Dissertation

submitted to the
Combined Faculties for the Natural Sciences
and for Mathematics
of the Ruperto-Carola University of Heidelberg, Germany
for the degree of
Doctor of Natural Sciences

Presented by
Dipl. Phys. Andreas Hahn
Born in: Zwickau, Germany
Oral examination: July 22, 2019

Moving Metal Artifact Reduction and Intrinsic Gating for Cone-Beam CT Scans of the Thorax Region

Referees: Prof. Dr. Peter Bachert

Prof. Dr. Marc Kachelrieß

Moving Metal Artifact Reduction and Intrinsic Gating for Cone-Beam CT Scans of the Thorax Region

In this work, novel algorithms in the field of retrospective intrinsic respiratory and cardiac gating and moving metal artifact reduction (MMAR) for cone-beam CT (CBCT) scans that are used in image-guided radiation therapy (IGRT) were developed. The added difficulty for CBCT scans is the relatively long acquisition time of up to 60 s compared to 0.25 s for clinical CT scans. The occuring respiratory and cardiac motion in combination with metal inserts cannot be handled with classical metal artifact reduction (MAR) methods. The proposed MMAR algorithms utilize an approach that combines the fields of motion compensation (MoCo) with classical MAR methods. In order for the MMAR methods to work, the motion state has to be known for every projection angle. A novel intrinsic gating approach, that automatically generates a list of potential motion surrogate candidates and identifies the best, was developed and used as a basis for the MMAR algorithms, so they can be applied for patients where no externally recorded motion signal is available. Whereas classical approaches for intrinsic gating are not designed for a laterally shifted detector, that is commonly used in IGRT with a CBCT, the novel algorithm works on scans with or without a shifted detector. It can also be used as a basis for 4D (3D + respiratory) or 5D (3D + respiratory + cardiac) MoCo algorithms.

Bewegte Metallartefaktreduktion und intrinsisches Gating Kegelstrahl-CT Scans der Thorax Region

Im Rahmen dieser Arbeit wurden Algorithmen im Bereich des retrospektiven intrinsischen Atem- und Herzgatings und im Bereich der bewegten Metallartefaktreduktion (MMAR) für Kegelstrahl-CT (CBCT) Scans, die in der bildgestützten Strahlentherapie (IGRT) verwendet werden, entwickelt. Die zusätzliche Erschwernis bei diesen CBCT Scans ist die vergleichsweise lange Scanzeit von bis zu 60 s im Vergleich zu 0.25 s bei einem klinischen CT. Die auftretende Atem- und Herzbewegung in Kombination mit Metallteilen kann durch klassische Metallartefaktkorrekturmethoden (MAR-Methoden) nicht behandelt werden. Die vorgeschlagenen MMAR Algorithmen verwenden einen Ansatz, der Methoden aus dem Bereich der Bewegungskompensation (MoCo) mit klassischen MAR Methoden verbindet. Damit diese MMAR Algorithmen funktionieren muss der Bewegungszustand für jeden Projektionswinkel bekannt sein. Ein neuer Ansatz für intrinsisches Gating, der automatisch eine Liste mit potentiellen Kandidaten für eine Bewegungssignal generiert und das beste auswählt, wurde entwickelt und als Basis für die MMAR Algorithmen verwendet, damit sie auch bei Patienten ohne extern aufgenommenes Atemsignal verwendet werden können. Während klassische Ansätze für intrinsisches Gating nicht für einen lateral verschobenen Detektor, der für gewöhnlich in der bildgestützten Strahlentherapie mit einem CBCT verwendet wird, ausgelegt sind, funktioniert der neue Algorithmus auf Scans mit und ohne lateral verschobenen Detektor. Er kann außerdem als Grundlage für 4D (3D + Atmung) oder 5D (3D + Atmung + Herz) MoCo Algorithmen verwendet werden.

Contents

List of Acronyms

acMoCo	artifact-specific cyclic motion compensation
AS	Amsterdam-Shroud method
bpm	beats per minute
CBCT	cone-beam computed tomography
CS	compressed sensing
CT	computed tomography
CTV	clinical target volume
ECG	electrocardiography
FBP	filtered backprojection
FDK	Feldkamp-Davis-Kress
FOV	field of view
GT	ground truth
GTV	gross tumor volume
IG	intrinsic gating
IGRT	image-guided radiation therapy
iTV	improved total variation
LINAC	linear accelerator
MAR	metal artifact reduction
MC	monte carlo
MMAR	moving metal artifact reduction
MoCo	motion compensation
MoCoMAR	moving metal artifact reduction using motion compensation
MVF	motion vector field
NMAR	normalized metal artifact reduction
PTV	planning target volume
rms	root-mean-squared
ROI	region of interest
RPM	Real-time Position Management system
rpm	respirations per minute

1. Introduction

Recent advances in the accuracy of treatment delivery in radiation therapy in combination with technological progress in medical imaging has lead to significant improvements in accuracy of dose distribution in radiation therapy (Gupta and Narayan 2012; Sterzing et al. 2011). A cone-beam CT (CBCT) is often used as an in-room imaging device for image-guided radiation therapy. Using volumetric or planar imaging, the patient position and the treatment plan can be registered to a planning CT scan acquired with a medical CT. It enables higher geometrical precision for the delivery of the MV treatment beam from a linear accelerator (LINAC). This way healthy tissue is spared and dose-escalation at the tumor made possible. It is most important when the tumor is close to organs-at-risk such as the esophagus or the spine, that should not be subjected to the radiation of the treatment beam. Variations of the tumor position or size between treatment sessions, e.g. caused by patient weight loss, changes of the tumor size or changes in the position of the tumor, or within a treatment session, e.g. caused by movement of the patient or respiratory or cardiac motion, can be detected and the treatment plan can be adjusted accordingly. It it also used to verify the treatment plan after treatment (Ahnesjö and Aspradakis 1999; Palta, Liu, and Li 2008).

Highly attenuating objects such as metal implants result in streaking artifacts in the reconstructed images and deteriorate the image quality. These artifacts can lead to potentially missed tumors if they are concealed by the metal artifacts. Due to the low rotation speed of the CBCT of usually 30-240 s, the patient cannot hold his breath during the scan time. Respiratory motion of the diaphragm and its surroundings leads to blurring in the reconstructed volume. Additionally, fiducial gold markers, that are implanted near tumors to enable tumor position tracking, can be subjected to motion and lead to streaking metal artifacts.

Algorithms that aim to correct artifacts caused by metal are called metal artifact reduction (MAR) algorithms and can be roughly divided into the following classes: iterative algorithms (Wang et al. 1996; De Man et al. 2001; Oehler and Buzug 2006; Lemmens, Faul, and Nuyts 2008), sinogram inpainting methods (Glover and Pelc 1981; Kalender, Hebel, and Ebersberger 1987; Mahnken et al. 2003; Wei et al. 2004; Jeong and Ra 2009; Bal and Spies 2006; Prell et al. 2009) and filtering methods (Bal et al. 2005). Iterative algorithms allow to include additional, physics-based information but are computationally expensive. While filtering methods use all available information, sinogram inpainting methods regard every ray that has passed metal as unreliable and replace the information using interpolation. They are computationally inexpensive but

can introduce new artifacts in the form of artificial blurring due to the interpolation. An approach that uses a sinogram normalization step has shown to greatly reduce or completely remove the newly introduced artifacts (Meyer et al. 2010). The use of a frequency split in the image domain can improve the result even further (Meyer et al. 2012).

Approaches that handle motion use some kind of motion surrogate, e.g. recorded using surface tracking techniques (Ford et al. 2002; Vedam et al. 2002; Pan et al. 2004), spirometry (Low et al. 2003; Zhang et al. 2003) or by measuring pressure changes with a respiratory belt (Dietrich et al. 2006; Kleshneva, Muzik, and Alber 2006). The first approach to account for motion that comes to mind is to only use projections that correspond to the same respiratory phase for reconstruction. This is called gating and leads to images that have a better temporal resolution but show artifacts due to the undersampling. Algorithms that use this phase-correlated reconstruction have to deal with the issue of reconstruction with undersampled data with irregular angular coverage (Leng et al. 2008a; Leng et al. 2008b; Bergner et al. 2009; Sawall et al. 2011; Ritschl et al. 2012; Jia et al. 2012). Another approach called motion compensation (Pengpan et al. 2012; Wang and Gu 2013; Brehm et al. 2012; Brehm et al. 2013; Yan et al. 2014; Dang et al. 2015; Biguri et al. 2017; Zhang et al. 2017; Sauppe et al. 2016b) uses information from all projections. Algorithms in this category use the phase-correlated udersampled reconstructed images to estimate motion vector fields (MVFs) that the phase-correlated volumes onto each other. This information can then be used to use all projections for the reconstruction of one motion phase resulting in a sharp volume without undersampling artifacts.

It is also possible to obtain a motion surrogate from the raw data. This is called intrinsic gating. It can be necessary if no external signal is available or if the external is corrupted. Besides that, an intrinsic signal is related more closely to true anatomic motion. Studies have found that the correlation between an external and an internal signal may not always be clear or change over time (Ahn et al. 2004; Hoisak et al. 2004; Tsunashima et al. 2004; Gierga et al. 2005; Yan et al. 2006). There are some methods for intrinsic respiratory gating that require user input (Dinkel et al. 2008; Farncombe 2008; Bartling et al. 2008; Hu et al. 2004), while others work fully automatically (Zijp, Sonke, and Herk 2004; Van Herk et al. 2007; Kavanagh et al. 2009; Vergalasova, Cai, and Yin 2012; Dhou, Motai, and Hugo 2013). A recent developement in motion compensation in CBCT scans by Sauppe et al. 2016b allows for 5D motion compensation, i.e. motion compensation that accounts for respiratory and cardiac motion. This has given rise to the need for intrinsic cardiac gating, since no ECG is normally used during these scans. The first method for cardiac gating is by Kachelrieß et al. 2002 and works for spiral scans. For CBCT scans, there is only a method for small animals that requires multiple rotations in order to work fully automatically (Kuntz et al. 2010).

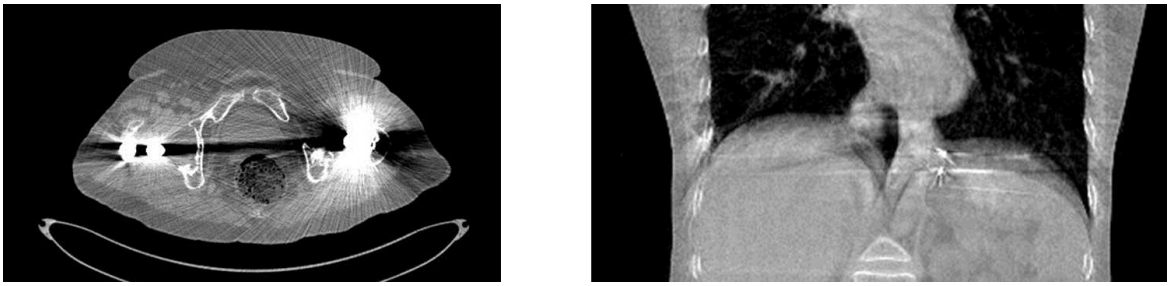

Figure 11.: Left: Axial slice of patient with a bilateral hip implant. The dark streaking artifacts are directed along the line of strongest attenuation, i.e. between the two implants. Right: Coronal view of patient with fiducial gold markers. Metal artifacts are caused by the markers. The diaphragm is blurred due to respiratory motion. C = 0 HU; W = 1500 HU.

Research in the field of the reduction of moving metal artifacts is scarce. All before mentioned MAR algorithms do not account for motion whereas all MoCo algorithms do not account for metal artifacts. There is an algorithm by Toftegaard et al. 2014 that uses a 3D marker model to remove artifacts caused by cylindrical gold markers. It does, however, require prior information in the form of the shape and size of the markers. An approach by Brehm et al. 2011, that uses a coarse segmentation step in the reconstructed volume in combination with a refined segmentation in the raw data, showed promising results.

The goal of this work is the development of novel algorithms, that can be used to remove artifacts caused by moving metal in CBCT scans. While classical methods focus either on the compensation of artifacts from static metal implants or motion compensation without any metal, the novel methods shall combine state-of-the-art algorithms of both fields to enable metal artifact reduction of moving metal inserts. The resulting algorithm shall be robust and independent of any prior knowledge. Since motion compensation requires information about the motion state for each projection angle, a novel algorithm to obtain a motion surrogate signal from the raw data was developed as well. This ensures that the MMAR algorithms can be used even if no external respiratory signal was recorded or if it is damaged.

In the first part of the thesis, the new algorithm for intrinsic respiratory gating is developed. Since classical approaches are not designed for scans with a laterally shifted detector, that is commonly used in IGRT with a CBCT, the development of a new method was necessary. Using a novel raw data based approach, that automatically determines the best respiratory signal from a large group of possible candidates, a respiratory motion surrogate can be obtained for scans with or without a laterally shifted detector. This signal can then be used for the motion compensation algorithms that are a part of the MMAR algorithms. It was found that said algorithm can be used to obtain a cardiac signal as well with only small modifications. This signal can be used

for novel approaches in the field of 5D motion compensation (Sauppe et al. 2016b).

In the second part of the thesis, two novel algorithms that combine metal artifact reduction and motion compensation were developed and an approach by Brehm et al. 2011 was refined. The first new MMAR algorithm (MoCoMAR1) uses the acMoCo algorithm by Brehm et al. 2013 to segment the moving metal in the original raw data. The mask is then used for inpainting-based metal artifact reduction by Meyer et al. 2010. The result is an metal artifact free 3D volume. Like the algorithm by Brehm et al. 2011 it is suitable for metal objects of all shapes and reduces to a classical inpainting MAR algorithm for static metal objects. The second new MMAR algorithm (MoCoMAR2) uses the acMoCo algorithm and a conventional inpainting MAR method by Meyer et al. 2010 as well, but returns a 4D volume without motion or metal artifacts.

2. Fundamentals

In this chapter, the fundamentals for the algorithms that were developed within this thesis are explained. First, the context of the imaging device that is the subject of this thesis, i.e. a cone-beam CT that is used in image-guided radiation therapy, is depicted in Sec. 2.1. After that, the physical background of X-ray–matter interaction is explained in Sec. 2.2. Next, the basic principles for the reconstruction of CBCT images are illustrated (Sec. 2.3). Finally, artifacts that can typically occur in the reconstructed images due to metal or respiratory motion and state-of-the-art methods to reduce or remove them are explained in Sec. 2.4.

2.1 IMAGE-GUIDED RADIATION THERAPY

Image-guided radiation therapy (IGRT) describes the use of an imaging device in the treatment room immediately before or during a treatment session (Verellen, De Ridder, and Storme 2008; Dawson and Jaffray 2007), called fraction. The goal is to improve tumor localizations and therefore the targeting of the MV treatment beam. This is especially important in regions in the proximity of organs-at-risk, e.g. the heart or the spine, to spare healthy tissue and allow high-precision dose escalation. A treatment scheme using IGRT is shown in Fig 21. First, a clinical CT scan is made to delineate the tumor. This is called the gross tumor volume (GTV). To include proliferating tumor cells in the proximity of the GTV, it is extended by a safety margin and called clinical target volume (CTV). Finally, another safety margin has to be included that accounts for geometric uncertainties, e.g. caused by respiratory motion or uncertainties in the patient position. This so called planned target volume (PTV) can be decreased by the use of image guidance during radiation therapy.

There are various reasons why the planning CT scans may be an inaccurate representation of the patient during the different fractions. They can be grouped into interfractional variations, i.e. variations between fractions, and intrafractional variations, i.e. variations during the course of one fraction.

Interfractional Variations

Before the treatment starts, the position of the patient has to be verified. To aid in this task, immobilization techniques using shoulder fixators or arm positioning devices are

used. They can fix the patient position with an accuracy of up to 10 mm (Sterzing et al. 2009; Zeidan et al. 2007). Even if the surface of the patient is aligned perfectly, internal organ position may change between treatment sessions. In the thorax region, there can be strong variations in the position of the esophagus. Another source of error are changes in the anatomy of the patient. The size of the tumor can change between fractions, as well as the size of surrounding tissue or the weight of the patient. This needs to be accounted for in an updated treatment plan.

Intrafractional Variations

Besides variations between fractions, there are also variations within a single fraction caused by two factors. First, it is possible that the patient moves. This factor can be reduced by using fixations and by making the patient aware of the importance of being still. The second factor is respiratory and cardiac motion. To minimize this error, irradiation can be restricted to one respiratory phase. This is called gating. The work in this thesis is about the reduction of the effects caused by respiratory and cardiac motion during a treatment session when a cone beam CT is used as an imaging device. The first part focuses on obtaining a respiratory and cardiac motion surrogate signal from the raw data. The second part deals with metal artifacts mainly caused by fiducial gold markers, that are placed near organs of interest to allow for better organ localization.

For both reasons, intra- and interfractional changes, image-guidance can improve the geometrical localization of the tumor. The workflow is as follows (Fig. 21): In the planning phase, a clinical CT scan is used to delineate the PTV and to create a treatment plan. In the treatment phase, an in-room imaging device is used for registration with the planning CT scan. Corrections to the treatment plan can than be done either online or offline. For offline corrections, the patient is scanned directly before the treatment session. After a 3-5 fractions, errors to the treatment plan are calculated after a fraction and corrected for the next fraction. For online treatment plan adaption, the patient is scanned using the in-room imaging device and the plan is adapted right before the treatment. Finally, the in-room imaging device can be used for treatment plan verification.

While ultrasound was the first in-room imaging device for IGRT, a CBCT is widely used today. It can be used either for volumetric or planar imaging. While the MV treatment beam of the linear accelerator (LINAC) can be used for imaging as well, it has a poor soft tissue resolution due to beam energies between 6-18 MV. It is, however, less prone to metal artifacts for the same reason. There are modern systems, that have an integrated kV cone-beam CT unit mounted perpendicular to the LINAC. With energies between 40-140 kV, it has a better soft tissue resolution than the MV beam (Ding and Munro 2013). Volumetric images acquired with such a CBCT unit are the subject of this thesis. The advantage of volumetric imaging is better organ delineation. Due

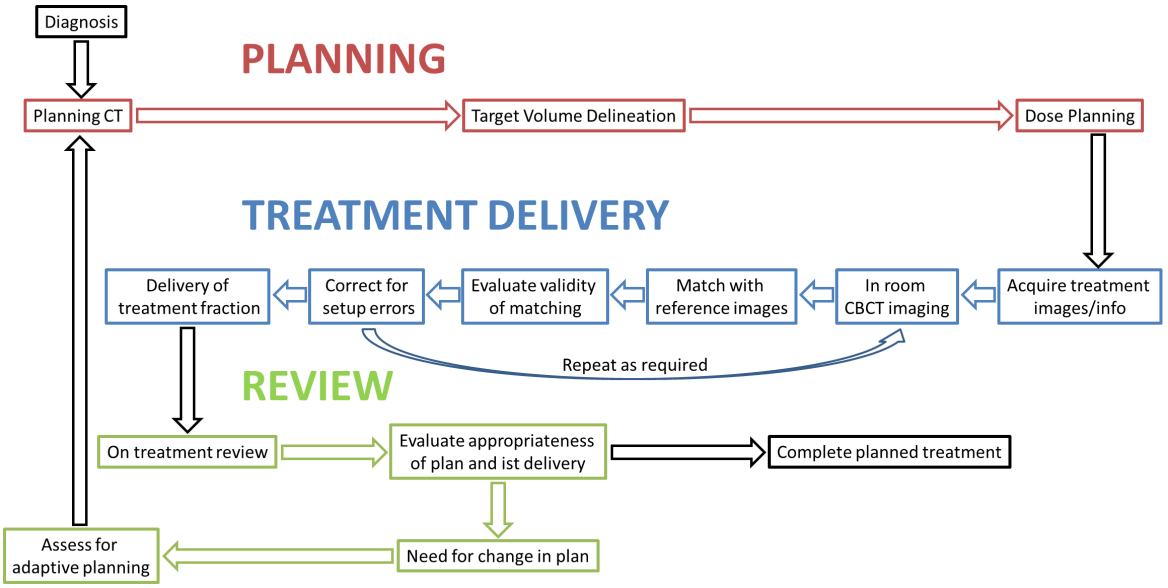

Figure 21.: Clinical workflow for image-guided radiation therapy using a CBCT. After an initial scan with a clinical CT, a treatment plan is created. Before each treatment session, the planning CT scan is registered to a in-room CBCT scan. It enables offline or online treatment plan adaptation and is also used for treatment plan verification. Adopted from Gupta and Narayan 2012

to the slow rotation times of the CBCT between 15-120 s, patient respiration leads to blurring in the reconstructed volumes. Another source of artifacts, are fiducial gold markers that lead to streaking metal artifacts. They can also be subjected to respiratory motion, which is not covered by conventional algorithms for metal artifacts reduction. All patients in this thesis have been scanned using integrated kV unit of a Varian TrueBeam® (Varian Medical Systems, Palo Alto, Calif.). It is shown in Fig 22.

2.2 X-RAY–MATTER INTERACTION

In this section, the physical basics for the interaction of X-ray radiation with matter in the context of medical imaging are briefly explained. Electromagnetic radiation with an energy over 100 eV is called X-ray radiation. Typical photon energies from the X-ray sources in CT range from 100 keV to 140 keV. In this energy range, the main mechanisms for energy loss of photons are the photoelectric effect and Compton scattering. Pair production (Bethe and Heitler 1934), in which an electron and a positron are created, requires energies above 2×511keV, i.e. double the rest mass of an electron, and does not occur in X-ray imaging. First, the general absorption of non charged particles in matter, which is described by the Lambert-Beer-law, is described followed by the photo-electric effect and scattering.

Figure 22.: A kV CBCT imaging unit is mounted perpendicular to the treatment beam (Varian TrueBeam®).

Lambert-Beer-law

The absorption of light in matter is described using the Lambert-Beer-law (Bouguer 1729; Lambert 1760). For a beam of light with an initial intensity I_0, the intensity I after traversing a length l in a homogenous material with an attenuation coefficient μ is given by

$$I = I_0 e^{-\mu l}. \tag{21}$$

The exponent $p = \mu l$ is called projection value. In CT, one usually looks at projection values and not at intensities. From a scan without an object, I_0 can be obtained and p is given by

$$p = -\ln(I/I_0). \tag{22}$$

The goal of a CT reconstruction is to obtain a 3D map of attenuation values μ from a series of projection values p. Since the human body consists mostly of material with a similar attenuation than water, the CT values are defined relative to the attenuation value of water μ_{water} in Hounsfield units (HU) (Brooks 1977):

$$\text{CT} = \frac{\mu - \mu_{\text{water}}}{\mu_{\text{water}}} 1000\text{HU} \tag{23}$$

This way, water or water equivalent objects have a CT value of 0 HU, air of -1000 HU. A CT value of 1000 HU means that the objects attenuation is twice as big as the

attenuation of water. μ depends on the material and the photon energy. It is related to the physical cross-section σ in the following way:

$$\mu(E) = \frac{\rho N_A}{A}\sigma(E) \tag{24}$$

ρ denotes the density of the material, N_A is the Avogadro number and A is the atomic mass. Due to the energy dependence of σ, μ_{water} depends on the spectrum of the X-ray source of the used CT system. The cross-section σ is dominated by the cross-section of the photoelectric effect σ_{PE} and the Compton effect σ_{C}, which are described next.

Photoeletric Effect

There are three related physical effects that are summarized under the photoelectric effect:

1. External photoelectric effect: An electron at the surface of a semi-conductor or metal is emitted after completely absorbing a photon. The kinetic energy of the electron is the difference of the work function (electron binding energy) and the photon energy. This implies that the photon energy has to be larger than the work function. After being discovered by Becquerel and documented by Hertz (Hertz 1887), Einstein delivered the theoretical explanation for this effect (Einstein 1905), which was rewarded with the nobel prize in physics.
2. Internal photoelectric effect: This effect occurs mainly in semi-conductors, where the photon lifts an electron into the conduction band.
3. Photo-ionization, also called atomic photoeffect: Here, a tightly bound electron from an inner shell of an atom or molecule is emitted by absorbing a photon. This is the relevant effect for CT imaging.

The probability of the photoelectric effect is given by its cross-section σ_{PE}, which can be approximated as

$$\sigma_{\text{PE}} \propto \frac{Z^4}{E^3} \tag{25}$$

for photon energies around 100 keV, that are typical for CT imaging. It has a strong dependence on the atomic number Z, i.e. the probability for photoelectric photon absorption strongly increases with larger atomic numbers.

Compton Scattering

The Compton effect is the inelastic scattering of a photon by a charged particle, e.g. an electron in the outer shell of an atom, and was first described by A. H. Compton (Compton 1923). The charged particle is regarded as static. In contrast to the

photoelectric effect, there is still a photon after the interaction. The energy transfer from the photon to charged particle depends on the direction, i.e. the angle, in which the charged particle is scattered. The cross-section σ_{CS} is given by

$$\sigma_{\mathrm{CS}} \propto \frac{Z}{E^m}, \tag{26}$$

with $0 \leq m \leq 1$. Since the attenuation coefficient is proportional to σ/A, σ_{CS} is proportional to Z/A, which is approximately constant for stable atoms. Compton scattering is therefore nearly independent of the material.

Rayleigh Scattering

Elastic scattering of a photon with a charged particle is called Rayleigh scattering. In contrast to Compton scattering, where the photon is scattered at an electron in an outer shell, the photon is scattered at the whole atom. Hence, the photon keeps its energy and only slightly changes its direction. Its cross-section is given by

$$\sigma_{\mathrm{RS}} \propto \frac{Z^2}{E^2}. \tag{27}$$

It has a low dependence on the atom number and on the energy. Due to the elastic nature of the scattering, no energy is deposited in the patient by Rayleigh scattering. It only causes X-ray photons to be detected in a different detector pixel than expected.

The energy dependence of the photoelectric effect, Compton scattering and Rayleigh scattering are shown in Fig. 23 for water. For low energies, the photoelectric effect and Rayleigh scattering are dominating the attenuation. For higher energies, Compton scattering is the dominant effect.

2.3 RECONSTRUCTION

In a medical CT scan, the X-ray source and the detector rotate around the patient. The X-rays are attenuated by the patient and all remaining photons are measured at the detector. In general, there are two domains in which all CT algorithms operate: The image domain, i.e. the reconstructed volume f, and the raw data domain, i.e. the projection values p measured at the detector. For a monochromatic X-ray source, f is a 3D map of the attenuation values $\mu(\vec{r})$. The projection value of a ray traversing the path γ that is measured at a detector pixel is given by the X-ray transform X of the attenuation map $\mu(\vec{r})$:

$$p = \int_\gamma \mu(\vec{r})\,\mathrm{d}s = \mathrm{X}f \tag{28}$$

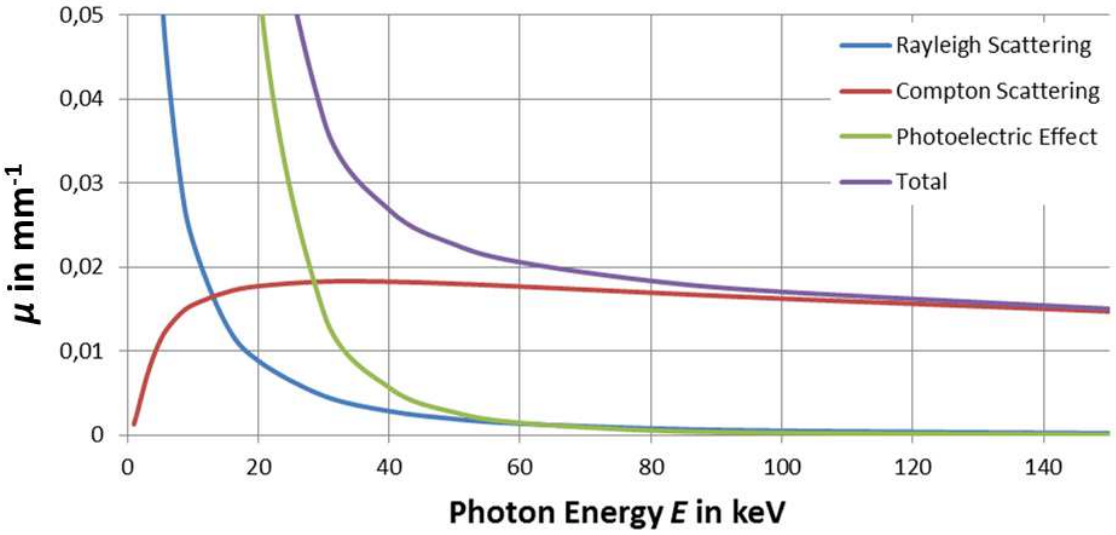

Figure 23.: Contributions of Compton scattering, Rayleigh scattering and the photoelectric effect to the total attenuation coefficient μ_{water} of water with a density $\rho = 1\frac{g}{cm^3}$.

The simple case of a 2D parallel beam geometry is illustrated in Fig. 24. In this case, the X-ray transform is identical to the Radon transform. Each ray can be parametrized by its distance to the isocenter ξ and its projection angle ν with

$$\xi = \xi(x, y, \nu) = x \cos \nu + y \sin \nu. \tag{29}$$

The projection value p is then given by

$$p(\xi, \nu) = \mathrm{X}f(\xi, \nu) = \iint \mu(x, y)\, \delta(\xi - x \cos \nu - y \sin \nu)\, \mathrm{d}x\, \mathrm{d}y. \tag{210}$$

The goal of the reconstruction is to find the inverse X-ray transform $\mathrm{X}^{-1}$of p, which is called filtered backprojection, whereas the X-ray transform X is called forward projection. Accordingly, the image on the detector for one projection angle is called projection. When one detector row is depicted over all projection angles, one speaks about a sinogram. The name comes from the fact, that a fixed point in the volume describes a sinusoidal curve in the sinogram.
In order to calculate the filtered backprojection, the one dimensional Fourier transform P of p with respect to ξ has to be calculated:

$$\begin{aligned} \mathfrak{F}p(u, \nu) = P(u, \nu) &= \int p(\xi, \nu) e^{-2\pi i u \xi}\, \mathrm{d}\xi \\ &\overset{(29)}{=} \iint \mu(x, y)\, e^{-2\pi i u (x \cos \nu + y \sin \nu)}\, \mathrm{d}x\, \mathrm{d}y \end{aligned} \tag{211}$$

Next, the two dimensional Fourier transform M of μ is calculated:

$$\mathfrak{F}\mu(u_x, u_y) = M(u_x, u_y) = \iint \mu(x, y) e^{-2\pi i(u_x + u_y)} \, \mathrm{d}x \, \mathrm{d}y \tag{212}$$

By comparing Eq. (211) and Eq. (212) one finds

$$P(u, \nu) = M(u \cos \nu, u \sin \nu). \tag{213}$$

This is also known as Fourier slice theorem. It can be used to calculate μ:

$$\begin{aligned}
\mu(x, y) = \mathfrak{F}^{-1} M(x, y) &= \iint M(u_x, u_y) \, e^{2\pi i(u_x + u_y)} \, \mathrm{d}u_x \, \mathrm{d}u_y \\
&= \iint M(u \cos \nu, u \sin \nu) \, e^{2\pi i(u \sin \nu + u \cos \nu)} \, |u| \, \mathrm{d}u \, \mathrm{d}\nu \\
&\overset{(213)}{=} \iint P(u, \nu) \, e^{2\pi i(u \sin \nu + u \cos \nu)} \, |u| \, \mathrm{d}u \, \mathrm{d}\nu \\
&\overset{(29)}{=} \iint P(u, \nu) \, e^{2\pi i u \xi} \, |u| \, \mathrm{d}u \, \mathrm{d}\nu \\
&= \int \mathfrak{F}^{-1} \left(P(u, \nu) \, K(u) \right) \, \mathrm{d}\nu, \text{ with } K(u) = |u|.
\end{aligned} \tag{214}$$

In the first step of Eq. (214) $u_x = u \cos \nu$ and $u_y = u \sin \nu$ were substituted with the Jacobian being $|u|$. In the last step, the integral over u was interpreted as the inverse Fourier transform of the $P \cdot K$. Using the convolution theorem, this can be rewritten in the following way:

$$\begin{aligned}
\mathfrak{F}(p * k) &= \mathfrak{F}(p) \cdot \mathfrak{F}(k) \\
\mathfrak{F}^{-1}\mathfrak{F}(p * k) &= \mathfrak{F}^{-1} \left(\mathfrak{F}(p) \cdot \mathfrak{F}(k) \right) = \mathfrak{F}^{-1}(P \cdot K) \\
\Leftrightarrow p * k &= \mathfrak{F}^{-1}(P \cdot K)
\end{aligned} \tag{215}$$

Here, k is the inverse Fourier transform of K. Inserting this result in Eq. (214) gives the formula for the filtered backprojection.

$$\mu(x, y) = \int p(\xi(x, y, \nu), \nu) * k(\xi(x, y, \nu)) \, \mathrm{d}\nu \tag{216}$$

k is called filter kernel and can easily be calculated:

$$k(\xi) = \int K(u) \, e^{2\pi i u \xi} \, \mathrm{d}u = \int |u| \, e^{2\pi i u \xi} \, \mathrm{d}u = \frac{-1}{2\pi^2 \xi^2} \tag{217}$$

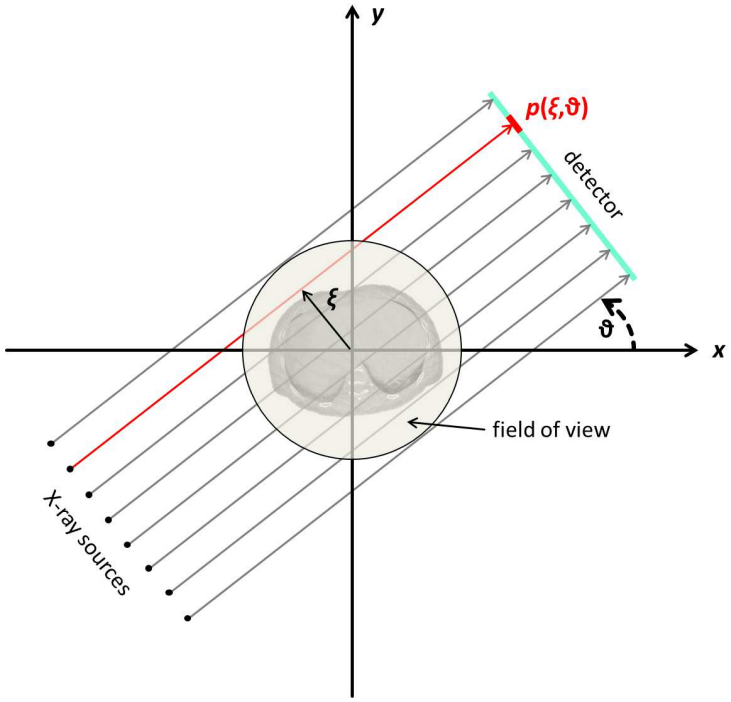

Figure 24.: Parallel beam geometry. For each detector pixel p there is one source that only sends photons to said pixel. The sources are arranged so that all X-rays are parallel. Each ray can be parametrized by the distance to the isocenter ξ and the rotation angle ν. All points that can be covered from 180° are called the field of view.

In the context of this thesis, all patients were scanned in a cone-beam geometry. An algorithm for the reconstruction in this geometry that is based on the filtered back-projection was introduced by Feldkamp, Davis, and Kress 1984 and is widely used. A prerequisite for the reconstruction is that all points in the volume that are to reconstructed have to be seen from 180°. Otherwise, limited angle artifacts occur. More than 180° provide no new information, since the opposite direction of the ray provides the same attenuation information. The area of all points that are covered from 180° is called the field of view (FOV). In order to increase the FOV, the detector was shifted laterally for all scans that are presented in this thesis. In order to maintain the 180° coverage for all points, a full rotation is needed with a shifted detector since not all points of the FOV are seen by the detector for all source angles.

2.4 ARTIFACTS

In the previous section reconstruction under ideal circumstances was described. These ideal circumstances are not met in real scans for various reasons and any deviation leads to errors in the reconstructed volume which are called artifacts. For the scope of

this thesis, metal artifacts, which are described in section 2.4.1, and motion artifacts, which are described in section 2.4.3, are most important and described in detail.

2.4.1 Metal Artifacts

Metal artifacts is a generic term that sums up artifacts that are mostly caused by objects with high densities and high atomic numbers, such as metal. The main causes, i.e. beam hardening, scatter and nonlinear partial volume artifacts, are explained here.

Beam Hardening

In section 2.3, the monochromatic projection value p was introduced:

$$p_\gamma = \int_\gamma \mathrm{d}s\, \mu(\mathbf{r}). \tag{218}$$

In reality, the X-ray tube produces a polychromatic X-ray spectrum $w(E)$, that depends on the anode material and the tube voltage. For diagnostic CT imaging, photon energy can range between 20 keV and 200 keV. In this energy range, photon absorption is dominated by the photo-effect and Compton scattering. Since the photoelectric effect is proportional to Z^3/E^3 and the Compton scattering to $1/E$, lower energy photons are absorbed more easily. The spectrum is therefore shifted to higher energies, i.e. the beam becomes harder. This effect is called beam hardening. The magnitude of this effect is related to the length the beam traverses through the dense material. The longer the way, the harder the beam becomes. Since photons with higher energy are attenuated less than photons with smaller energy, more photons reach the detector than anticipated. This leads to an underestimation of the attenuation value of the material and as a consequence to smaller CT values in the center of an object. This is called a cupping artifact.

To account for the energy dependency of the attenuation value μ, the polychromatic, measured projection value q is given by

$$q_\gamma = \int \mathrm{d}E\, w(E) e^{-\int_\gamma \mathrm{d}s\, \mu(\mathbf{r},E)}, \tag{219}$$

with

$$\int \mathrm{d}E\, w(E) = 1. \tag{220}$$

As a first order approximation, let us assume that the scanned object consists of only one material. μ can then be written as a product of a space dependent part $\mu(\mathbf{r})$ and an energy dependent part $\psi(E)$. Since the human body mostly consist of water equivalent materials, i.e. soft tissue, this is a good approximation for diagnostic CT. q is then given by

$$q_\gamma = \int \mathrm{d}E\, w(E) e^{-\int_\gamma \mathrm{d}s\, \mu(\mathbf{r})\psi(E)} = \int \mathrm{d}E\, w(E) e^{-p_\gamma \psi(E)} \tag{221}$$

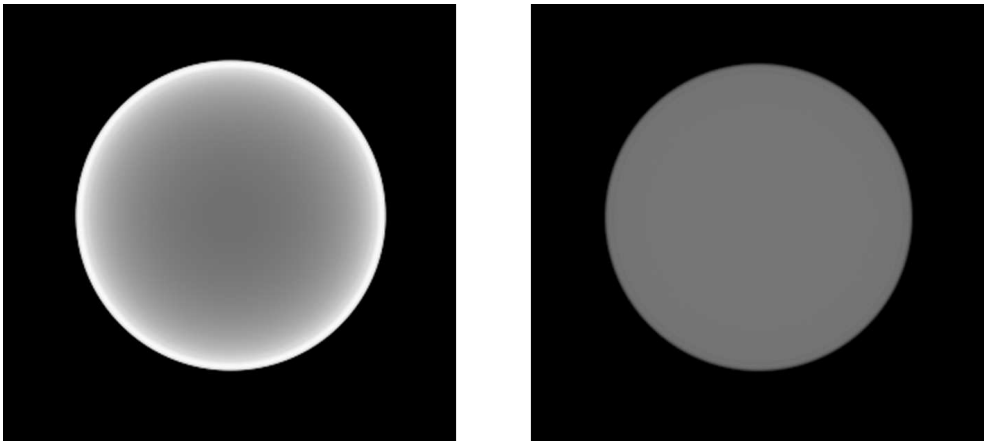

Figure 25.: Left: Water phantom simulated using the Tucker spectrum from Fig. 26. The attenuation values in the center are underestimated due to beam hardening. Right: Same water phantom after a water precorrection using a look-up table and the knowledge of the Tucker spectrum. (C=0 HU, W=1000 HU).

This non-linear relation between p and q can be inverted numerically. For clinical CT scans this is called water precorrection and done using calibration schemes (Grimmer et al. 2012; Kijewski and .Bjarngard 1978; McDavid et al. 1977; Ruth and Joseph 1995; Stonestrom, Alvarez, and Macovski 1981). If no calibration was done, the empirical cupping correction algorithm (Kachelrieß, Sourbelle, and Kalender 2006; Ritschl et al. 2010) offers a simple image-based method to remove cupping.

To illustrate the beam hardening effect, a simulated water cylinder with a diameter of 10 cm is shown in Fig. 25 before (left) and after water precorrection (right). The simulation was conducted using Eq. 219 and a polychromatic spectrum according to Tucker, Barnes, and Chakraborty 1991. A 1.0 mm aluminum and 0.9 mm titanium prefilter as well as a 2 mm gadolinium oxysulfide energy integrating detector were used for the creation of the spectrum (Fig. 26). As water precorrection, the beam hardening was removed numerically using the known Tucker spectrum and a look-up table. The uncorrected volume shows the typical cupping artifact with underestimated attenuation values in the middle and overestimated values at the border. If the spectrum was known, it can be removed perfectly.

Note that it is only possible to correct beam hardening for one material at a time. Due to the much higher atomic number of metal, beam hardening still remains an issue and leads to dark and bright streaking artifacts (Fig. 11). There are several methods dedicated to metal artifact correction, nearly all of which only account for metal that is not subjected to motion. An overview over the different approaches is given in section 2.4.2 as a preparation for the new methods that are presented in this thesis.

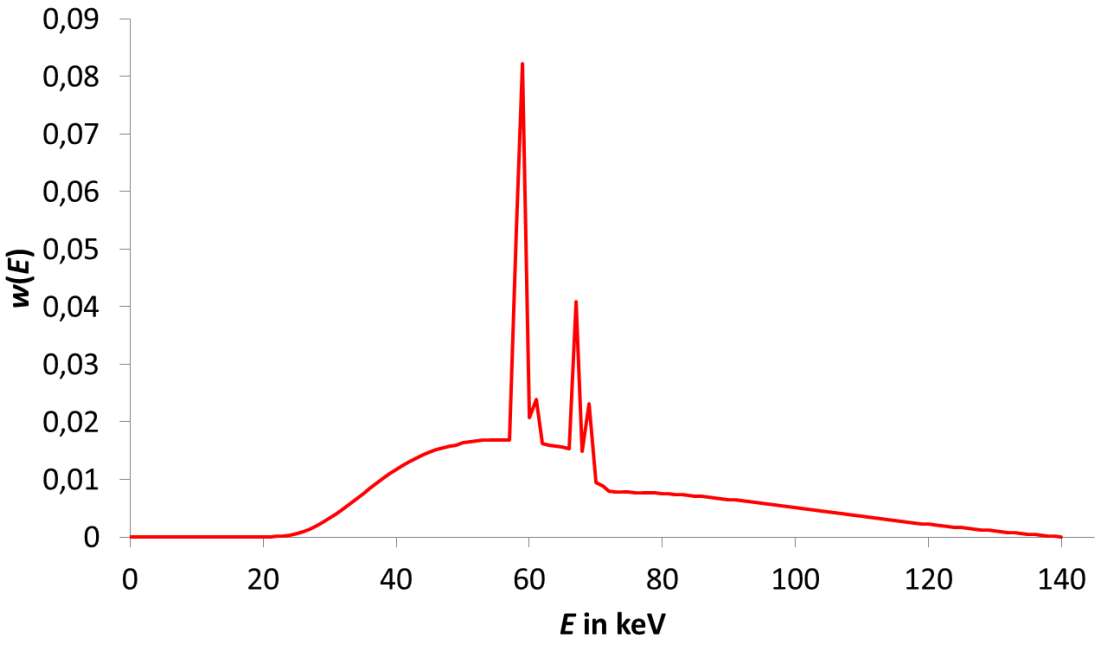

Figure 26.: 140 kV X-ray spectrum created according to Tucker, Barnes, and Chakraborty 1991. A 0.9 mm titanium and 1.0 mm aluminum pre-filter and a 2 mm gadolinium oxysulfide energy integrating detector were simulated. The spectrum is normalized to 1.

Scattering

For diagnostic imaging, Rayleigh scattering has only a small contribution to the cross-section. At a typical average energy of 70 kev, the cross-section of Rayleight scattering and the photoelectric-effect contribute only around 10%, whereas the cross-section for Compton scattering contributes around 90%. It has the strongest impact where little or no photons are registered. For strongly attenuating metal inserts, scattered photons in areas where very few photons are detected lead to an underestimation of the attenuation. This leads to cupping artifacts, that are similar to beam hardening, as well as noise.
When it comes to the reduction of artifacts caused by scattering, one can either try to reduce the amount of scattered photons at the detector using anti-scatter grids or collimators (Rührnschopf and Klingenbeck 2011) or use algorithms to estimate the scatter distribution in order to correct for it. The gold standard, that includes all physical effects in its calculations, is a Monte Carlo (MC) transport code (Rührnschopf and Klingenbeck 2011). It is, however, computationally very complex and time consuming and cannot be done in real-time. A less time demanding approach are kernel-based approaches. Here, a kernel describes the probability of each ray between the source and a detector pixel to be scattered. The parameters needed for the kernel can either be deduced from theoretical models or can be fit using MC simulations (Bhatia et al. 2016; Li, Mohan, and Zhu 2008; Lo et al. 1993; Love and Kruger 1987; Meyer, Kalender, and Kyriakou 2009; Rinkel et al. 2007; Spies et al. 2001; Star-Lack et al. 2009; Sun and

Star-Lack 2010; Swindell and Evans 1996). While kernel methods are much faster, they are less accurate and depend on good parameter selection. Recently, a deep scatter approach by Maier et al. 2018 was able to produce results that are comparable to the MC approach with the speed that is comparable to kernel-based approaches by using a deep neural network.

Nonlinear Partial Volume Effects

Partial volume effects occur when there are local variations in the attenuation that are smaller than the resolution of the reconstructed volume. This effect is especially strong when there is metal inserts, due to the sharp edges and high attenuation. As a consequence, the relation between the projection value p and the attenuation value μ is no longer linear, even if the X-ray source was monochromatic (Glover and Pelc 1980).

2.4.2 Metal Artifact Reduction

An intuitive approach to remove metal artifacts is to combine the artifact reduction strategies for each artifact source, e.g. scattering and beam hardening, to remove all artifacts. However, for stronger metal artifacts, e.g. caused by a bilateral hip implant or dental fillings, the X-rays traversing the metal are attenuated so much that they cannot be used any more. Algorithms that replace all projection values that are corrupted by metal are called metal artifact reduction (MAR) methods. In the most basic approach by Kalender, Hebel, and Ebersberger 1987, metal is segmented in an initially reconstructed volume using a threshold. While it would be difficult to locate the metal in the raw data since it is superimposed with the patient anatomy, e.g. soft tissue and bones, it can easily be segmented in the volume due to its higher attenuation values. Since the position of the metal is known in the volume, it can be tracked in the projections using forward projection. All pixels in the metal mask in the raw data are replaced using interpolation. The interpolation is not done on the projections but on sinograms. A sinogram shows one detector row over all projection angles, whereas a projection shows the whole detector for one projection angle. While this makes no difference for row-wise linear interpolation, it can make a difference for similar algorithms that use more advanced interpolation schemes, e.g. bilinear interpolation. After the interpolation, a metal free and artifact free volume is reconstructed and the initially segmented metal reinserted in a final step. This method is called MAR1 in this thesis and its scheme is shown in Fig. 27. Methods that replace projection values p that are effected by metal with artificial data are called inpainting methods.

A drawback of this approach is the loss of information due to the inpainting. Regions in the proximity of the metal and between metal inserts are especially prone to this error. There are various approaches that apply the same principle with more advanced inpainting methods (Mahnken et al. 2003; Yu et al. 2009; Veldkamp et al. 2010; Kratz et al. 2011) which have lead to limited improvement. A recent approach

by Meyer et al. 2010 called NMAR utilizes a normalization step and is able to remove metal artifacts without the introduction of new ones. It is an extension of the MAR1 algorithm. From the originally reconstructed volume, a prior ternary artifact free image is created that divides the volume into three classes using thresholds: air, soft tissue, and bones + metal. Air is set to -1000 HU, soft tissue to 0 HU and bone keeps its value, since it its attenuation value can vary strongly. It does not matter what metal is replaced with in the volume, since it will be interpolated in the raw data. The original sinogram is then divided pixelwise by the forward projected prior sinogram. This is called normalization step, since it leads to a more or less flat sinogram. Linear interpolation is done on the normalized sinogram and the result is denormalized by multiplicating it with the prior sinogram (Fig. 27). This way, the structural information in the proximity of the metal implant is preserved and no new artifacts are introduced. In cases with vary strong attenuation, e.g. the space between a bilateral hip implant, this normalization may not be enough. In this case, a frequency split approach can be utilized (Meyer et al. 2012). It is an image-based approach that conserves the high frequencies of the originally reconstructed volume in the proximity of the metal. This way even fine structures can be preserved that would otherwise be damaged by the interpolation.

Besides the before mentioned approaches, there are iterative algorithms, that use additional knowledge like photon statistics or the physics of the data acquisition process (Wang et al. 1996; De Man et al. 2001; Lemmens, Faul, and Nuyts 2008). In most cases they also regard the metal data is unreliable and aim to replace it, which is why they can also be classified as inpainting algorithms. A popular iterative algorithm that uses compressed sensing (CS) is called improved total variation (iTV) and aims to minimize the total variation of the reconstructed image (Sidky and Pan 2008; Ritschl et al. 2011). A drawback of all iterative algorithms is that it is very time consuming, which makes it hard to incorporate them into a clinical setup. Often, a classical inpainting approach can be used that performs equally well.

All of the previously mentioned algorithms are designed for metal inserts that are not subjected to motion. They mostly rely on metal segmentation in the volume to find the metal in the raw data. However, if the metal is moving due to the patients respiration during the relatively long acquisition times of a CBCT, two problems occur:

- The reconstructed metal is blurred. Therefore, it may have attenuation values below the values one would expect for metal or even in the range of bones. Threshold-based segmentation is no longer feasible in this case.

- Even if it is segmented properly, its forward projection does not cover the full motion range of the metal in the raw data. This leaves the user of classical MAR algorithms like MAR1 or NMAR with two options: Either the metal mask in the raw data has to be largely extended or not the whole range of motion is covered. While the first possibility leads to a large artificially smooth area in the

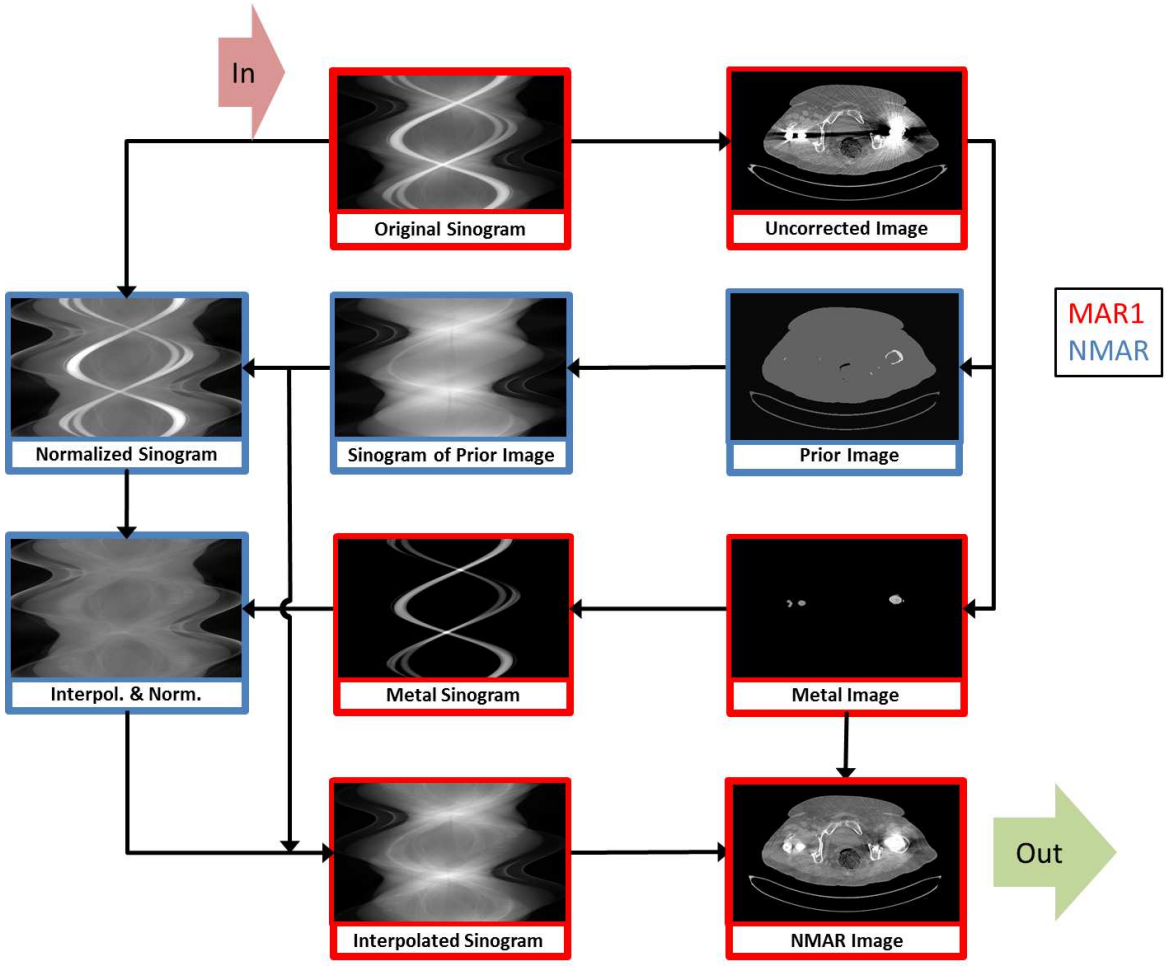

Figure 27.: Schemes of MAR1 (Kalender, Hebel, and Ebersberger 1987) (red border) and NMAR (Meyer et al. 2010) (red + blue border). For MAR1, metal is segmented in an initially reconstructed volume. This maske is used to identify all pixels in the original sinogram that are corrupted by metal and replace them using linear interpolation. Reconstruction of the metal free gives an metal and artifact free volume in which the originally segmented metal is reinserted. For NMAR, a normalization step using a ternary prior image, is applied before interpolation.

reconstructed volume that may obscur a tumor in the proximity of the metal, the second possibility results in a volume where not all metal artifacts are removed.

A recent approach by Toftegaard et al. 2014 uses a 3D marker model to deal with both issues. It is designed for small cylindrical gold fiducial markers and uses the information about the size and shape of the markers to segment them in the projections. From this, a 3D marker model is created. The markers are removed from the raw data using linear interpolation. From the 3D marker model the position of markers is known for all times. It is used to estimate an ellipsoid that contains 95 % of the 3D positions of the marker, which is in turn used to reinsert the markers. While this method showed promising results, it requires prior knowledge in the form of the shape and size of the markers. A more general approach by Brehm et al. 2011 does not require any prior information. It uses an initial metal segmentation in the volume to obtain a coarse metal mask in the raw data. This mask is dilated to include the whole range of motion of the metal. In a second step, the metal is segmented within the coarse mask in the raw data. While it is not feasible to segment the metal in a complete projection, it can be done within a small area, i.e. the coarse mask, by using edge detection methods. This gives a refined mask that is used for linear interpolation. The initially segmented metal is reinserted into the metal- and artifact free volume. The drawback of this approach is that the initial metal segmentation in the volume might fail if it is blurred too much. This algorithm is called MMAR in the following. Besides the new methods proposed in this thesis, these are the only methods dedicated to moving metal.

The algorithms proposed in this thesis aim to correct for moving metal inserts. Two new methods are developed that utilize motion compensation to segment the metal (MoCoMAR1 and MoCoMAR2). Additionally, MMAR is extended by an improved segmentation in the volume to overcome its drawback.

2.4.3 Motion Artifacts and Motion Management

Motion caused by motion of the patient can lead to misalignment artifacts but is not the subject of this thesis. Here, respiratory and cardiac motion that occur in CBCT scans of the thorax region are discussed. A typical patient shows average respiratory motion of 1-11 mm in anterior-posterior-direction and 6-20 mm in superior-inferior-direction (Ionascu et al. 2007) and between 13 and 23 respirations per minute (rpm) (Kory 1957; Quirk, Becker, and Smith 2013; Bianchi et al. 2013). Cardiac motion ranges between 3-8 mm between end-diastole and end-systole with a frequency between 50 and 100 beats per minute (bpm) (Lentner 1990; Tan et al. 2013). Due to the poor time resolution of a typical CBCT scan that takes about 60 s, respiratory and cardiac motion leads to blurring around the diaphragm and the ventricular wall (Fig. 28, left). If metal is present and subjected to motion as well, the metal artifacts cover a larger area depending on the range of motion.

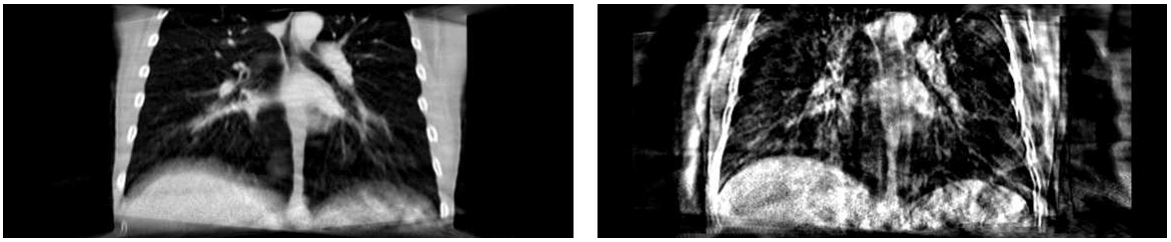

Figure 28.: Coronal slice of reconstructed CT volume. Left: Standard 3D reconstruction. The diaphragm is blurred due to respiratory motion. Right: Respiratory gated reconstruction. The diaphragm is sharp but strong artifacts appear due to undersampling.

In medical imaging there are several strategies to deal with these issues. The first approaches focus on physically reducing the respiratory motion by using breath-hold techniques or audiovisual coaching of the patient (Kini et al. 2003; George et al. 2006). While breath-holding is easily done for clinical CT scans with an acquisition time of up to 0.25 s, it is no longer feasible for CBCT scans with an acquisition time of 60 s. The patient may not be able to hold his breath this long. Audiovisual coaching can help to make the breathing pattern more regular. Another approach is the so-called gating. Here, a motion surrogate is used that links each projection angle to a respiratory state, e.g. max. inhale or max. exhale or something in between. Gating is used prospectively during the acquisition or retrospectively during image reconstruction.

Prospective and Retrospective Gating

Prospective gating aims to consider motion during acquisition. It requires a motion surrogate that is recorded externally during acquisition. This signal can be used to only acquire projections in a specified motion state. In this case, the temporal resolution is increased but the total acquisition time increases as well. This is not desirable for the patient and reduces the number of patients that can be treated per day. The motion signal can also be used to only activate the irradiation when the target is in a desired location (Jiang 2006) or to track the target (Tacke et al. 2010). Retrospective gating is done after acquisition at image reconstruction. Here, data for all motion states were recorded and a motion surrogate signal is used afterwards to sort the projections into their respective motion bins. This sorting process is called binning. In contrast to prospective gating, an external motion surrogate that is recorded during acquisition can be used but is not necessary. It can be derived from the raw data in a process called intrinsic gating, which is described later in Sec. 2.4.4. In this thesis, no prospective scans were used and only retrospective gating was used.

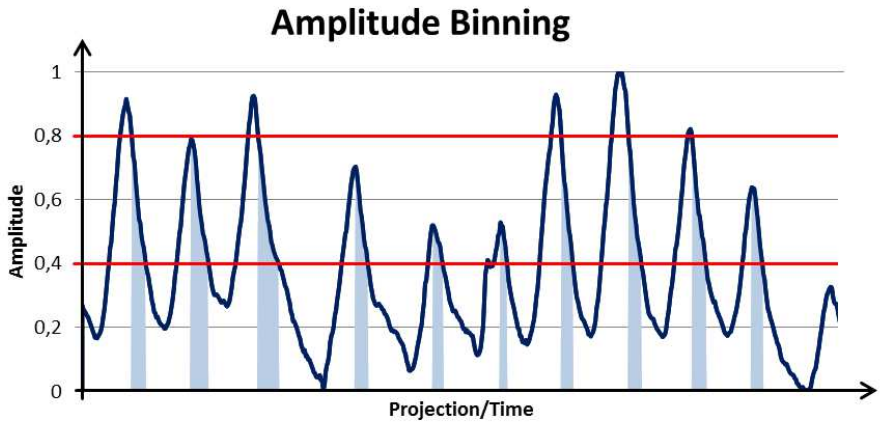

Figure 29.: Example of amplitude binning of a respiratory surrogate signal that is normalized to [0,1]. Here, all projections with an amplitude between 0.4 and 0.8 are sorted into the same motion bin. Since inhalation and expiration follow different motion patterns, which is called respiratory hysterese, only projections in the exhale phase were selected.

Phase and Amplitude Binning

If a motion surrogate is available, it can used for binning in two distinct ways called phase binning and amplitude binning (Sauppe et al. 2018). For amplitude binning, the motion surrogate is normalized to an interval [0,1]. This interval is divided into motion bins of equal size and projections are sorted into their respective bin (Fig. 29). The advantage of this method is that each projection bin has a good temporal resolution. For the reconstruction the angular distribution of projections within a motion bin is of great importance. Too large angular gaps lead to undersampling artifacts. With amplitude gating, large angular gaps may occur if the respiratory motion amplitude of the patients varies strongly between respirations. This can partly be fixed by using dynamic windows that are designed in a way that all motion bins contain a comparable number of projections. The drawback is a loss of temporal resolution. The other way to do the binning is called phase binning. Here, only the peaks of the motion surrogate, e.g. max. inhale or max. exhale, are of importance. From the peaks, a saw-tooth signal is created that increases linearly from 0 to 1 between peaks. This saw-tooth signal is then used for binning (Fig. 210). The advantage of this method is improved angular coverage. The drawback is the loss of temporal resolution, since the absolute amplitude is disregarded. A recent approach by Sauppe et al. 2018 showed good results by combining phase and amplitude gating in order to get a good angular coverage and maintain a good temporal resolution. Even though respiratory gating was only covered in this section, it can be done for the cardiac signal as well.

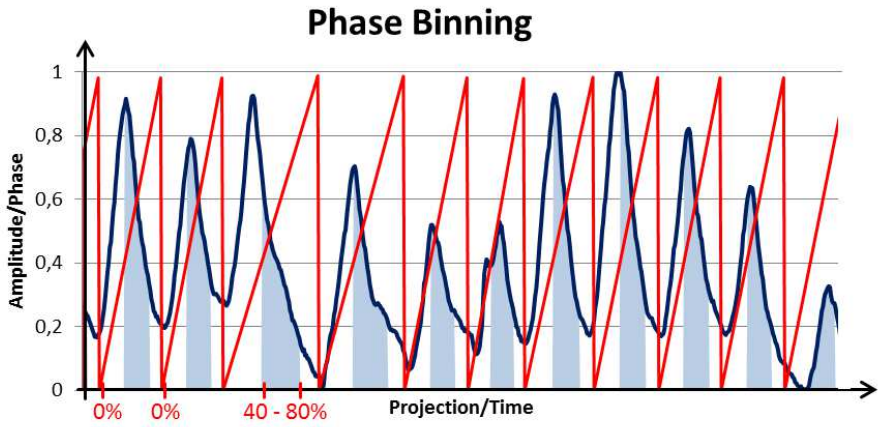

Figure 210.: From the peaks, in this case max. exhale, of the amplitude signal a saw-tooth signal (red) that increases linearly between peaks is created. The phase signal is used to sort projections into motion bins. Here, all projections where the phase signal is between 0.4 and 0.8 are sorted into the same bin.

Motion Management

The easiest way to account for motion is to only use projections from the same motion bin for reconstruction. This so called gated reconstruction leads to a sharp image with strong undersampling artifacts, since only a fraction of the original data was used for reconstruction (Fig. 28, right). Algorithms that incorporate information from all phases to reconstruct a desired phase are called motion compensation (MoCo) algorithms (Sonke et al. 2005; Dietrich et al. 2006; Li et al. 2006; Lu et al. 2007; Wang and Gu 2013; Brehm et al. 2012; Brehm et al. 2013; Yan et al. 2014; Brehm et al. 2015; Dang et al. 2015; Biguri et al. 2017; Zhang et al. 2017). First, a 4D gated reconstruction is done. Let N be the number of motion bins. For each motion bin n a gated reconstruction is done resulting in the so-called phase correlated image I_n. Based on I_n, motion vector fields (MVF) are estimate that map the volumes of the different phase onto each other using some kind of registration algorithm. The scheme of the cyclic motion compensation by Brehm et al. 2012 is shown in Fig. 211. Here, T^n_{n-1} is the MVF that maps I_{n-1} onto I_n. Notice how MVFs are only defined between neighboring phases. A cyclic constraint makes sure that the concatenation of all MVF, which corresponds to a complete respiratory cycle, is the identity. Registration between phase correlated images is done using a deformable Demon's algorithm (Thirion 1998). This algorithm was extended by an artifact model (Brehm et al. 2013). The artifact model uses an initial 3D reconstruction that is converted into a ternary prior image similar to the one for the NMAR algorithm. It divides the volume into three classes, air, soft tissue and bone, that are assigned a fixed CT value. This volume is forward projected in the original geometry, resulting in artificial raw data without motion. These raw data are used for gated reconstruction. The phase correlated images of the prior image show undersampling artifacts but no motion and are used to estimate MVFs that only

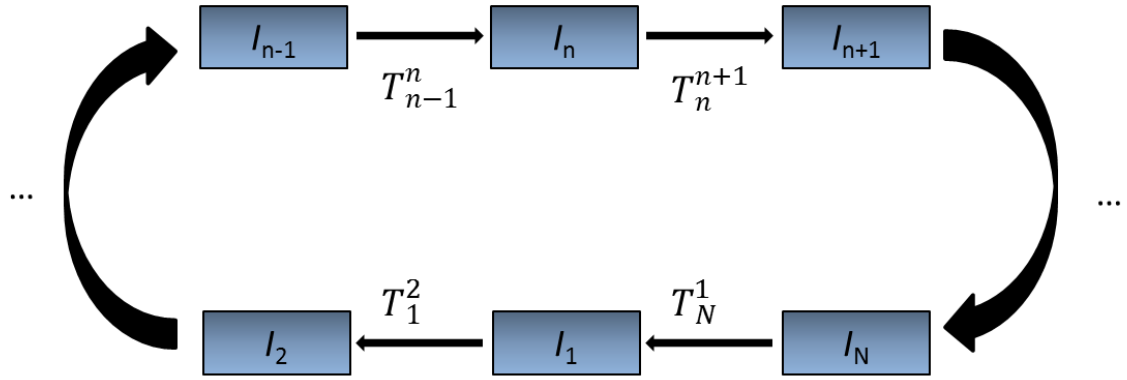

Figure 211.: Cyclic registration scheme of Brehm et al. 2012. Motion vector fields (MVFs) T^n_{n-1} that map the phase correlated image I_{n-1} to I_n are estimated using a deformable Demon's algorithm.

register the artifacts. By subtracting the artifact MVFs from the original MVFs, only anatomical motion and not the undersampling artifacts are registered. This so called acMoCo algorithm is used as a part of the newly developed algorithms for moving metal artifact reduction in the second part of this thesis.

External Motion Surrogate Acquisition

All motion compensation or gating approaches rely on a signal that correlates the projections to the respiratory or cardiac motion state. This signal can be recorded during acquisition using a respiration belt (Moser et al. 2008), a spirometer (Keall et al. 2006), a marker block or surface measurements (Bert et al. 2005; Bert et al. 2006). The external signals of the patient scans used in this thesis were recorded using the Varian Real-time Position Management (RPM) system (Varian Medical Systems, Palo Alto, USA). It tracks a marker block with reflectors that is placed on the patient using infrared cameras.

2.4.4 Intrinsic Gating

Retrieving a respiratory or cardiac motion surrogate from raw data is called intrinsic gating. It can be necessary if no external signal was recorded or if it is corrupted. Another reason for intrinsic gating is that this motion surrogate has a better correlation to the true anatomic motion than an external signal. As a study has found, the correlation between an external and an internal signal may change over time (Ge et al. 2013). The name 'intrinsic gating' can be misleading, since it is a different task than 'gating', where projections are sorted into motion bins to enable 4D reconstruction. However, the signal acquired using intrinsic gating can be used as a foundation for retrospective gating methods to sort the projections into the correct bins.

Most methods for intrinsic gating focus on respiratory gating (Dinkel et al. 2008; Farncombe 2008; Bartling et al. 2008; Hu et al. 2004; Zijp, Sonke, and Herk 2004; Van Herk et al. 2007; Kavanagh et al. 2009; Vergalasova, Cai, and Yin 2012; Dhou, Motai, and Hugo 2013) , since this is the dominant source of motion. The general idea behind behind most methods is to track the motion of the diaphragm in the projections. For the purpose of this thesis it is important to note, that none of the mentioned methods are designed for scans with a laterally shifted detector. A method that is frequently used is the Amsterdam-Shroud (AS) method (Zijp, Sonke, and Herk 2004). Here, the gradient in cranio-caudal direction is calculated on the logarithmic projections. Each projection is then condensed to a single column by projecting it onto the cranio-caudal axis. All condensed projections next to each other are called the 'Amsterdam Shroud' (Fig. 212). After taking the horizontal derivative of the Amsterdam-Shroud, which is the time derivative, the lines are shifted vertically in a way to minimize the root mean square of the pixel difference. The shift gives the respiratory motion surrogate.

Intrinsic gating is not limited to CBCT scans of the thorax region of humans. It also finds application in small animal CT, where small rodents are used as preclinical research subjects. A method designed for small rodents by Kuntz et al. 2010 uses an ROI in the projections that covers the heart and the diaphragm (Fig. 213). The center of mass within this ROI is used as a motion surrogate. The position of the ROI is determined automatically using variational analysis from the data of multiple rotations. The method can be used for respiratory and cardiac gating. While there is an algorithm for cardiac gating for humans for spiral scans (Kachelrieß et al. 2002), there is no algorithm dedicated to intrinsic cardiac gating in CBCT scans of humans. Due to recent advances in the field of motion compensation Sauppe et al. 2016b, that allows for the simultaneous correction of respiratory and cardiac motion, such a signal is highly desirable, since it is not common to record an ECG while the patient is scanned. The goal of the algorithm for intrinsic gating aims to estimate a respiratory and a cardiac motion surrogate in a fully automatic fashion. Additionally, it has to be applicable for scans with or without a laterally shifted detector.

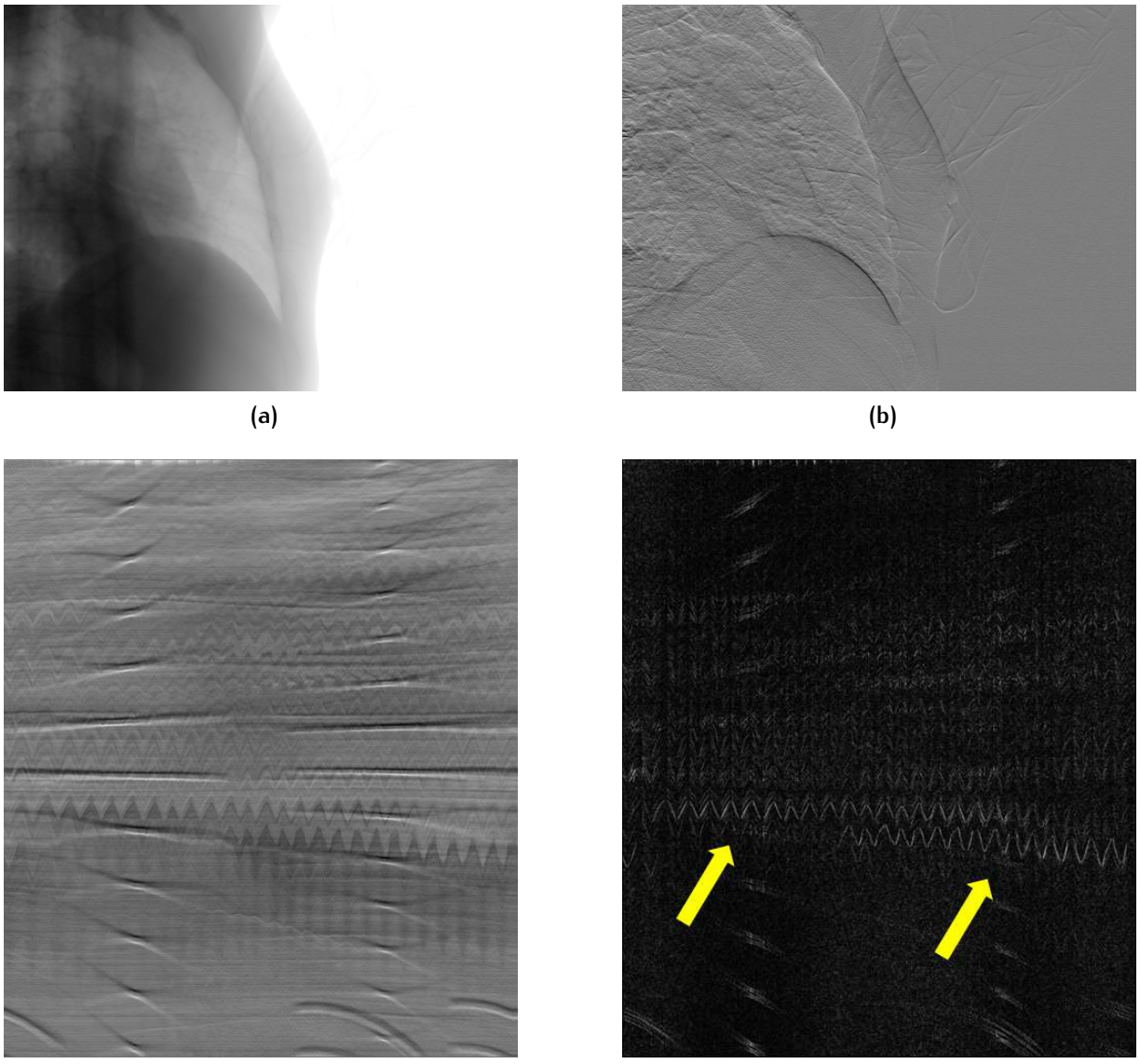

Figure 212.: Steps of Amsterdam-Shroud (AS) method (Zijp, Sonke, and Herk 2004). (a) First, the logarithm of the projection values is taken. (b) Next, the derivative in cranio-caudal direction is calculated. (c) Each projection is condensed into a single column. All condensed projections next to each other is called the Amsterdam shroud. (d) The horizontal derivative of the Amsterdam shroud is calculated. The yellow arrows indicate the position of the diaphragm. From this, the rows are shifted to minimize the root mean square of the pixel difference. The shift is the desired signal. Note that not both hemidiaphragms are visible in all columns, since the example here is recorded using a laterally shifted detector.

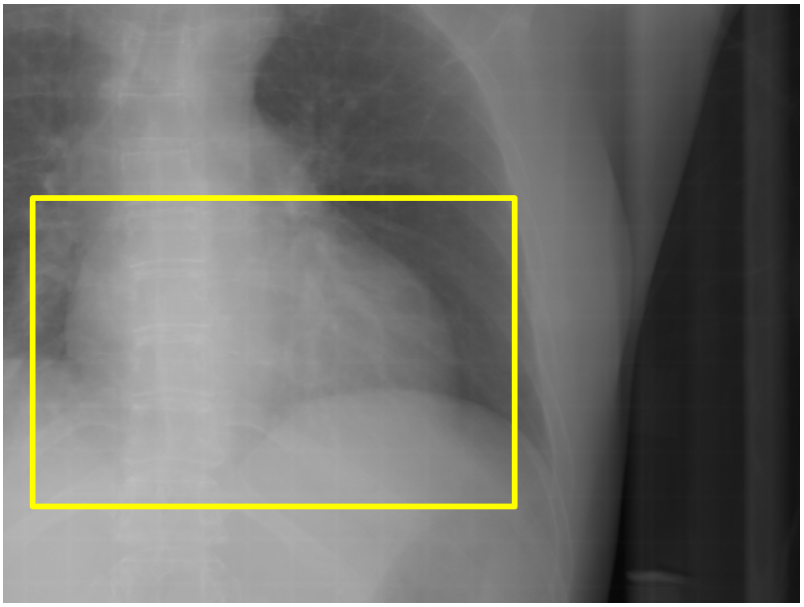

Figure 213.: For the method by Kuntz et al. 2010, an ROI that covers the heart and the diaphragm is selected automatically by comparing projections from the same direction from different rotations. The position of the center of mass within the ROI gives the desired motion surrogate.

3. Materials and Methods

In this thesis, algorithms were developed in two main fields: Intrinsic gating (IG) and moving metal artifact reduction (MMAR). Since intrinsic gating can be a prerequisite for some of the MMAR algorithms, it is introduced first in section 3.1. New algorithms for MMAR are introduced in section 3.2. The algorithms were published in Hahn and Kachelrieß 2018; Hahn, Sauppe, and Kachelrieß 2016; Hahn, Knaup, and Kachelrieß 2018 (IG) and Hahn et al. 2018b; Hahn et al. 2018a (MMAR) or submitted for publication (Hahn et al. 2019).

3.1 INTRINSIC GATING

The algorithm for intrinsic gating shall fulfill the following requirements:

- It works fully automatically.
- It takes the raw data as an input.
- It gives a surrogate motion signal as an output.
- It works on scans with and without a laterally shifted detector.

While the first two requirements are self-explanatory, the latter two need some explanation. In section 2.4.3 phase gating and amplitude gating were introduced. With a laterally shifted detector, amplitude gating is not feasible for the following reason: The left and the right hemidiaphragm do not necessarily have the same position in longitudinal direction. They move synchronously but usually the right hemidiaphragm is higher than the left (O'Brien 1928) (Fig. 31a). Conventional methods for respiratory gating are designed for scans where the left and the right hemidiaphragm are visible at all times. This is, however, not the case if the detector is laterally shifted. The projection recorded in anterior-posterior direction might cover only the left hemidiaphragm (Fig. 31b) while the projection in posterior-anterior direction only covers the right hemidiaphragm (Fig. 31c). This is why there will be a shift in any intrinsically determined amplitude signal. For this reason, the algorithm introduced in this chapter is used for phase gating. It is, however, not limited to phase gating and can also be used for amplitude gating if scans without a shifted detector are available.

The algorithm can be divided into three parts:

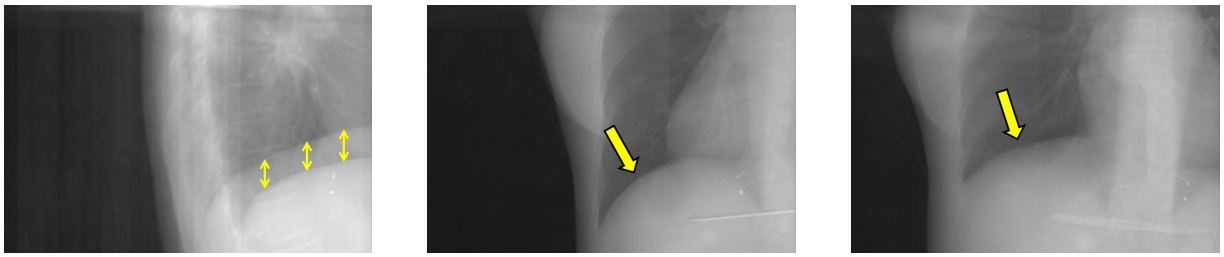

(a) (b) (c)

Figure 31.: Projections acquired with a laterally shifted detector. (a) View in lateral direction. Both hemidiaphragms are visible. The yellow arrows indicate the difference in the craniocaudal direction. (b) View in anterior-posterior direction. Only the left hemidiaphragm is visible. (c) View in posterior-anterior direction. Only the right hemidiaphragm is visible. The arrows in (b) and (c) mark the position of the respective hemidiaphragm.

1. A preprocession step, where the raw data are modified in a way to only show regions that are subjected to motion. This step is covered in Sec. 3.1.1.
2. A step, where a large number of possible motion surrogate candidates is generated (Sec. 3.1.2).
3. A final step, where the resulting motion surrogate is chosen from the candidates (Sec. 3.1.3).

The steps described in said sections are used to obtain a respiratory surrogate. With only a small modification of the algorithm, the cardiac signal can be obtained as well. This is described in Sec. 3.1.4.

3.1.1 Preprocession

The projection, from which the motion surrogate is to be acquired, show a mix of regions that move like the diaphragm or the ventricular wall and regions that are mostly static like the spine. For this purpose, only regions that are subjected to motion are of interest. It is therefore desirable to divide the raw data p into a static part p_{stat} and a dynamic part p_{dyn}, that contains all motion information:

$$p = p_{\text{dyn}} + p_{\text{stat}}. \tag{31}$$

In order to compute p_{dyn}, a static background p_{stat} that can be subtracted from the original raw data p is calculated using the following technique: The original raw data are reconstructed using the standard Feldkamp-Davis-Kress (FDK) reconstruction (Feldkamp, Davis, and Kress 1984). Since the reconstruction X^{-1} and the forward projection X are inverse operations, the original raw data can be obtained by forward projecting the reconstructed volume. This is possible because the motion information is encoded in the volume in artifacts with a small amplitude. To break this relation

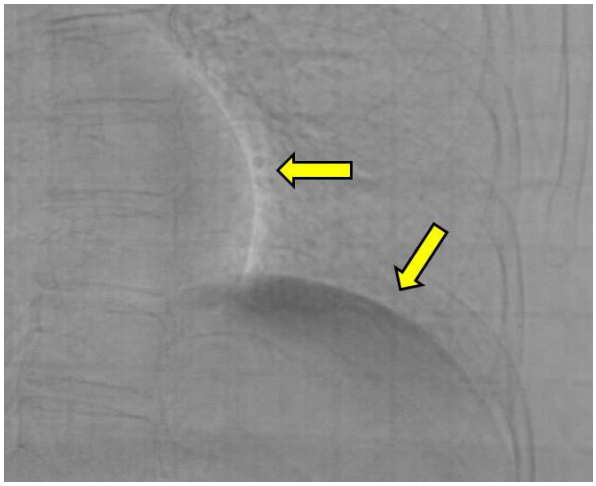

Figure 32.: Here, a selected region of a projection of the dynamic raw data p_{dyn} is shown. The yellow arrows indicate dark/bright areas that appear due to the respiratory and cardiac motion. Adopted from Hahn et al. 2019.

and to get the projections that correspond to a static volume, a 5×5 Median filter M is applied on the reconstructed volume before forward projection. This way motion information in the volume is reduced and these new projections show less motion as well. They serve as the desired static background p_{stat}.

$$p_{\text{stat}} = \text{XMX}^{-1}p \tag{32}$$

In the static raw data p_{stat} the diaphragm does not move, is blurred and somewhere between max. inhale and max. exhale. By subtracting the static background p_{stat} from the original raw data p, anatomic background that is not subjected to motion is removed. Static regions in p_{dyn} are around zero. Regions where motion occurs like the diaphragm or the ventricular wall shows positive or negative contributions, depending on the motion state (Fig. 32). All calculations in the following sections are carried out on the dynamic raw data p_{dyn}. The necessity of this preprocession step is part of the evaluation.

3.1.2 Surrogate Signal Candidate Generation

A common feature of all intrinsic gating algorithms is the tracking of the diaphragm in the raw data. It is either found manually or automatically. Here, a different approach is chosen. A priori the position of the diaphragm is neither known in the reconstructed volume nor in the raw data. Each voxel in the volume can therefore be seen as a candidate for the position of the diaphragm. Instead of using all voxels as possible candidates, grid points g_V are distributed regularly over the whole volume (Fig. 33, left). Each grid point can be tracked on the detector using basic geometric calculations. Let $f : \mathbb{R}^3 \rightarrow \mathbb{R}^2 \times \mathbb{R}$ be this transformation that maps a grid

point $g_V(n_x, n_y, n_z) = (n_x, n_y, n_z)^T$, which is defined in volume, onto a series of points $g_D(n_u, n_v, n_a) = (n_u(n_a), n_v(n_a))^T$ on the detector . n_u and n_v span the detector, while n_a denotes the projection number, i.e. the source angle. Note that while the point in the volume is fixed, it corresponds to a different detector pixel for each projection angle. The following steps are performed for each grid point g:

1. g_D is calculated.
2. A rectangular region of interest (ROI) on the detector is placed around g_D for each projection n_a (Fig. 34). If g_V is located at the diaphragm, the ROI around g_D is supposed to cover the whole range of motion of the diaphragm on the detector. If g_V is not located at the diaphragm, g_V covers random anatomy and maybe the diaphragm for some projections.
3. The average gray value is calculated for each ROI. This is where the preprocession step comes into play. The greater the deviation from the average motion state, the larger the dark/bright areas, the larger/smaller the average gray value within the ROI. The average gray value for each projection constitutes the motion surrogate $s(n_a)$ for this grid point.

It is possible that depending on the grid point g_V, g_D is not on the detector for all projections, e.g. it leaves the detector to the left or right side. Even if g_D is no longer on the detector, the ROI around it might still partially be on the detector. The final motion surrogate is supposed to be complete, i.e. there has to be a surrogate for all projection angles. Hence, all grid points where only 20% or less of the ROI around g_D is on the detector for one or more projection angle, are discarded. To increase the performance of the algorithm, the dynamic raw data were rebinned by a factor of 4×4, i.e. 4×4 neighboring pixels were averaged to reduce the total number of pixels. Since the average gray value is calculated within a ROI, this rebinning step did not change the outcome of the algorithm. To further boost the performance, the grid point trajectory on the detector only needs to be computed for the grid points in one axial slice. The trace of the other grid points can be obtained using a shift in longitudinal direction.

3.1.3 Final Signal Selection

In the previous step, each grid point provides a candidate for the desired motion surrogate. In this step, the best candidate is selected. First, a band-pass filter is applied to $s(n_a)$. It is set to allow for frequencies between 10 to 30 rpm and is described in more detail in Appendix A. Next, the max. inhale peaks are determined automatically. The idea is, that a good grid point covers the diaphragm for all angles. The peaks are therefore distributed more or less regularly. If the grid point is not on the diaphragm, the peaks will be distributed randomly but not regularly. This is illustrated in Fig. 36. Peaks are determined by finding local maxima on the band-pass filtered signal. Let

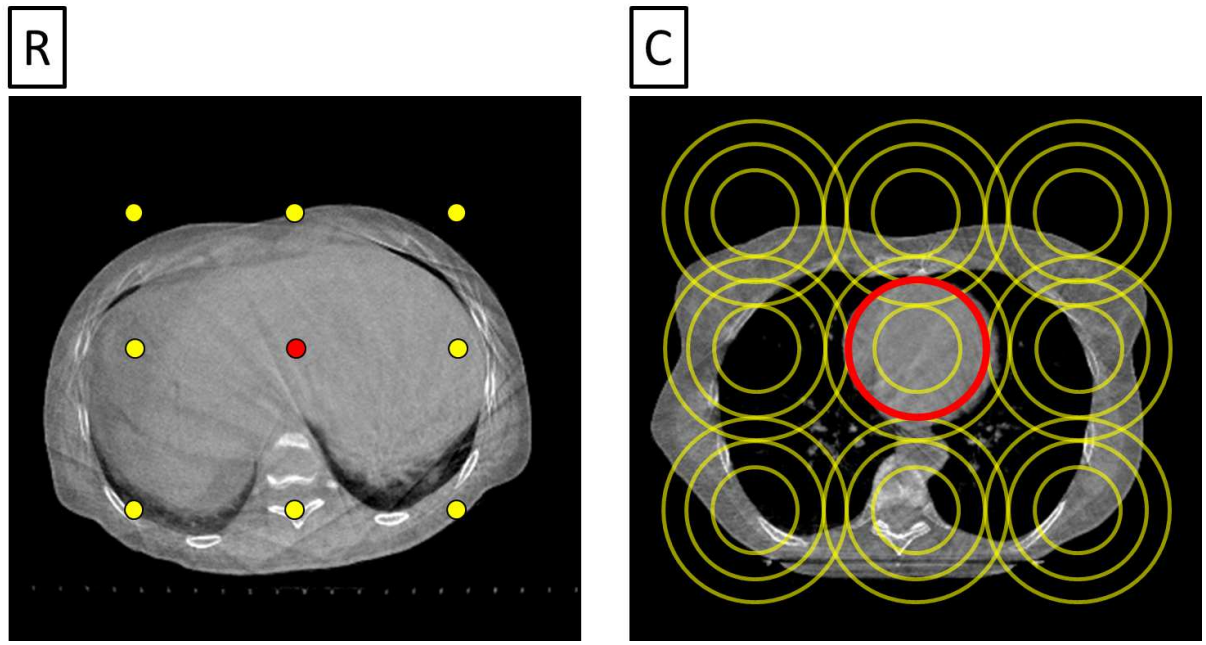

Figure 33.: Left: Grid points g_V, depicted as yellow circles, are distributed regularly in the 3D volume for respiratory gating. Here, one axial slice containing the diaphragm is shown as an example. Right: For cardiac gating, circles with different radii are distributed instead. The circles lie within an axial plane, they are not spheres. One grid point and one circle are marked red, since they will be used in the following figures. Adopted from Hahn et al. 2019.

$s_{\text{peak}}(n)$ be the position of the peaks and $\Delta s_{\text{peak}}(n)$ be the distance between the n-th and the n+1-th peak for a given signal s. In order to measure the regularity of the peaks, the standard deviation σ_s of $\Delta s_{\text{peak}}(n)$ is calculated. The signal s with the lowest standard deviation and therefore the most regular peaks is chosen as the best candidate and therefore the final result.
In Sec. 3 it was stated that this algorithm can be used for amplitude and phase gating. This becomes obvious when looking at the result. If amplitude gating is desired, s can be used. If phase gating is desired, a saw-tooth signal can be created from s_{peak}.

3.1.4 Cardiac Gating

In the previous sections, only respiratory intrinsic gating was addressed. As it turnes out, the same principle can be applied to achieve cardiac gating as well with only small adjustments. The easiest and most obvious modifications are the following: The band-pass filter has to be adjusted to typical cardiac frequencies. The number of grid points has to be increased to allow for a finer sampling of the volume. The ROIs have to be smaller, since they no longer have to cover the full range of motion of the diaphragm but the ventricular wall instead. The preprocession step remains unchanged.

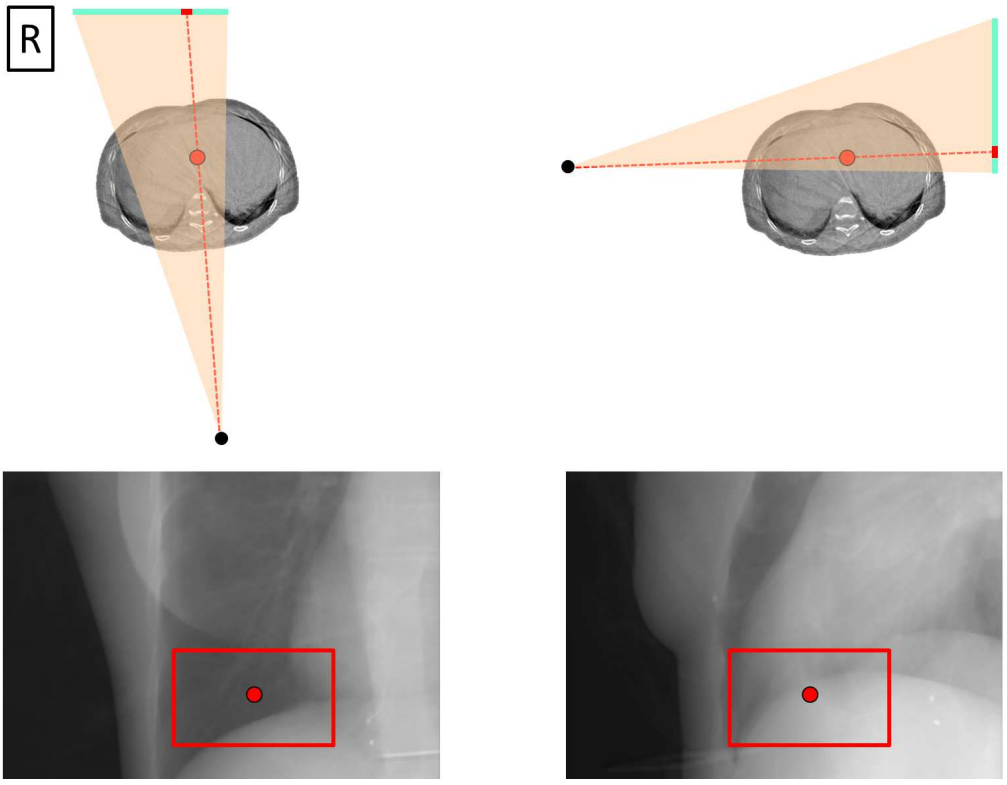

Figure 34.: A grid point in the volume g_V (top) and its counterpart g_D (bottom) are marked as yellow circles. The average gray value is calculated within the depicted ROI. Note that the projection shows the original raw data and not the dynamic raw data. This is only due to illustration purposes. The average gray value $s(n_a)$ is calculated on the dynamic raw data. Adopted from Hahn et al. 2019.

Smaller ROIs are necessary to obtain a cardiac signal but cause two new issues. The first issue is the number of grid points that result in a signal for all projections. This is a geometrical problem that is caused by the laterally shifted detector. As stated in Sec. 3.1.2, at least 20% of the ROI has to be on the detector for all projections. The number of valid grid points is therefore related to the ROI size. This leaves a very small number of viable grid points for the smaller ROIs for cardiac gating. An example of how many grid points can be used with an ROI size that is appropriate for cardiac gating is shown in Fig. 37b. With this setup, the heart would have to be in the small red area near the isocenter. As a comparison, the viable grid points for respiratory gating with a larger ROI are shown in Fig. 37a.

The second issue is best explained in a thought experiment. The goal of the experiment is to show that it is not possible to find a good grid point for cardiac gating.

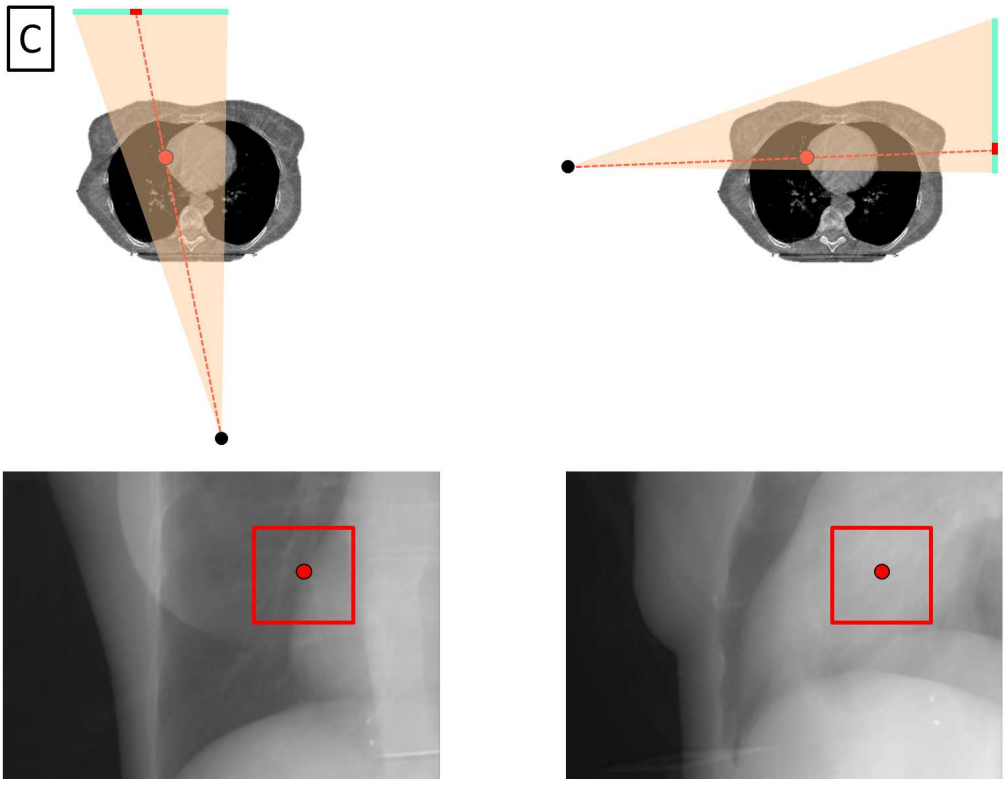

Figure 35.: The red circle depicts a grid point that is at the ventricular wall for one angle α (left), but at the center of the heart for an angle $\alpha + \pi/2$. The corresponding projections are shown in the bottom row. Adopted from Hahn et al. 2019.

For respiratory gating, the goal is to find a grid point at the diaphragm. For cardiac gating, let us assume the position of a grid point g_V is known. From an angle α, the corresponding point g_D on the detector is at the ventricular wall. At an angle $\alpha + \pi/2$ g_D is no longer at the ventricular wall but in the center of the heart (Fig. 35). Note that it is possible to have a patient scan where both issue are not problematic. If the heart is in the isocenter and there is an axial slice with a relatively small cross-section of the heart, the smaller valid area and the angular dependence are not an issue. The first because the heart is within the valid area, the latter because even the smaller ROI is big enough to cover the ventricular wall for all angles.

The solution to both issues is depicted on the right side of Fig. 33. The cross-section of the heart within an axial plane is approximately circular. So instead of tracking the original grid points, it is calculated where the tangent to a circle around the grid point intersects the detector. Here, each grid point represents the center of a circle. Since the radius of the circle is not known a priori, multiple circles with different radii are calcu-

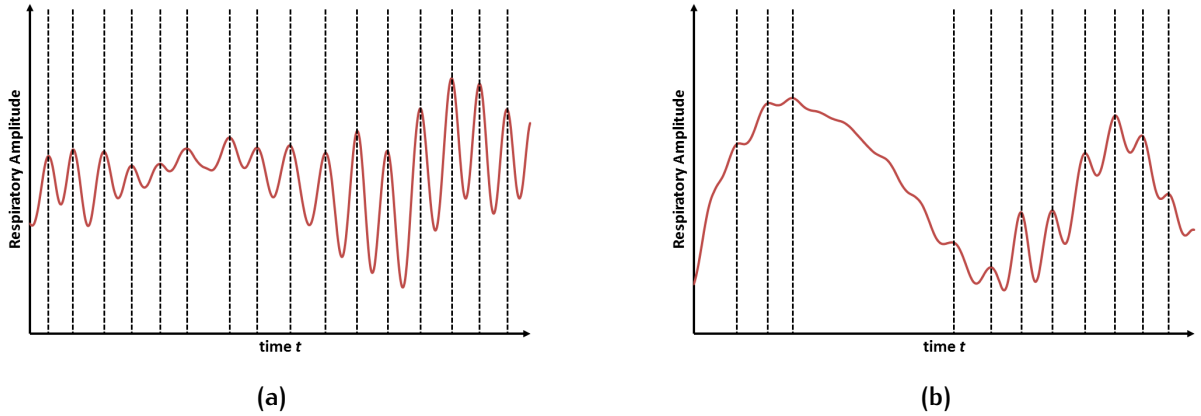

Figure 36.: In (a), the signal s from a grid point on the diaphragm is depicted. The peak positions are indicated by the vertical dashed lines. Here, the peaks are distributed farily regularly. In (b), the signal s from a grid point that is not on the diaphragm is shown. While it was possible to see the respiratory signal for some projections, it does not show in all. This is why the detected peaks have a large gap and the standard deviation of the peak distance is much higher as a consequence. Adopted from Hahn, Knaup, and Kachelrieß 2018.

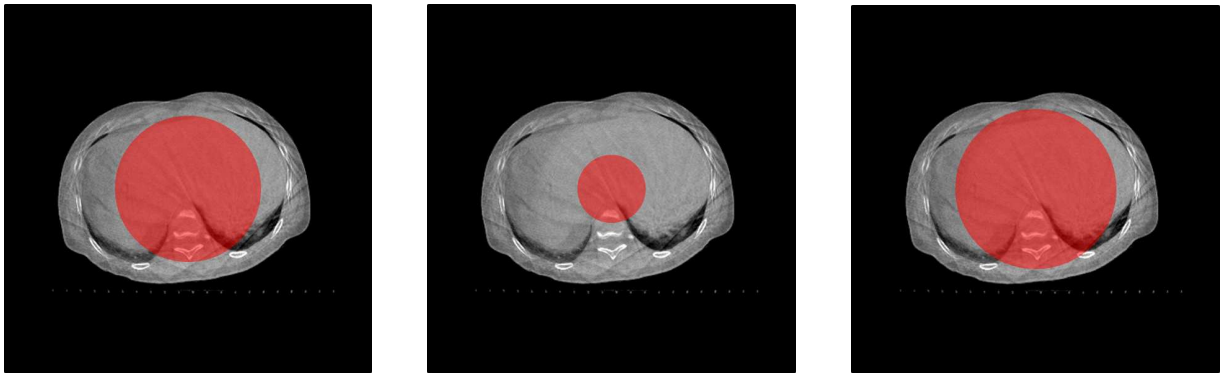

Figure 37.: (a) The red circle indicates the area where grid points give a signal s for all projection angles with an ROI size of 200px × 100px (77.6 × 38.8 mm that is used for cardiac gating. In order for the method to work, the heart needs to be within the red area. (b) Same as (a) but with an ROI size of 300px × 300px (116.4 mm × 116.4 mm) that is used for respiratory gating. The valid area is much larger. (c) Same ROI size as in (a). Here, circles are used instead of grid points. Now the viable area is sufficiently large.

lated for each grid point. Using circles instead of grid points significantly increases the area in the reconstructed volume where the heart can be found despite using smaller ROIs (Fig. 37c). Additionally, the ROI can now cover the ventricular wall for all angles (Fig. 38).

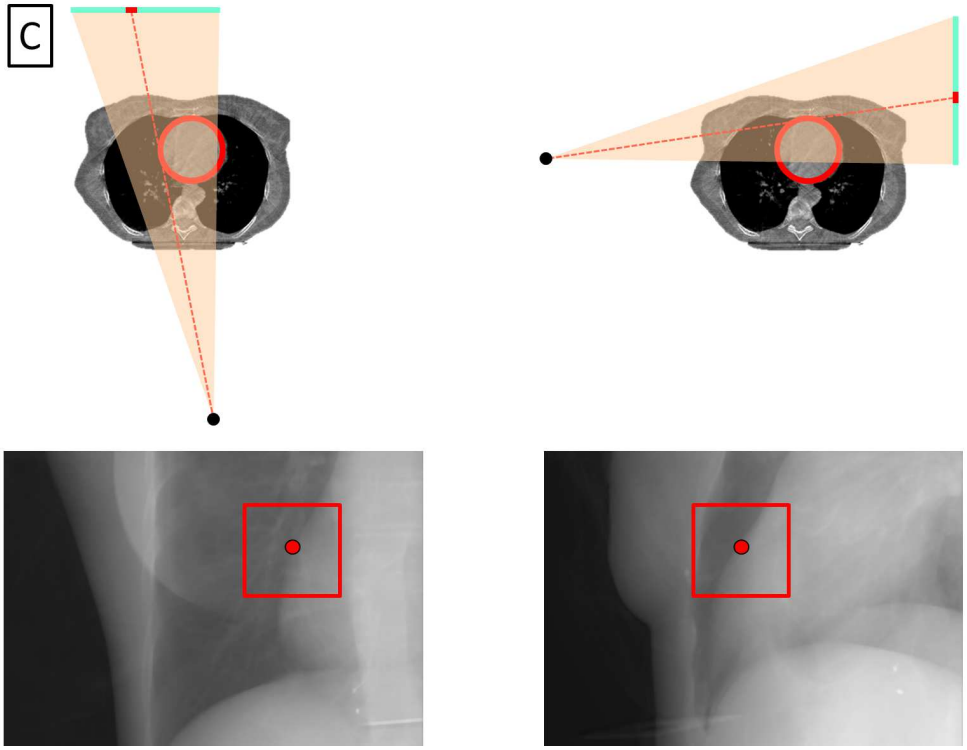

Figure 38.: For cardiac gating, the tangent to a circle is tracked on the detector instead of a grid point. This way the ventricular is within the ROI from all angles. Adopted from Hahn et al. 2019.

3.2 MOVING METAL ARTIFACT REDUCTION

In this chapter, three algorithms for moving metal artifact reduction are introduced. The first algorithm is called MMAR and is a refined version of an algorithm that was already presented at RSNA 2011 (Brehm et al. 2011). It was published in Medical Physics (Hahn et al. 2018b) and is an extension of classical metal artifact reduction methods but does not use techniques from the field of motion compensation. It is described in Sec. 2.4.2. The other algorithms, called MoCoMAR1 and MoCoMAR2, are original work within the scope of this thesis. They have been published in Medical Physics (Hahn et al. 2018b) or were presented at the ECR 2018 (Hahn et al. 2018a), respectively. Both combine the fields of metal artifact reduction and motion compensation and are presented in Sec. 3.2.2 and Sec. 3.2.3. An overview over the algorithms is shown in Tab 31.

Table 31.: Overview of methods for moving metal artifact reduction

Name	Utilizes MoCo	Result	Original Work within this Thesis
MMAR	no	3D Volume	no (but got refined)
MoCoMAR1	yes	3D Volume	yes
MoCoMAR2	yes	4D Volume	yes

3.2.1 MMAR

There are two main reasons why conventional MAR algorithms fail for metal inserts that are subjected to motion.

1. It is difficult to segment metal in the raw data, because it is superimposed with human anatomy. This is why most MAR algorithms use a threshold based metal segmentation in an initial, uncorrected reconstructed volume. There, static metal is easily segmented due to its high attenuation value. Moving metal on the other hand is smeared in the volume and can have attenuation values that are too low for conventional segmentation.

2. After the segmentation in the volume, conventional approaches use a forward projection to segment the metal in the raw data. For moving metal, this yields two problems: Since the metal is smeared, the metal mask in the raw data is too big and too many pixels will be replaced. On the other hand it might also be too small at the same time, if not the whole range of motion is covered.

The solution to the first issue is a novel approach within the scope of this thesis. Instead of using just one threshold to segment metal in the reconstructed volume, two thresholds are utilized. They are set to T_1 = 2000 HU and T_2 = 800 HU. While everything above T_1 can be considered metal, smeared metal can be in the range between T_2 and T_1, as well as bone or streaking metal artifacts. To exclude bone from this mask, a floodfill algorithm is utilizes after some morphological operations and the sizes of the connected regions in the mask calculated. To large regions are discarded as bones. Also, regions in the proximity of metal are discarded as metal artifacts. This is illustrated in Fig. 39.

The second issue is handled with the algorithm proposed by Brehm et al. 2011. The raw data are being reconstructed using a standard FDK reconstruction. Metal is segmented using the two thresholds as described above. The metal mask in the volume is forward projected to obtain a metal mask in the raw data. It is dilated to be sure to cover the full range of motion. While it is not possible to find the metal in the complete raw data in a reliable way, it is much easier if a smaller region, i.e. the dilated mask, that includes the metal is known. In this region, a 2D Sobel filter is applied to find the sharp metal edges. Otsu's algorithm is applied projection-wise to automatically detect an appropriate threshold for the metal edges. The final metal mask in the raw data

(a) Sagittal plane of volume f

(b) $f \geq T_1$

(c) $T_1 > f \geq T_2$

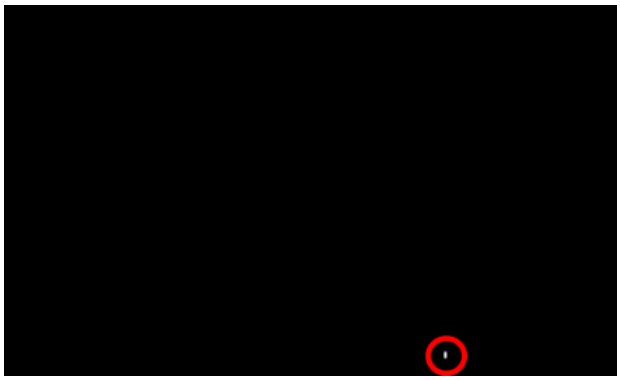

(d) $T_1 > f \geq T_2$, after bone and streak removal

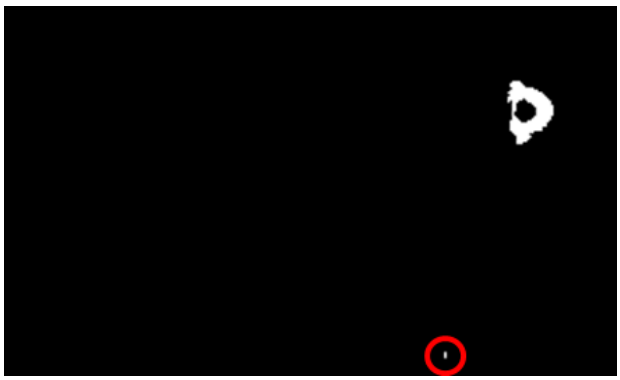

(e) Final metal mask

Figure 39.: (a) The depicted patient has a pacemaker and a cylindrical gold marker (red circle). Here simple threshold-based segmentation is not possible. The pacemaker is well above the threshold of $T_1 = 2000$ HU and can easily be segmented (b). The gold marker can be segmented using an additional threshold $T_2 = 800$ HU. Everything between T_1 and T_2 is shown in (c). Besides the gold marker, bone and artifacts in the proximity of the pacemaker are segmented as well. Big connected regions and regions in the proximity of the pace maker are removed (d). The final mask including the pacemaker and the gold marker is shown in (e). C=250 HU, W=1000 HU in all images. Adopted from Hahn et al. 2018b.

is obtained after morphological operations. All pixels in this mask are replaced using row-wise linear interpolation. After that, the interpolated raw data are reconstructed. The resulting volume contains neither metal artifacts nor metal, which is why the originally segmented metal is reinserted. The complete algorithm scheme is depicted in Fig. 310.

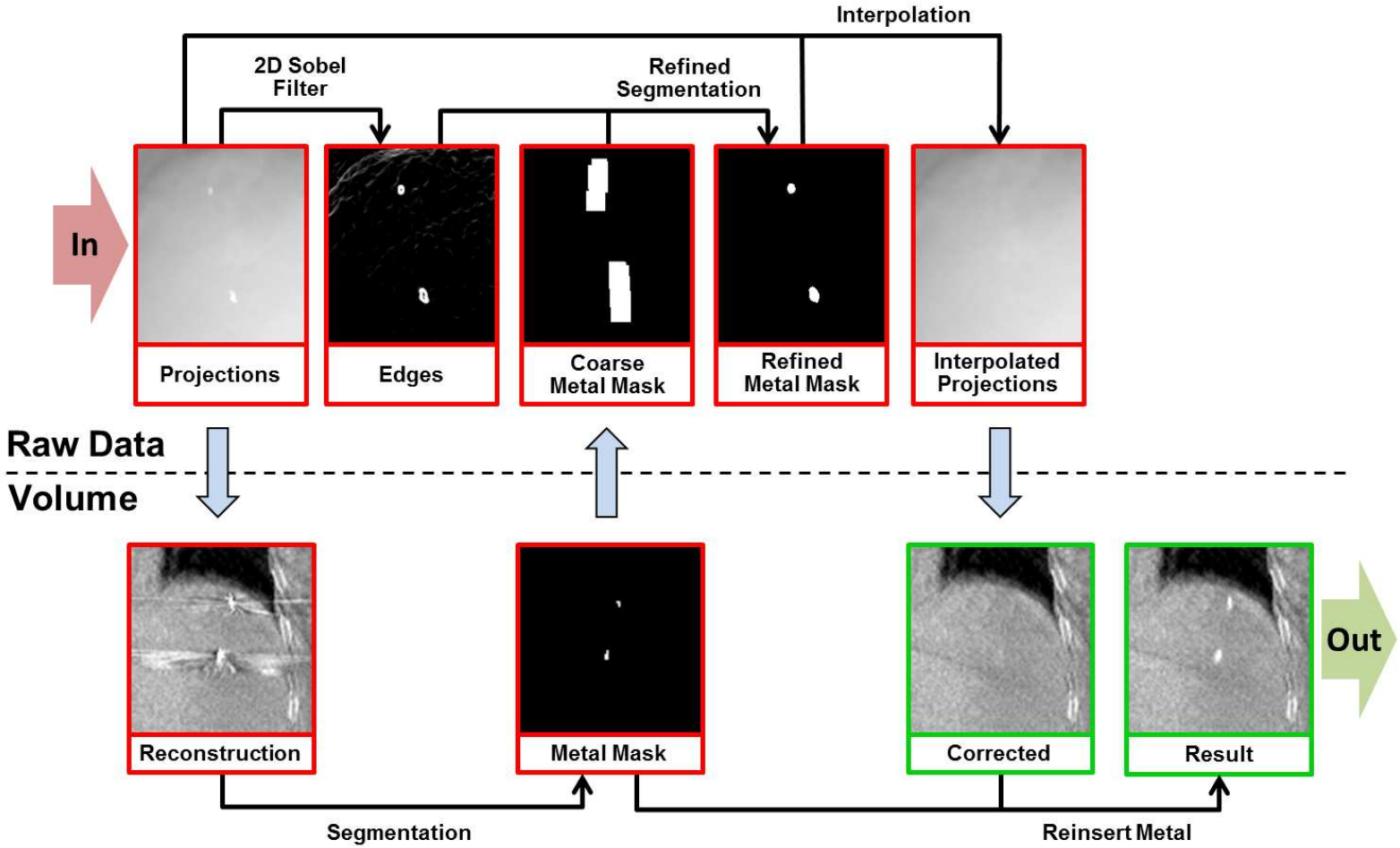

Figure 310.: Scheme of MMAR. After an intial metal segmentation in the volume, a coarse metal mask in the projections is created by forward projection and dilation. Inside this mask, the metal edges are identified using a Sobel filter. Otsu's algorithm provides suitable thresholds for each projection to separate metal edges from anatomy. Morphological operations provide the final mask which is used for linear interpolation. The original metal is reinserted to reconstructed metal free projections. Adopted from Hahn et al. 2018b.

3.2.2 MoCoMAR1

MoCoMAR1 utilizes a combination of the acMoCo algorithm (Brehm et al. 2013) described in Sec. 2.4.3 and the NMAR algorithm (Meyer et al. 2010) (Sec. 2.4.2). For convenience, they are briefly summarized here again.
The acMoCo algorithm works as follows: First, a respiratory-gated reconstruction is performed which results in a set of highly undersampled volumes, each corresponding to a different respiratory motion state. Volumes of adjacent motion phases are mapped onto each other using deformable registration. This map is called motion vector field (MVF). An artifact model prevents that motion artifacts are registered instead of the anatomy. The MVFs are used to warp the undersampled, gated volumes to a desired motion phase. As a result, the volume in the desired motion phase has strongly reduced motion artifacts and is no longer undersampled, because data from all phases were used.
In the NMAR algorithm, metal is segmented in an initially reconstructed volume using a threshold. From the metal mask in the volume, as metal mask in the raw data is obtained using forward projection. The initial volume is converted to a ternary image, that divides the volume into air, soft tissue and bones. Each class is assigned their average gray value, except for bones which remain unchanged. In a normalization step, the original raw data are divided pixel-wise by the forward projection of the ternary volume. After linear interpolation of the metal, the interpolated raw data are multiplied by the forward projected ternary raw data and an artifact free volume is reconstructed. The originally segmented metal is then reinserted.
MoCoMAR1 combines these algorithms in the following way: The acMoCo algorithm is used to obtain a 4D volume without motion artifacts. In this volume, metal can be segmented more easily, because it is no longer smeared. As a result, the position of the metal is known in the volume for each motion state. A 4D metal mask in the raw data is created by forward projection of the 4D metal mask in the volume. From the motion surrogate signal that is also used for the acMoCo algorithm, the respiratory state for each projection is known. The metal mask in the original 3D raw data is obtained by using the metal mask the corresponds to the motion state of the respective projection. Using this respiratory sensitive metal mask, the NMAR algorithm can be used for metal artifact reduction. Note that the motion surrogate was either recorded externally or is retrieved using the newly developed intrinsic gating algorithm from Sec. 3.1. The complete scheme of the algorithm can be found in Fig. 311.

3.2.3 MoCoMAR2

The result of MoCoMAR1 is a 3D volume without metal artifacts but with motion artifacts. The idea of a 4D volume without metal artifacts and without motion artifacts suggests itself, since motion compensation is already part of the algorithm. This idea is implemented in MoCoMAR2. Starting with the 4D volume provided by the acMoCo

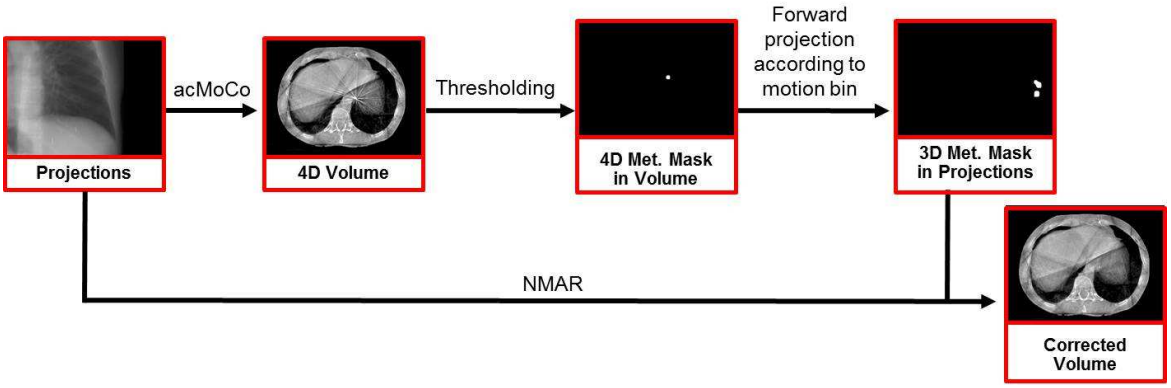

Figure 311.: The acMoCo algorithm is used to obtain a 4D volume with high spatial resolution that still contains metal artifacts. Here, a 4D metal mask in the volume is created using simple threshold-based segmentation. The forward projected mask of the respective motion state is selected projection-wise to obtain a 3D metal mask in the original raw data. This mask is then used for the NMAR algorithm. Adopted from Hahn et al. 2018a.

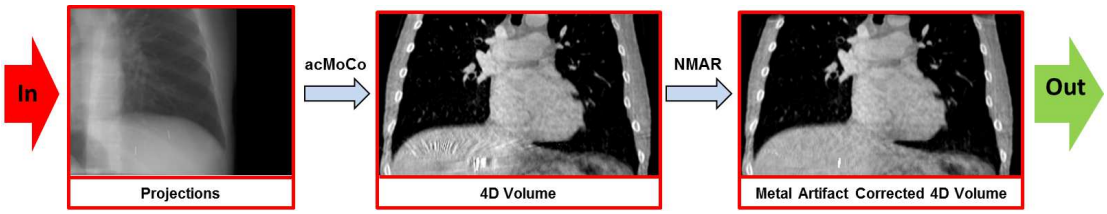

Figure 312.: Scheme of MoCoMAR2. The acMoCo algorithm and the NMAR algorithm are applied sequentially to obtain a 4D volume without motion artifacts or metal artifacts. Adopted from Hahn et al. 2018b.

algorithm, a new set of 4D raw data is created by forward projection. They can then be used for the NMAR algorithm to obtain a 4D volume without motion and metal artifacts. The workflow is illustrated in Fig. 312.

4. Results

In this chapter, the results of the novel algorithms are presented. First, the intrinsic respiratory gating (Sec. 4.1.1) and the intrinsic cardiac gating (Sec. 4.1.2) are being evaluated using patient scans of the thorax region. Next, MMAR, MoCoMAR1 and MoCoMAR2 are being evaluated using a simulation (Sec. 4.2.1) and using patient data (Sec. 4.2.2). Parts of the results of the intrinsic gating have been presented at SPIE 2016 (Hahn, Sauppe, and Kachelrieß 2016), CT Meeting 2018 (Hahn and Kachelrieß 2018) and RSNA 2018 (Hahn, Knaup, and Kachelrieß 2018) and are submitted for publication (Hahn et al. 2019). Part of the results of MMAR and MoCoMAR2 have been published in Hahn et al. 2018b. Parts of the results for MoCoMAR1 were presented at ECR 2018 (Hahn et al. 2018a).

4.1 INTRINSIC GATING

Ten patient scans of the thorax region were available to evaluate the efficacy of the algorithm. The scans were acquired on a Varian TrueBeam® (Varian Medical Systems, Palo Alto, Calif.) at 11 fps for five patients and 15 fps for the other five patients. The algorithm is completely independent of the number of fps. They are only factored in the bandpass filter. The scan time for all scans was 60 s with an angular coverage of 360°. The detector contained 1024×768 pixels with a size of $(0.388\text{ mm})^2$. A volume of 512×512×210 voxels with a size of $(1\text{ mm})^3$ using a standard FDK (Feldkamp, Davis, and Kress 1984) algorithm was reconstructed for the preprocession step. Due to the lateral shift of the detector of 160 mm, the field of view was increased to 46.5 cm.

4.1.1 Respiratory Gating

For the respiratory gating, a signal from the Varian real-time position management (RPM) system is available for six patients. For the other patients, the position of the respiratory peaks was determined by carefully scrolling through the projections. From the peaks, which are either from the RPM signal or the manual inspection, a saw-tooth signal is created as described in Sec. 2.4.3.
10×10×10 grid points were distributed over the volume. The ROI size was set to 300 px × 300 px (116.4 mm × 116.4 mm) and the bandpass filter set to allow frequencies between 10 and 30 rpm.
For the purpose of this evaluation, the proposed algorithm including the preproces-

Table 41.: Overview of methods that are being compared. Adopted from Hahn et al. 2019.

Abbreviation	Method
P1	Proposed method 1: Intrinsic gating using the background subtraction step and grid point tracking for respiratory gating and circle tracking for cardiac gating.
P2	Proposed method 2: Identical to P1 up to the background subtraction, which is omitted.
P3	Proposed method 3: Identical to P1 up to the cardiac gating. Here, grid points are tracked for the cardiac gating as well.
R1	Reference method 1: Amsterdam-Shroud method (Zijp, Sonke, and Herk 2004)
R2	Reference method 2: Cardiac gating for small animals (Kuntz et al. 2010)

sion step and the use of circles for cardiac gating is called P1. This is the complete algorithm. The version without the preprocession step is called P2, while the version with the preprocession step but without the use of circles is called P3. For respiratory gating, P1 is being compared to the Amsterdam-Shroud (AS) method (Zijp, Sonke, and Herk 2004) (see Sec. 2.4.4), which is commonly used for intrinsic gating. The AS method is called R1 for reference method 1 in this evaluation. An overview over all methods that are part of the evaluation is shown in Tab. 41.

Evaluation Metric

As argued in Sec. 3.1, P123 are used for phase gating (Sauppe et al. 2018). Hence, only the peaks of the final signal are important. They mark the time points of max. inhalation. From these points, a saw-tooth signal is created (Kachelrieß and Kalender 1998), that rises linearly from 0 to 1 between peaks (Fig. 41a). This signal can be used to assign each projection to a motion bin. To evaluate the proposed algorithm, the intrinsically determined saw-tooth phase signal has to be compared to a ground truth phase signal. An intuitive approach would be to take the root-mean-squared (RMS) error. The problem with this simple approach is that the ground truth and the intrinsic signal have obviously been acquired in different ways. While both provide a signal that is characteristic for the breathing pattern of the patient, there can be a constant offset between them even if both signals are perfect. This would lead to an artificially large RMS that does not reflect the quality of the result of the intrinsic gating (Fig. 41b). A constant offset can be eliminated by renaming the motion bins.
A better way to measure the accuracy of the proposed algorithm is to use a measure that accounts for the offset: the standard deviation of the distance between the peaks

(Fig. 41c). Let $s_{GT}(n)$ be the ground truth phase signal at the n-th projection, $s_{IG}(n)$ the intrinsically determined phase signal and $\Delta s(n) = s_{GT}(n) - s_{IG}(n)$. Then

$$\sigma = \sqrt{\frac{1}{N}\sum_{n=1}^{N}(\Delta s(n) - \overline{\Delta s})^2}. \tag{41}$$

The error σ is named after the respective method P1, P2 or R1, e.g. σ_{R1}. When calculating $\Delta s(n)$ the periodicity of s has to taken into account by taken the signal modulo 1.

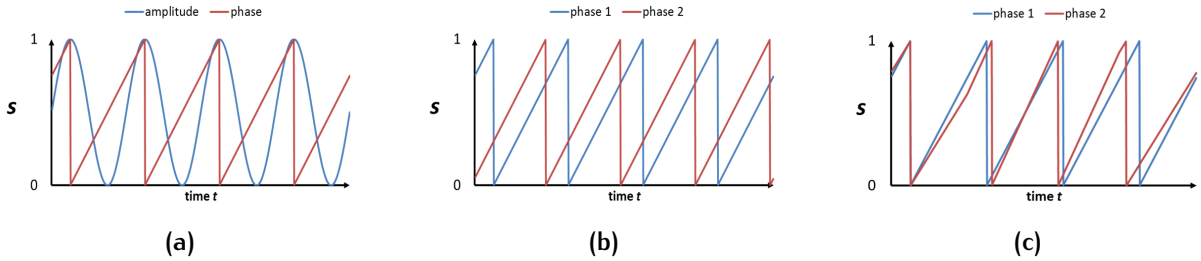

Figure 41.: (a) The phase signal (red) is a sawtooth signal, that rises linearly between two peaks of the respiratory or cardiac amplitude (blue). (b) Here two phase signals with identical slope but a small shift are shown. While the standard deviation of their difference is zero, the RMS is 0.3. This shows how the standard deviation of the difference of the phases is a reasonable measure for their similarity in a sense that both curves describe the same physical breathing. The RMS of the two phase signals in (c) is 0, while their standard deviation is 0.41. This reflects the fact that there are differences in the underlying breathing described by the two curves. Adopted from Hahn et al. 2019.

The results can be found in Table 42. P1 performed better for all cases except for patient 2. For patient 1, 9 and 10 R1 was not able to extract a proper signal. This was due to the high noise in these scans. P1 is more robust against higher noise because it evaluates a ROI in which noise cancels, whereas R1 uses edge detection, which is more prone to noise.

4.1.2 Cardiac Gating

For the cardiac gating, no external signal like an ECG was available. The number of heart beats was determined by carefully inspecting the sinogram (Fig. 42). The accuracy of this manual inspection is not high enough to evaluate exact cardiac peak positions, which is why only the number of heart beats were compared.
50×50×50 grid points were used with an ROI size of 200 px × 100 px (77.6 mm × 38.8 mm). The bandpass filter was set to allow frequencies between 50 and 120 bpm and the algorithm iterated over circle radii between 3 cm and 5 cm in steps of 2 mm.

Table 42.: Results of respiratory gating. Adopted from Hahn et al. 2019.

Patient	σ_{P1}	σ_{R1}
1	0.054	-
2	0.108	0.088
3	0.131	0.175
4	0.093	0.205
5	0.101	0.184
6	0.042	0.144
7	0.068	0.224
8	0.220	0.201
9	0.087	-
10	0.079	-

Unfortunately, there is no method for cardiac gating for humans. To have some kind of comparison, the cardiac gating was compared to a cardiac gating algorithm for small animals (Kuntz et al. 2010) (see Sec. 2.4.4). Here an ROI including the heart has to be selected manually. In order to evaluate the efficacy of the background subtraction in the preprocession step and the use of circles instead of grid points, P1 is compared to P2 and P3 as well.

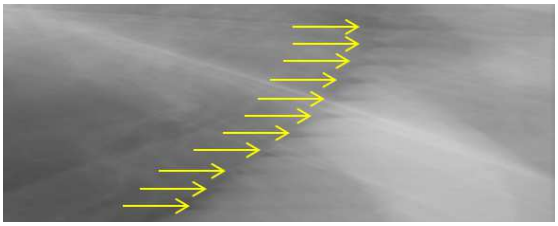

Figure 42.: Here a selected region of the sinogram through a slice containing the heart is shown. The motion of the ventricular wall can be seen this way. The yellow arrows indicate the position of maximum contraction, i.e. a new heart beat. Adopted from Hahn et al. 2019.

The results for the cardiac gating are shown in Table 43. Since the scan time was 60 s, the number of counted heart beats is also the number of beats per minute (bpm). The ground truth can be found in the second column. N_{P1}, N_{P2}, N_{P3}, N_{R2} are the number of detected heart beats by the respective methods. ΔN_{P123} are given by

$$\Delta N_{P123} = N_{GT} - N_{P123}, \tag{42}$$

with the manually counted number of heart beats N_{GT} as the ground truth.
P1 performed best for all patients with a maximum error of one heart beat. The total error in the number of heart beats for all patients was two. P2 performed equally well for six patients and slightly worse for four patients with an increased error of up to two heart beats. The total error was seven. The preprocession step was therefore able to improve the performance of the algorithm. P3 was able to obtain good results for

Table 43.: Results of cardiac gating. Adopted from Hahn et al. 2019.

Patient	N_{GT}	N_{P1}	N_{P2}	N_{P3}	N_{R2}	ΔN_{P1}	ΔN_{P2}	ΔN_{P3}	ΔN_{R2}
1	80	80	80	80	62	0	0	0	-18
2	70	69	69	73	57	-1	-1	-3	-13
3	65	65	63	85	58	0	-2	-20	-7
4	70	70	70	69	67	0	0	1	-3
5	52	52	52	56	64	0	0	-4	12
6	61	61	60	61	60	0	-1	0	-1
7	78	78	78	80	57	0	0	-2	-21
8	69	69	70	53	64	0	1	16	-5
9	86	85	84	55	61	-1	-2	31	-25
10	74	74	74	74	67	0	0	0	-7
		$\sum_{i=1}^{10} \lvert\Delta N\rvert$				2	7	77	112

five patients with a maximum absolute error of two, medium results for two patients (max. absolute error of four) and failed completely for three patients leading to a total summed absolute error of 77. The difference between P1 and P3 is that P3 tracks the trajectory of the grid points whereas P1 tracks the trajectory of the tangent to a circle. This greatly improved the performance of the algorithm. R2 performed worse for all patients compared to P1 and P2 with deviations of up to 25 heart beats. The total summed absolute error was 112. It was expected that observing the ventricular wall, as P1 and P2 do, instead of the complete heart, as R2 does, provides much more precise results. R2 was designed for small animals and does not seem to work properly for humans.

4.2 MOVING METAL ARTIFACT REDUCTION

Most results in this section have been published in Hahn et al. 2018b. The new proposed algorithms MoCoMAR1, MoCoMAR2 were compared against MMAR by Brehm et al. 2011 and a standard inpainting-based MAR by Kalender, Hebel, and Ebersberger 1987, that does not account for motion. Unfortunately the moving metal artifact reduction method by Toftegaard et al. 2014 (see Sec. 2.4.2), which will be called MMAR2 from now on, was not available. In order to compare it to the proposed methods, a best-case scenario using the simulation was implemented and evaluated. MMAR2 utilizes a complex scheme to segment cylindrical and spherical markers in the rawdata. From this, a 3D marker model is created. Since the 3D position, size and orientation of the markers are known for the simulation, the case where MMAR2 was able to find the perfect marker model was tested.

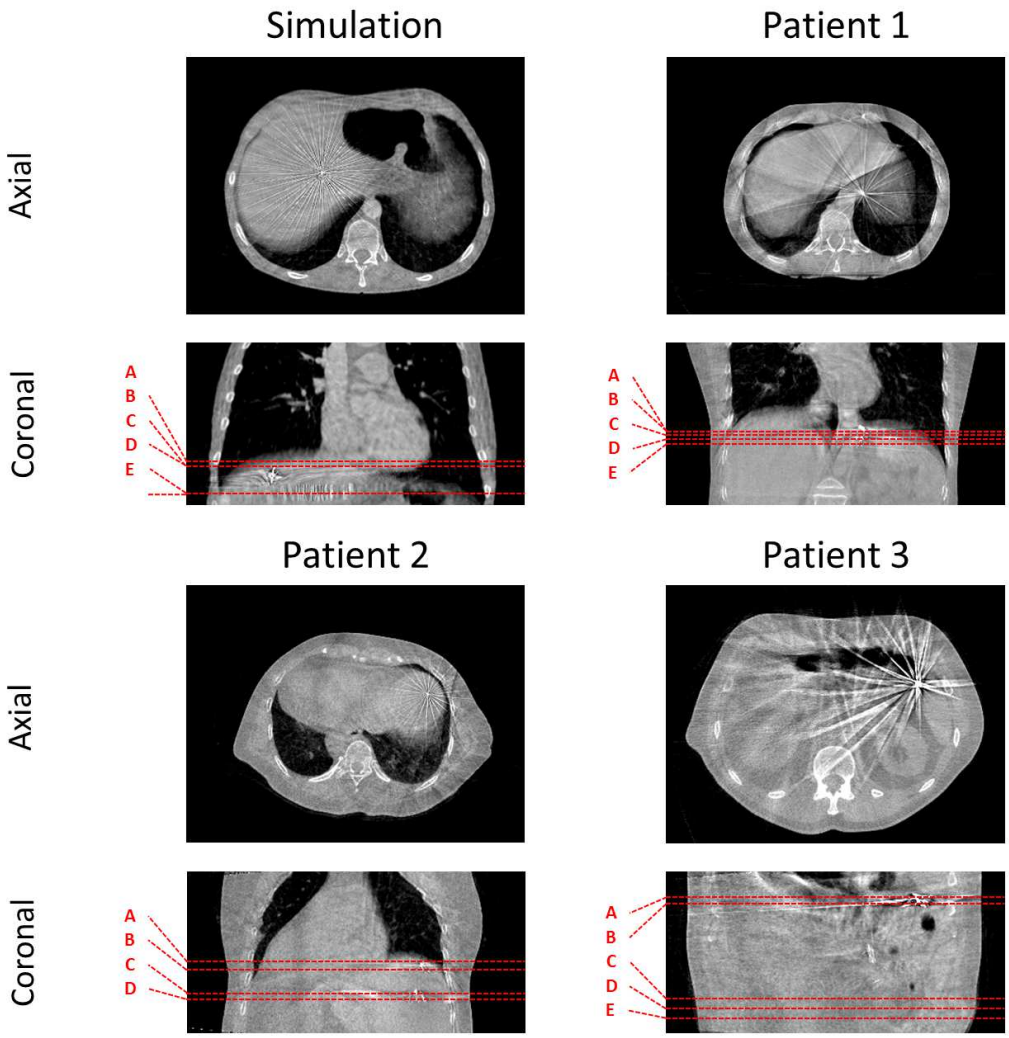

Figure 43.: Axial and coronal view of simulation and patients 1-3. The slices indicated by A-E are shown in the following figures. $C = 0$ HU, $W = 1500$ HU. Adopted from Hahn et al. 2018b.

An overview over the slices shown in the results for the simulation and patients is shown in Fig. 43.

4.2.1 Simulation

A clinical thorax scan with a Somatom Definition Flash (Siemens Healthcare, Forchheim) of a patient was used as the basis for the simulation. The volume was deformed using realistic deformation vector fields to simulate breathing. The max. amplitude was 5 mm in posterior-anterior and 20 mm in superior-inferior direction. The respiration signal recorded by a Varian Real-time Position Management^{TM} system during a CBCT scan was used to simulate a realistic breathing pattern (Fig. 44). The amplitude can be normalized to an intervall [0,1] and a volume was created for each motion state

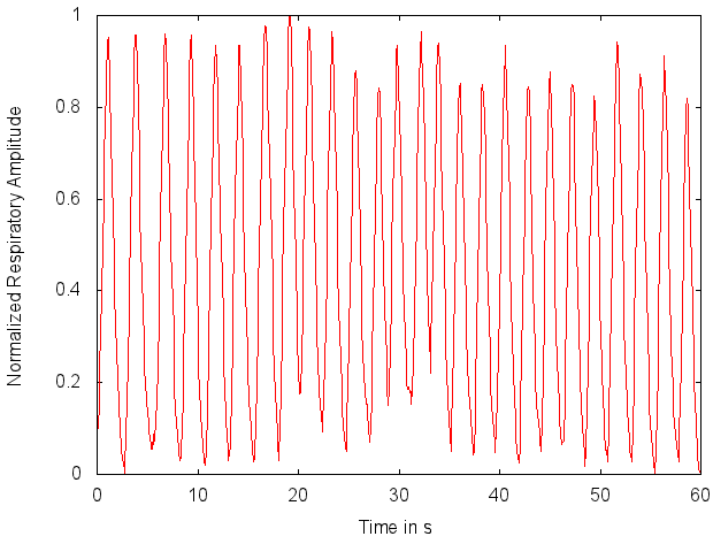

Figure 44.: Respiratory signal for simulation. Adopted from Hahn et al. 2018b.

using the deformation vector fields. The respective volumes were forward projected in the Varian TrueBeam^{TM} geometry. A rotation of 360° over 60 s at 11 fps was simulated, which leads to 660 projections. To evaluate the efficacy of the algorithms for various metal marker sizes, three small gold cylinders (length l = 3 mm, radius r = 0.4 mm) and two larger gold cylinders (l = 10 mm, r = 0.6 mm) were added analytically to the raw data by calculating the intersection length. The attenuation value was chosen to match the attenuation values of the markers in the patient scans in the next section. The position of the markers were first defined in the volume. With known deformation vector fields, their position is known for all respiratory states and can be tracked on the detector using basic geometric considerations.

The simulation results are shown in Fig. 45. The depicted axial slices A to E have been selected to show areas in the outer motion range of the metal inserts. This is because these are the regions where the algorithms that account for motion differ from the ones that do not. In an average motion position, it is also possible to obtain good results with algorithms that do not account for motion. The position of the slices in the volume is shown in Fig. 43. Unlike indicated in the algorithm schemes, metal was not reinserted in the corrected volume in order to clearly distinguish remaining metal artifacts from reinserted metal. The first row shows the ground truth, i.e. the simulation without metal. In the second row, the simulation with metal is shown and the metal artifacts, that are indicated by red arrows, are visible. MAR1 was able to reduce metal artifacts but failed to remove them completely since it does not account for motion. MMAR, MMAR2, MoCoMAR1 and MoCoMAR2 were all able to remove the metal artifacts completely, as indicated by the green arrows. MMAR2 is a simplified version of the algorithm by Toftegaard et al. 2014 that knows the perfect metal mask in the raw data. Hence, the result is the best possible correction possible. The proposed algorithms MMAR and MoCoMAR1 were able to produce a nearly identical result. For

MoCoMAR2, an average respiratory motion state was chosen, so it is comparable to the 3D corrected volumes by the other algorithms. While the metal artifacts are removed, there are some small artificially smooth areas. This is a result of the interpolation that can be removed by using the frequency split in the FSNMAR algorithm (Meyer et al. 2012). Since the frequency split was not used for the other algorithms, it was not used here as well to allow for a fair comparison.

4.2.2 Patient Data

Like for the patient data for intrinsic gating, the kV CBCT unit from a Varian TrueBeam® system was used. The acquisition time was 60 s at 11 fps for all scans and 660 projections with an angular coverage of 360° were recorded. The size of the flat detector (1024×768 pixels with a pixel spacing of $(0.388\ \text{mm})^2$) and the parameters of the reconstructed volume (512×512×210 voxels with a voxel size of $(1\ \text{mm})^3$) are identical to Sec. 4.1 as well.

Three patient scans were available for evaluation. Patient 1 was scanned in the thorax region and has two implanted fiducial gold anchors. Patient 2 was scanned in the thorax region as well and has implanted cylindrical gold markers with an approximated length of 2 mm. For both patients, MMAR, MoCoMAR1, MoCoMAR2 and MAR1 were applied. The respiratory surrogate signal required for the MoCo was obtained using the newly developed intrinsic gating algorithm from the first part of the thesis. For Patient 1, the signal from the Varian RPM system was available. Patient 3 was scanned in the abdomen region, which is why it was not possible to utilize the acMoCo algorithm and therefore MoCoMAR1 and MoCoMAR2. It has two larger cylindrical gold markers with an approximated length of 10 mm and two smaller gold markers with an approximated length of 3 mm.

For patient 1, MAR1 was not able to remove the metal artifacts completely in contrast to MMAR, MoCoMAR1 and MoCoMAR2 that were able to obtain an artifact free volume (Fig. 46). For patient 2, MAR1 was able to remove the metal artifacts in the first slice, but failed for the others. The other algorithms were again able to remove the artifacts completely (Fig. 47). For the third patient, MAR1 was able to remove artifacts in slices D and E. These slices were further away from the diaphragm and therefore subjected to less motion. The other slices were closer to the diaphragm and MAR1 in turn failed to remove the artifacts. MMAR was able to remove them in all slices.

MoCoMAR2 sometimes introduced artificially smooth areas for all patients. As mentioned in the simulation section, this can be avoided by using the frequency split by Meyer et al. 2012. This was not done to allow for a fair comparison.

To illustrate the metal reinsertion step that was omitted in all previous results, Fig. 49 shows the results of MoCoMAR2 with and without reinserted metal. Metal reinsertion is only shown for MoCoMAR2, since for the other algorithms slices in the outer motion range were chosen. The reinserted metal does not show in these slices. For MoCoMAR2 a 4D volume is reconstructed. In the chosen respiratory state in Fig. 46-

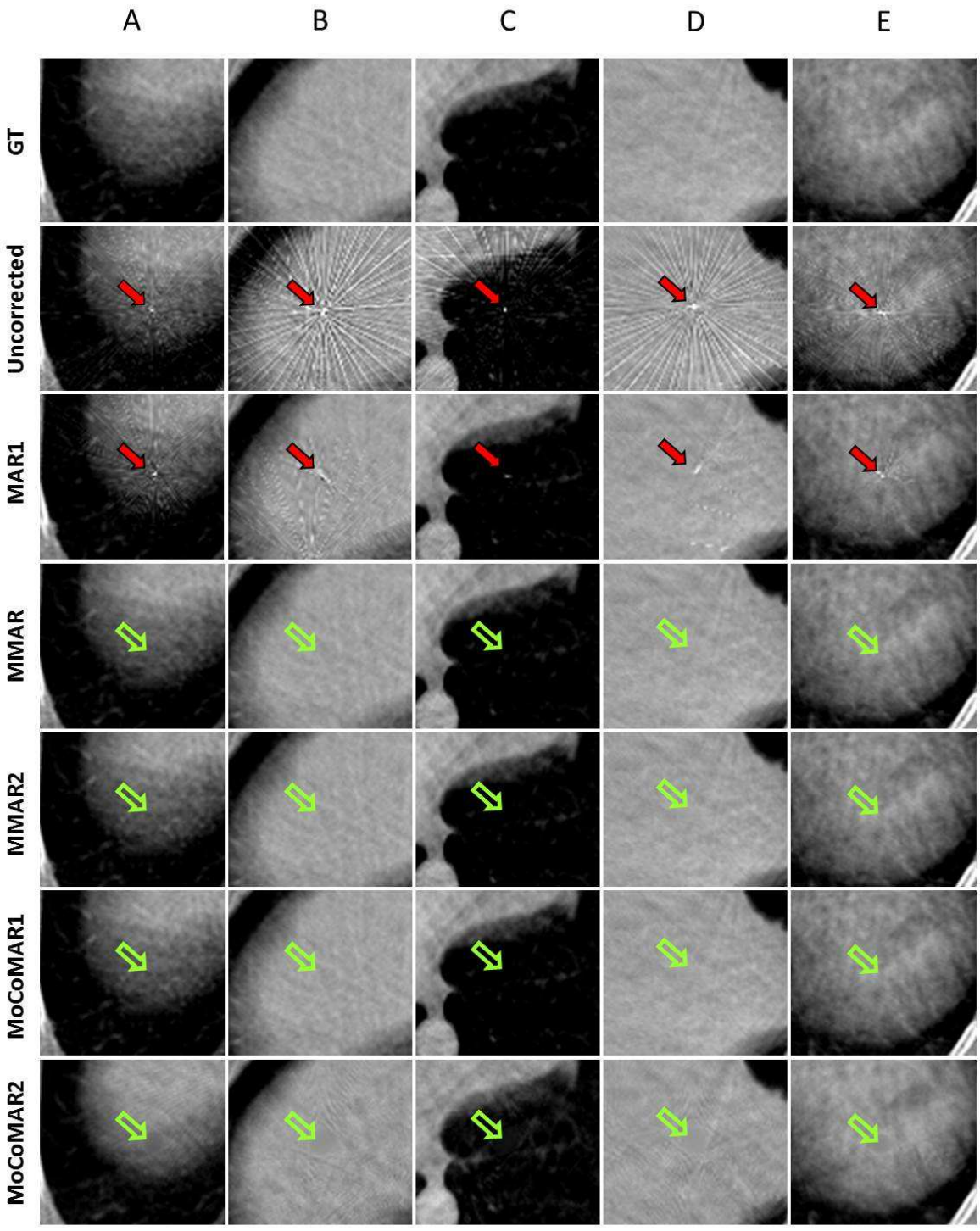

Figure 45.: Simulation results. Axial slices in the outer motion range of the metal inserts are chosen. The first and second row show the volume without and with the analytically added metal. The following rows show the results of the respective algorithms. Metal has not been reinserted to distinguish metal artifacts from the reinserted metal. The position of the metal implant is indicated by arrows. $C = 0$ HU, $W = 1500$ HU. Adopted from Hahn et al. 2018b.

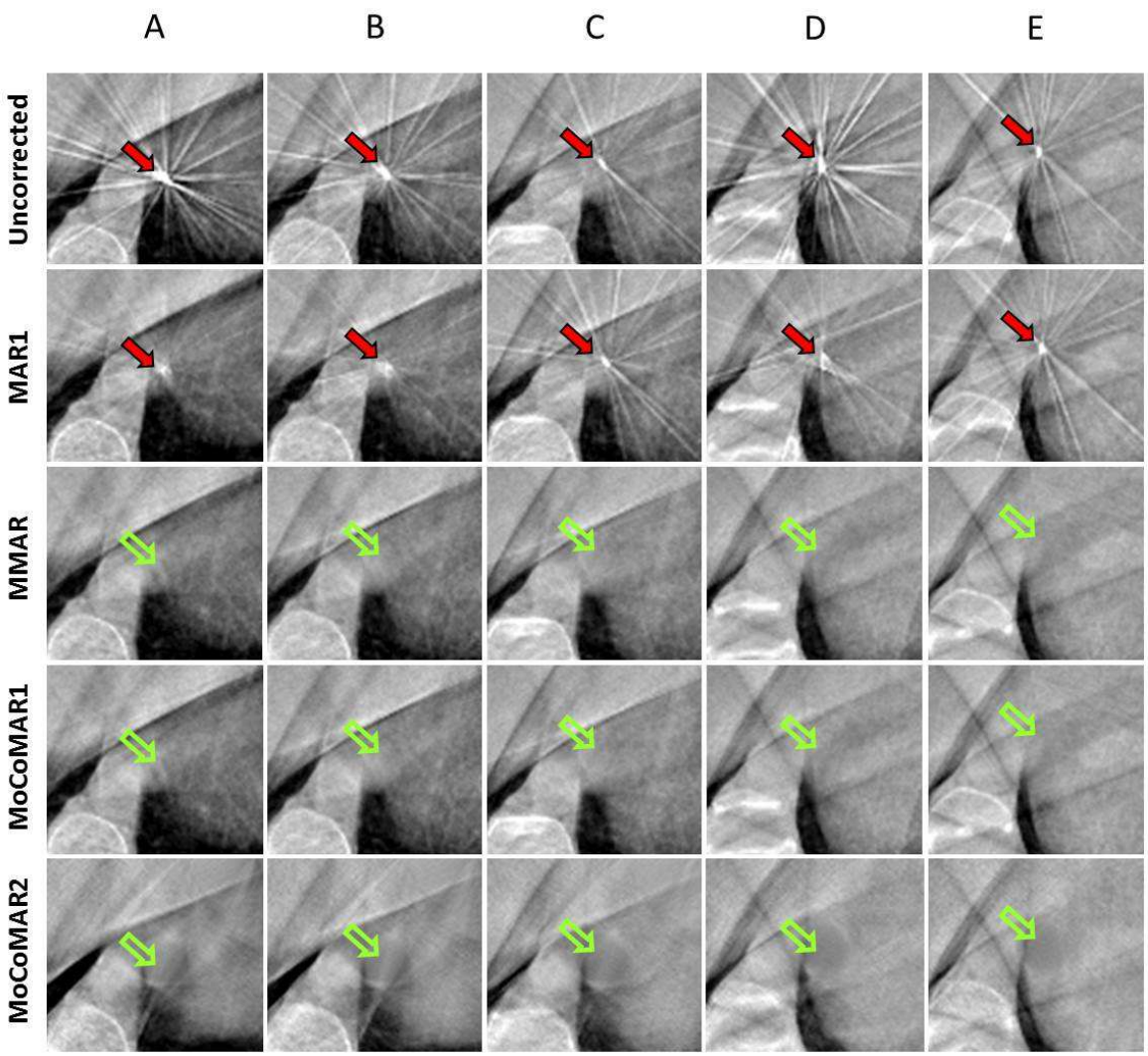

Figure 46.: Results of patient 1. For MoCoMAR2, the mid-inhale phase was selected to show a comparable volume. $C = 0$ HU, $W = 1500$ HU. Adopted from Hahn et al. 2018b.

48, metal is present in the selected slices, which is why the metal reinsertion is visible. Metal reinsertion is also shown in a sagittal view of the simulation. Artifact correction was done using the MMAR algorithm (Fig. 410).

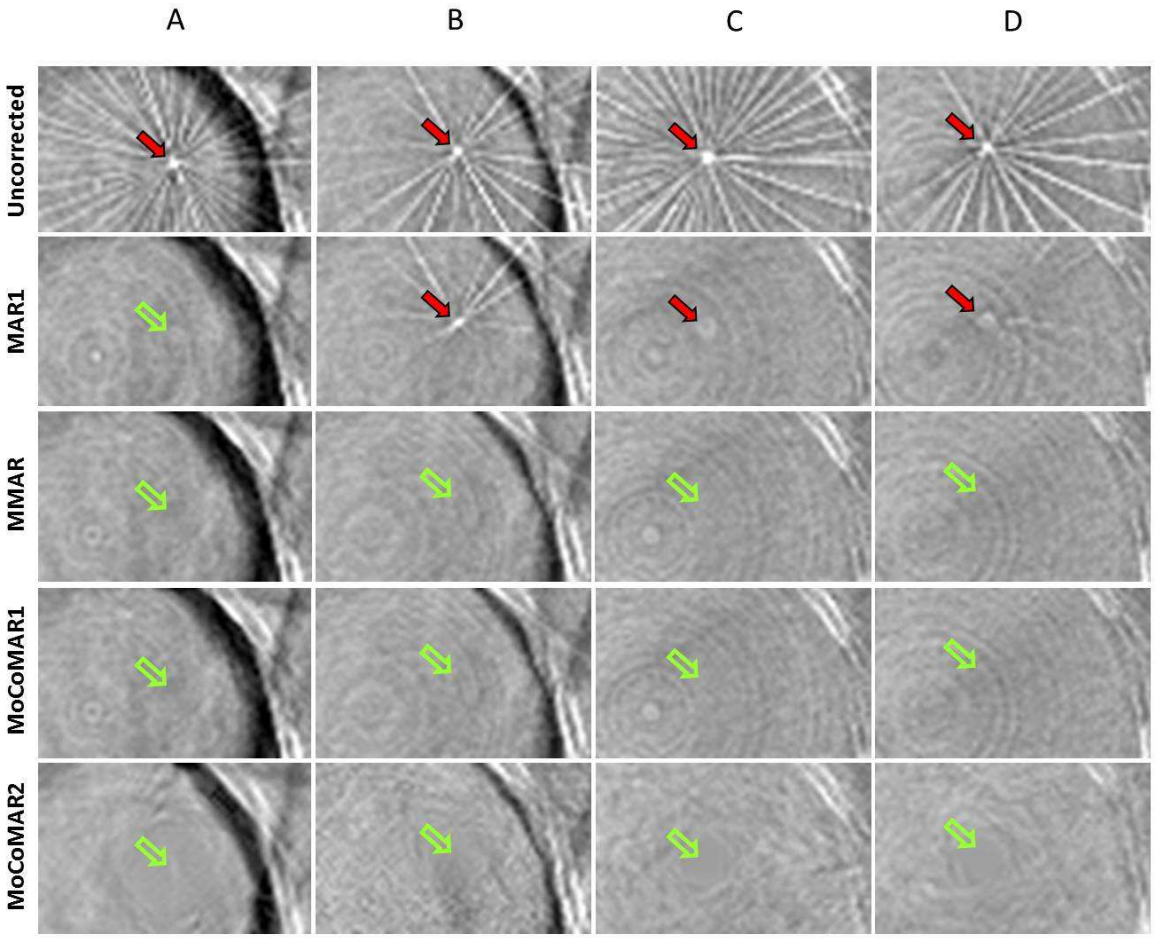

Figure 47.: Results of patient 2. For MoCoMAR2, the mid-inhale phase was selected to show a comparable volume. Ring artifacts can be seen in the selected slices because no ring suppression algorithm was enabled in the reconstructions. These artifacts vanish for the MoCoMAR2 result as a consequence of the acMoCo algorithm. $C = 0$ HU, $W = 1500$ HU. Adopted from Hahn et al. 2018b.

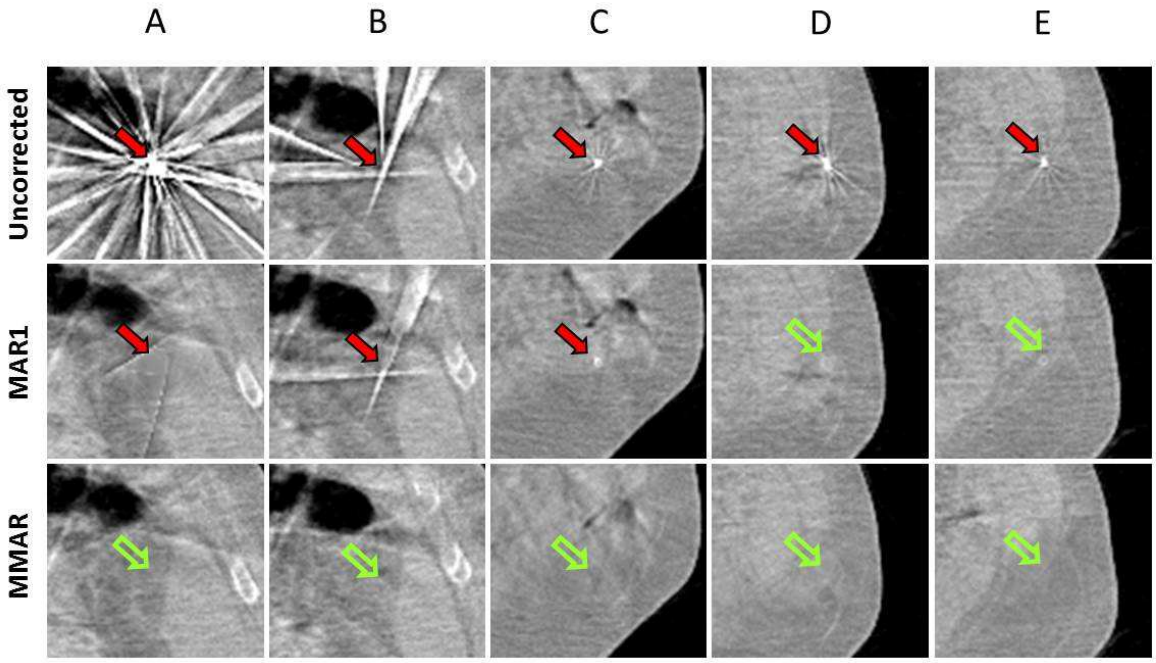

Figure 48.: Results of patient 3. For MoCoMAR2, the mid-inhale phase was selected to show a comparable volume. $C = 0$ HU, $W = 1500$ HU. Adopted from Hahn et al. 2018b.

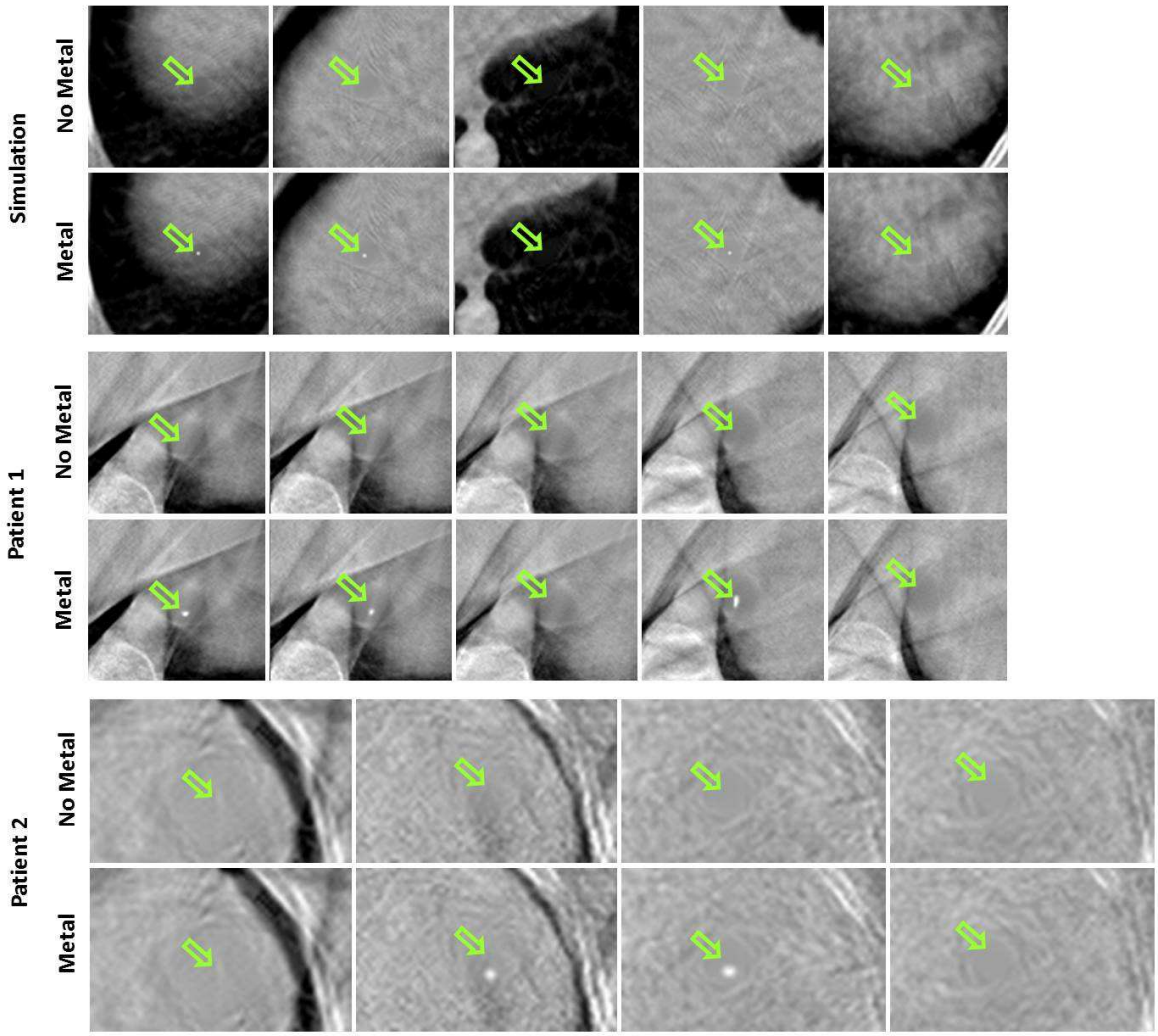

Figure 49.: To demonstrate the reinsertion of the metal, all results of the MoCoMAR2 algorithm are shown with and without reinserted metal. $C = 0$ HU, $W = 1500$ HU.

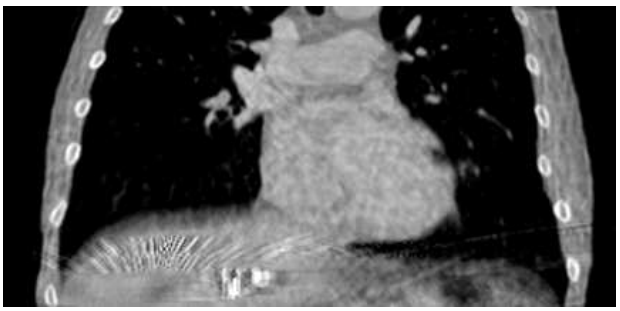

(a) Sagittal view of the uncorrected volume (simulation).

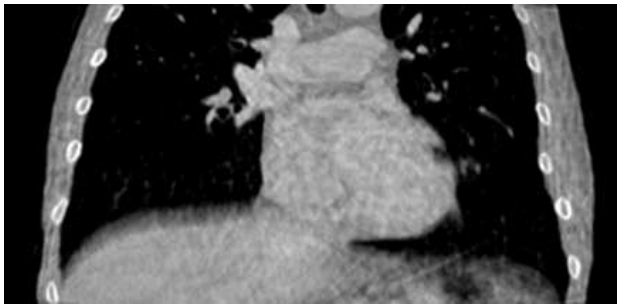

(b) Artifact free volume after metal removal using MMAR

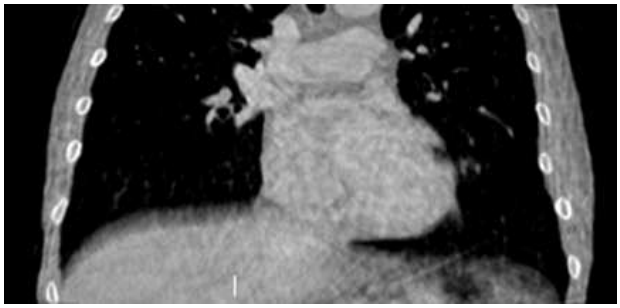

(c) Final volume with reinserted metal

Figure 410.: Illustration of metal reinsertion on the simulation data. (a) shows the sagittal view of the uncorrected volume. In (b), metal has been removed using MMAR. The final volume with the reinserted metal is shown in (c). $C = 0$ HU, $W = 1500$ HU. Adopted from Hahn et al. 2018b

5. Discussion

5.1 INTRINSIC GATING

Long acquisition times of up to one minute for cone-beam CT scans used in image-guided radiation therapy lead to motion blurring in the reconstructed volume and impede metal artifact removal using conventional algorithms in scans with metal inserts. In order to utilize motion compensation algorithms, a respiratory motion signal has to be available for all projection angles. This signal can then be used to link each projection to its corresponding respiratory motion state. The algorithm developed in the first part of the thesis aims to retrospectively extract a suitable motion surrogate from the projections. It does so in a fully automatic way and can be used for amplitude gating as well as phase gating. Additionally, it has to able to extract said signal for scans with and without a laterally shifted detector. Conventional algorithms for intrinsic are not designed to deal with a shifted detector. The novel algorithm utilizes a new scheme, where from a large group of potential motion surrogates, that are defined by grid points that are spread in the volume, the best candidate is chosen automatically. The efficacy of the method was evaluated using patient data acquired with the kV CBCT unit of a Varian TrueBeam™ and compared to the widely used Amsterdam-Shroud (AS) method (Zijp, Sonke, and Herk 2004). The novel algorithm can be used to extract a cardiac signal intrinsically as well using only small modifications from its original form: By swapping the grid points for circles that are defined within an axial plane, the cardiac can be acquired in a similar fashion. The cardiac gating was evaluated using the same patients and compared against a method for cardiac gating for small animals (Kuntz et al. 2010), since no other such algorithm exists for humans. In order to evaluate two key features of the algorithm, it was also compared to a version of itself without a preprocession step that subtracts a static background from the raw data and to a version of itself that uses the grid points for cardiac gating.

It was found that the proposed algorithm was able to reliably find a respiratory motion surrogate for all patients while the reference AS method failed for three patients. This can be caused by the nature of the AS algorithm. It compresses each projection into a single column and uses edge-detection in superior-inferior direction to track the diaphragm. The scans where the method failed had higher levels of noise. Since the proposed algorithm uses the average gray value within an ROI to constitute a motion surrogate, it less prone to noise than a method using edge detection. For the seven patients where both methods acquired a signal, the proposed algorithm was more ac-

curate for all patients but one.

For the evaluation of the respiratory gating, it was assumed that there can be a constant offset between intrinsic signal and an external signal. This assumptions is in contrast to a study by Ge et al. 2013. It states that the relation between an external and an intrinsic signal may change over time. Due to the relatively short scan times of 60 s seconds, we assume that our assumption still holds.

The ground truth for respiratory signal was acquired by manual inspection or by using the RPM, if it was available. Even though both methods provide a respiratory signal, it is not clear a priori if the peaks are at the same position. Therefore, as a proof of concept, the respiratory peaks were also determined manually for the scans where the RPM signal is available. It was found that the average deviation in the peak position is 0.21 s. For the scans at 11 fps, the time between two consecutive projections is $\approx$ 0.09 s, for scans at 11 fps it is $\approx$ 0.07 s. This corresponds to an accuracy of 2.3 projections or 3 projections, respectively and is a source of error.

For the cardiac gating, it was found that the proposed algorithm was able to obtain the correct number of heart beats with a maximum error of 1 heart beat for two patients. Since the ground truth for the number of heart beats was found by carefully inspecting the sinograms, the result lies within the error margin of the ground truth. Omitting the preprocession step lead to slightly worse results with a total absolute error of seven for all patients compared to a total error of two. Tracking the tangents of circles instead of grid points was found to improve the robustness of the algorithm a lot. For three patients a completely wrong number of heart beats was found when using grid points. For four patients the result could be improved using circles. For three patients the result was the same. The proposed algorithm outperformed the intrinsic cardiac gating for small animals for all patients. This can be attributed to the fact that the small animal gating uses an ROI that covers the complete heart, whereas the proposed algorithm uses a smaller ROI that only covers the ventricular wall. This smaller ROI leads to more precise results. Also, the algorithm for small animals involved a manual selection of the ROI that can be prone to errors. However, other ROI positions were tested and no significant changes were noticed.

The proposed algorithm depends on several parameters: The size of the ROI, the number of grid points and the band-pass filter. As a long as reasonable parameters are chosen, it was found that the algorithm does not depend very much on the exact parameters. The ROI for respiratory gating should be large enough to cover the whole motion of the diaphragm, the ROI for cardiac gating should be much smaller, since it only needs to cover the ventricular wall. For respiratory gating a small number of grid points is sufficient, while the number of grid points for the cardiac gating has to be high enough to allow for sufficient coverage of the volume.

While the initial motivation for the design of this algorithm was to supplement the moving metal artifact reduction methods, it is not limited to this application. The signal from the respiratory intrinsic gating can be used by all algorithms that sort projections into motion bins to acquire 4D-CBCT images (**leng:08**; Sonke et al. 2005; Kriminski et al. 2005; Li et al. 2006; Dietrich et al. 2006; Purdie et al. 2006; Lu et al. 2007; Guckenberger et al. 2008; Sonke et al. 2009; Bergner et al. 2010; Jia et al. 2012) or algorithms that correct the motion during reconstruction or post-processing (Schäfer et al. 2004; Li et al. 2005; Isola et al. 2008; Rit et al. 2009; Zhang et al. 2010; Lewis et al. 2011; Brehm et al. 2012; Brehm et al. 2013; Sauppe et al. 2016b). A potential additional field of application that would use the respiratory and the cardiac gating is small animal CT. While there are no conceptual problems with the proposed algorithm that would be prevent its use in small animal CT, this has not been tested within the scope of this thesis and can be the field of future investigations. Another application is in the field of interventional imaging with C-arm systems. The proposed algorithm was already used for a novel 5D motion compensation approach by Sauppe et al. 2016b, that allows for cardiac and respiratory motion compensation for radiation therapy of tumors close to the heart.

An argument can be made that a reliable algorithm for intrinsic gating is to be preferred to external motion surrogates, e.g. acquired using markers for abdominal surface tracking (Ford et al. 2002; Vedam et al. 2002; Pan et al. 2004), measuring pressure changes of a respiratory belt (Dietrich et al. 2006; Kleshneva, Muzik, and Alber 2006) or by using spirometry (Low et al. 2003; Zhang et al. 2003). Intrinsic gating approaches directly measure the motion of the internal structures in contrast to the external methods. Studies found, that the correlation between the external signal and the anatomic motion may not always be as clear as desired (Ahn et al. 2004; Hoisak et al. 2004; Tsunashima et al. 2004; Gierga et al. 2005; Yan et al. 2006).

5.2 MOVING METAL ARTIFACT REDUCTION

Highly attenuating objects such as metal inserts lead to artifacts that effect the image quality negatively. While conventional algorithms for metal artifact reduction focus on static metal, moving metal, e.g. fiducial gold cylinders used for tumor tracking, occur in CBCT scans used for image-guided radiation therapy due to the long acquisition times of up to 60 s. Two new algorithms were developed that aim to remove artifacts caused by metal of arbitrary shape that is subjected to motion. The goal of the new methods is to remove artifacts caused by moving metal inserts without introducing new artifacts and without any prior knowledge, e.g. the shape or material of the metal, in a fully automatic fashion. They shall work as well for metal that is not subjected to motion. The first algorithm uses the acMoCo (Brehm et al. 2013) algorithm in order to determine the position of the metal in the volume for all different respiratory

motion states and is called MoCoMAR1. This information is used to remove moving metal inserts in the original raw data using the NMAR algorithm (Meyer et al. 2010) to obtain an metal artifact free 3D volume. The second algorithm (MoCoMAR2) uses the acMoCo and the NMAR algorithms sequentially to obtain a 4D volume without motion and metal artifacts. The intrinsic gating from the first half of the thesis was used to obtain a respiratory motion surrogate that is needed by the acMoCo algorithm. Additionally, the MMAR algorithm by Brehm et al. 2011 was expanded by introducing a segmentation step in the volume to segment blurred metal as well. All algorithms were tested on simulated data, where realistic deformation vector fields were applied to a clinical CT volume to simulate breathing and fiducial gold cylinders of different sizes were added analytically to the raw data. They were tested on patient data as well and compared to a standard method for metal artifact reduction MAR1 by Kalender, Hebel, and Ebersberger 1987. The method by Toftegaard et al. 2014 was not available. It uses a 3D marker model to estimate the marker position in the raw data and was tested for the case of an ideal mask in the raw data on the simulation.

MoCoMAR1, MoCoMAR2 and MMAR were able to remove all metal artifacts in the simulated data. While MoCoMAR1 and MMAR did not introduce new artifacts, MoCoMAR2 introduced small artificially smooth areas around the position of the metal insert. These areas can potentially be removed using the frequency split by Meyer et al. 2012. This was, however, not done since MAR1 did not use a frequency split and thus a fair comparison would not be possible. MAR1 was able to reduce the metal artifacts but did not remove them completely. Compared to the method by Toftegaard et al. 2014 in the case of an ideal raw data metal mask, no difference to the results by MMAR and MoCoMAR was found.

For the patient data, MMAR, MoCoMAR1 and MoCoMAR2 were able to remove all metal artifacts. MAR1 was not able to remove all artifacts. It removed the artifacts in cases of metal with a small motion range, i.e. fiducial markers that are not in the proximity of the diaphragm. In cases of stronger marker motion, it reduced the artifacts but failed to remove them.

Since MMAR and MoCoMAR1 produced nearly identical results, MMAR is to be preferred due to its lower computation time which is in the same order as that of classical inpainting methods such as MAR1 or NMAR. It could therefore be clinically applicable. Additionally, unlike MoCoMAR1 and MoCoMAR2 it does not require a motion signal. One could argue that MoCoMAR1 has the potential to be more robust when it comes to the metal segmentation in the volume compared to MMAR, since the to be segmented markers are sharper and not smeared. However, no case was found in the evaluation where MoCoMAR1 removed artifacts that MMAR could not remove. MoCoMAR2 is to be used in cases where a 4D volume is desired. Unlike MMAR and MoCoMAR1, where the originally segmented markers are reinserted in a final step, MoCoMAR2 has the potential to improve marker size and position estimation since

they are segmented in a 4D volume. This was, however, not evaluated here and can be the subject of future studies.

6. Conclusions

The goal of this thesis was the development of algorithms for the reduction of artifacts caused by moving metal artifacts in CBCT scans of thorax region. The proposed methods connect the fields of motion compensation and metal artifact reduction, which were regarded independently before. As a prerequisite for the motion compensation, an algorithm was developed that aims to extract a respiratory and cardiac motion surrogate from the raw data.

The proposed algorithm for intrinsic gating was necessary since conventional algorithms are not designed for laterally shifted detectors, that are commonly used in IGRT with a CBCT to increase the field of view. In a novel approach, grid points are distributed over the volume and tracked on the detector, each resulting in a possible respiratory motion surrogate. From these candidates, the best signal is determined automatically. Tests using patient data showed that the proposed method was able to reliably determine a suitable motion surrogate for all patients in contrast to a widely used conventional method. It was found that the same principle can be used for cardiac gating as well, if instead of the grid points being tracked on the detector, tangents to circles are being tracked. The method was able to determine the correct number of heart beats with a maximum error of one heart beat in 60 s scans of patients. A preprocession step, that removes a static background from the raw data, was found to result in a small improvement of the result. The switch from grid points to circles was found to be more impactful, as without it strong deviations of more than ten heart beats were found for some patients. Due to the lack of another intrisic gating algrithm for humans, it was compared to an algorithm for small animal intrinsic cardiac gating. The proposed method outperformed the small animal method for all patients.

In the field of moving metal artifact reduction, two novel algorithms were developed. The first one is called MoCoMAR1 and uses a motion compensation algorithm by Brehm et al. 2013 to segment otherwise blurred metal in a 4D volume. From this, a metal mask in the original raw data is created that accounts for metal motion. Using an inpainting approach, an artifact free 3D volume is reconstructed. The second algorithm, MoCoMAR2, uses the same motion compensation algorithm to obtain a 4D volume. News 4D raw data are generated using forward projection and the normalized metal artifact reduction by Meyer et al. 2010 is utilizes to obtain a 4D volume without motion and metal artifacts. For an already existing method called MMAR by Brehm et al. 2011, that does not require motion compensation, an advanced segmentation in the volume was created to account for metal inserts with lower attenuation values due

to blurring caused by respiratory motion. All algorithms were tested on simulated data and on patient data and successfully removed all metal artifacts and therefore greatly improved the image quality. They were compared to a conventional method that does not account for motion, which was able to remove the artifacts only in cases with small motion. No significant differences in the results of MoCoMAR1, MoCoMAR2 and MMAR were found, which is why the MMAR algorithm is to be prefered due to its low computational time, that is comparable to conventional inpainting based MAR methods. MoCoMAR2 is to be used if an artifact free 4D volume is desired.

Appendices

A. Band-pass Filter

As a band-pass filter, a finite impulse response (FIR) filter was used. The advantage of FIR filters is that they are stable, since a finite impulse response is guaranteed. Additionally, they can easily be implemented as a filter with linear phase by using a symmetric coefficient sequence. Hence, there is no phase distortion since all frequency components of the input signal are shifted equally in time. Let $x(n)$ be the input signal and $y(n)$ the output signal after filtering. Then $y(n)$ is given by

$$y(n) = \sum_{k=0}^{N-1} h(k)x(n-k) = (h * x)(n). \tag{A1}$$

$h(k)$ are called filter taps, N is the number of taps. $h(k)$ is also the impulse response function of the filter. The filter is defined by the frequencies it allows to pass, which is why one has to consider the frequency response $H(\omega)$ of the taps $h(k)$. It is given by the discrete-time Fourier transform (DTFT) of the impulse response:

$$H(\omega) = \sum_{k=0}^{N-1} h(n)e^{-i\omega n}, \; \omega = \frac{2\pi f}{f_s} \tag{A2}$$

ω is defined relative to the sampling frequency f_s. An ideal bandpass filter that allows frequencies between $[\omega_l, \omega_h]$ is given by

$$H(\omega) = \begin{cases} 1, & \omega_l \leq \omega \leq \omega_h \;\vee\; -\omega_h \leq \omega \leq -\omega_l \\ 0, & \text{else} \end{cases} \tag{A3}$$

An example is illustrated in Fig. A1. The taps can in turn be calculated by using the inverse DTFT:

$$h(k) = \frac{1}{2\pi} \int_{-\pi}^{\pi} H(\omega)e^{i\omega k} \mathrm{d}\omega \tag{A4}$$

For the ideal filter in Eq. A3, the taps $h(k)$ can easily be calculated.

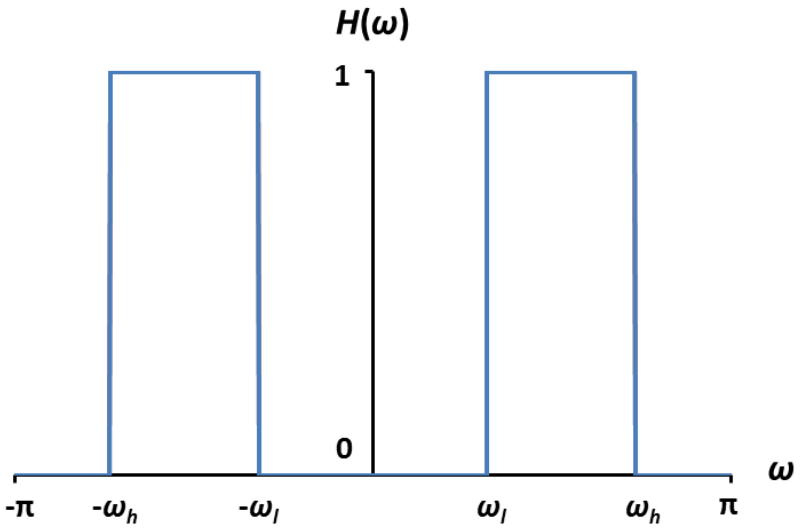

Figure A1.: Frequency response $H(\omega)$ of an ideal bandpass filter that passes frequencies between ω_l and ω_h. Since $H(\omega)$ is periodic in ω with a periodicity of 2π, it only needs to be specified over the Nyquist interval $[-\pi, \pi]$ (Orfanidis 1995).

$$\begin{aligned} h(k) &= \frac{1}{2\pi}\left(\int_{-\omega_h}^{\omega_l} e^{i\omega k}\mathrm{d}\omega + \int_{\omega_l}^{\omega_h} e^{i\omega k}\mathrm{d}\omega\right) \\ &= \frac{1}{k\pi}\frac{e^{-i\omega_l k} - e^{-i\omega_h k} + e^{i\omega_h k} - e^{i\omega_l k}}{2i} \\ &= \frac{\sin(\omega_h k) - \sin(\omega_l k)}{k\pi} \end{aligned} \tag{A5}$$

For $k \to 0$, the tap $h(0)$ is given by

$$h(0) = \frac{\omega_h}{\pi} - \frac{\omega_l}{\pi}. \tag{A6}$$

The bandpass filter used in the context of intrinsic gating had 51 taps and allowed for frequencies of 10–30 rpm for respiratory gating and 50–120 bpm for cardiac gating. The respective frequency response functions are shown in Fig. A2+A3. Note, that the gain does not instantly drop to zero outside of the desired frequency band, which is indicated by the vertical dashed red lines. Also, ripples occur due to Gibbs phenomenon (Hewitt and Hewitt 1979).

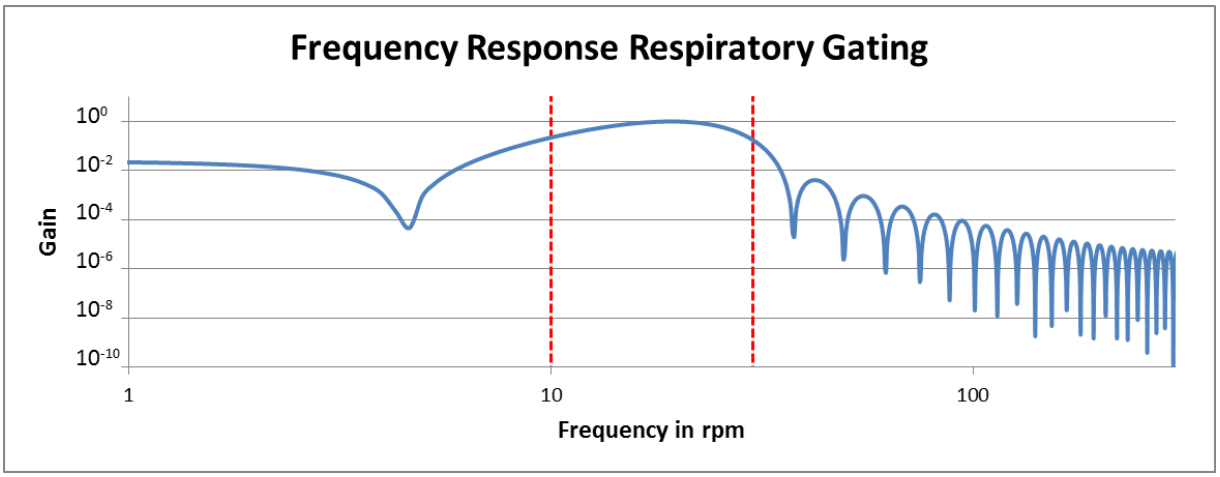

Figure A2.: Frequency response respiratory gating. The dashed red lines indicate the cut-off frequencies at 10 rpm and 30 rpm.

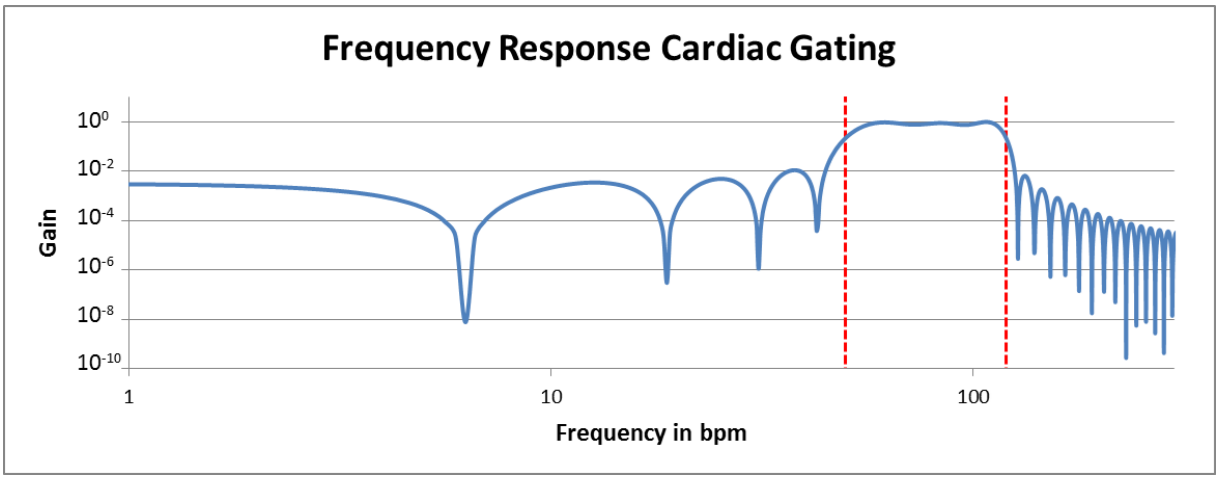

Figure A3.: Frequency response cardiac gating. The dashed red lines indicate the cut-off frequencies at 50 bpm and 120 bpm.

Bibliography

Ahn, S, B Yi, Y Suh, J Kim, S Lee, S Shin, S Shin, and E Choi (2004). "A Feasibility Study on the Prediction of Tumour Location in the Lung from Skin Motion". In: *The British journal of radiology* 77.919, pp. 588–596.

Ahnesjö, A. and M. M. Aspradakis (1999). "Dose calculations for external photon beams in radiotherapy". In: *Physics in Medicine & Biology* 44.11, R99.

Bal, M. and L. Spies (2006). "Metal Artifact Reduction in CT using Tissue-Class Modeling and Adaptive Prefiltering". In: *Med. Phys.* 33.8, pp. 2852–2859.

Bal, M., H. Celik, K. Subramanyan, K. Eck, and L. Spies (2005). "A Radial Adaptive Filter for Metal Artifact Reduction". In: *Medical Imaging 2005: Image Processing*. Vol. 5747. International Society for Optics and Photonics, pp. 2075–2083.

Bartling, S. H., J. Dinkel, W. Stiller, M. Grasruck, I. Madisch, H.-U. Kauczor, W. Semmler, R. Gupta, and F. Kiessling (July 2008). "Intrinsic Respiratory Gating in Small–Animal CT". In: *European Radiology* 18.7, pp. 1375–1384.

Bergner, F., T. Berkus, M. Oelhafen, P. Kunz, T. Pan, and M. Kachelrieß (2009). "Autoadaptive Phase-Correlated (AAPC) Reconstruction for 4D CBCT". In: *Med. Phys.* 36.12, pp. 5695–5706.

Bergner, F., T. Berkus, M. Oelhafen, P. Kunz, T. Pan, R. Grimmer, L. Ritschl, and M. Kachelrieß (2010). "An Investigation of 4D Cone-Beam CT Algorithms for Slowly Rotating Scanners". In: *Med. Phys.* 37.9, pp. 5044–5053.

Bert, C., K. G. Metheany, K. Doppke, and G. T. Chen (2005). "A Phantom Evaluation of a Stereo-Vision Surface Imaging System for Radiotherapy Patient Setup". In: *Med. Phys.* 32.9, pp. 2753–2762.

Bert, C., K. G. Metheany, K. P. Doppke, A. G. Taghian, S. N. Powell, and G. T. Chen (2006). "Clinical Experience with a 3D Surface Patient Setup System for Alignment of Partial-Breast Irradiation Patients". In: *International Journal of Radiation Oncology* Biology* Physics* 64.4, pp. 1265–1274.

Bethe, H. and W. Heitler (1934). "On the Stopping of fast Particles and on the Creation of Positive Electrons". In: *Proceedings of the Royal Society of London. Series A, Containing Papers of a Mathematical and Physical Character* 146.856, pp. 83–112.

Bhatia, N., D. Tisseur, F. Buyens, and J. M. Létang (2016). "Scattering Correction using Continuously Thickness-Adapted Kernels". In: *NDT & E International* 78, pp. 52–60.

Bianchi, W., A. F. Dugas, Y.-H. Hsieh, M. Saheed, P. Hill, C. Lindauer, A. Terzis, and R. E. Rothman (2013). "Revitalizing a Vital Sign: Improving Detection of Tachypnea at Primary Triage". In: *Annals of emergency medicine* 61.1, pp. 37–43.

Biguri, A., M. Dosanjh, S. Hancock, and M. Soleimani (2017). "A General Method for Motion Compensation in X-Ray Computed Tomography". In: *Physics in Medicine & Biology* 62.16, p. 6532.

Bouguer, P. (1729). *Essai d'Optique sur la Gradation de la Lumière*.

Brehm, M., T. Berkus, T. Oelhafen, and M. Kachelrieß (2011). "Moving metal artifact reduction (MMAR): A metal artifact reduction algorithm for flat detector cone-beam CT scans with metal subject to respiratory motion". In: *RSNA Conference Proc.*

Brehm, M., P. Paysan, M. Oelhafen, P. Kunz, and M. Kachelrieß (2012). "Self-Adapting Cyclic Registration for Motion-Compensated Cone-Beam CT in Image-Guided Radiation Therapy". In: *Med. Phys.* 39.12, pp. 7603–7618.

Brehm, M., P. Paysan, M. Oelhafen, and M. Kachelrieß (2013). "Artifact-Resistant Motion Estimation with a Patient-Specific Artifact Model for Motion-Compensated Cone-Beam CT". In: *Med. Phys.* 40.10, p. 101913.

Brehm, M., S. Sawall, J. Maier, S. Sauppe, and M. Kachelrieß (2015). "Cardiorespiratory Motion-Compensated Micro-CT Image Reconstruction using an Artifact Model-Based Motion Estimation". In: *Med. Phys.* 42.4, pp. 1948–1958.

Brooks, R. A. (1977). "A Quantitative Theory of the Hounsfield Unit and its Application to Dual Energy Scanning." In: *Journal of computer assisted tomography* 1.4, pp. 487–493.

Compton, A. H. (1923). "A quantum theory of the scattering of X-rays by light elements". In: *Physical review* 21.5, p. 483.

Dang, J., X. Gu, T. Pan, and J. Wang (2015). "A Pilot Evaluation of a 4-Dimensional Cone-Beam Computed Tomographic Scheme Based on Simultaneous Motion Estimation and Image Reconstruction". In: *International Journal of Radiation Oncology* Biology* Physics* 91.2, pp. 410–418.

Dawson, L. A. and D. A. Jaffray (2007). "Advances in Image-Guided Radiation Therapy". In: *Journal of clinical oncology* 25.8, pp. 938–946.

De Man, B., J. Nuyts, P. Dupont, G. Marchal, and P. Suetens (2001). "An Iterative Maximum-Likelihood Polychromatic Algorithm for CT". In: *IEEE transactions on medical imaging* 20.10, pp. 999–1008.

Dhou, S., Y. Motai, and G. D. Hugo (2013). "Local Intensity Feature Tracking and Motion Modeling for Respiratory Signal Extraction in Cone Beam CT Projections". In: *IEEE Trans. Biomed. Engineering* 60.2, pp. 332–342.

Dietrich, L., S. Jetter, T. Tücking, S. Nill, and U. Oelfke (2006). "Linac-Integrated 4D Cone Beam CT: First Experimental Results". In: *Physics in Medicine & Biology* 51.11, p. 2939.

Ding, G. X. and P. Munro (2013). "Radiation Exposure to Patients from Image Guidance Procedures and Techniques to Reduce the Imaging Dose". In: *Radiotherapy and Oncology* 108.1, pp. 91–98.

Dinkel, J., S. H. Bartling, J. Kuntz, M. Grasruck, A. Kopp-Schneider, M. Iwasaki, S. Dimmeler, R. Gupta, W. Semmler, H.-U. Kauczor, and F. Kiessling (2008). "Intrinsic Gating for Small–Animal Computed Tomography: A Robust ECG–Less Paradigm for Deriving Cardiac Phase Information and Functional Imaging". In: *Circulation: Cardiovascular Imaging* 1.3, pp. 235–243.

Einstein, A. (1905). "Über einen die Erzeugung und Verwandlung des Lichtes betreffenden heuristischen Gesichtspunkt". In: *Annalen der Physik* 322.6, pp. 132–148.

Farncombe, T. (2008). "Software–Based Respiratory Gating for Small Animal Conebeam CT". In: *Med. Phys.* 35.5, pp. 1785–1792.

Feldkamp, L. A., L. Davis, and J. W. Kress (1984). "Practical Cone-Beam Algorithm". In: *Journal of the Optical Society of America* 1.6, pp. 612–619.

Ford, E., G. Mageras, E Yorke, K. Rosenzweig, R Wagman, and C. Ling (2002). "Evaluation of Respiratory Movement During Gated Radiotherapy using Film and Electronic Portal Imaging". In: *International Journal of Radiation Oncology* Biology* Physics* 52.2, pp. 522–531.

Ge, J., L. Santanam, D. Yang, and P. J. Parikh (2013). "Accuracy and Consistency of Respiratory Gating in Abdominal Cancer Patients". In: *International Journal of Radiation Oncology* Biology* Physics* 85.3, pp. 854–861.

George, R., T. D. Chung, S. S. Vedam, V. Ramakrishnan, R. Mohan, E. Weiss, and P. J. Keall (2006). "Audio-Visual Biofeedback for Respiratory-Gated Radiotherapy: Impact of Audio Instruction and Audio-Visual Biofeedback on Respiratory-Gated Radiotherapy". In: *International Journal of Radiation Oncology* Biology* Physics* 65.3, pp. 924–933.

Gierga, D. P., J. Brewer, G. C. Sharp, M. Betke, C. G. Willett, and G. T. Chen (2005). "The Correlation Between Internal and External Markers for Abdominal Tumors: Implications for Respiratory Gating". In: *International Journal of Radiation Oncology* Biology* Physics* 61.5, pp. 1551–1558.

Glover, G. H. and N. J. Pelc (1981). "An Algorithm for the Reduction of Metal Clip Artifacts in CT Reconstructions". In: *Med. Phys.* 8.6, pp. 799–807.

Glover, G. and N. Pelc (1980). "Nonlinear partial volume artifacts in x-ray computed tomography". In: *Med. Phys.* 7.3, pp. 238–248.

Grimmer, R., R. Fahrig, W. Hinshaw, H. Gao, and M. Kachelrieß (2012). "Correction for Beam Hardening in CT". In: *Med. Phys.* 39.2, pp. 825–831.

Guckenberger, M., R. A. Sweeney, J. Wilbert, T. Krieger, A. Richter, K. Baier, G. Mueller, O. Sauer, and M. Flentje (2008). "Image-Guided Radiotherapy for Liver Cancer Using Respiratory-Correlated Computed Tomography and Cone-Beam Computed Tomography". In: *International Journal of Radiation Oncology* Biology* Physics* 71.1, pp. 297–304.

Gupta, T and C. A. Narayan (2012). "Image-Guided Radiation Therapy: Physician's Perspectives". In: *Journal of medical physics/Association of Medical Physicists of India* 37.4, p. 174.

Hahn, A. and M. Kachelrieß (May 2018). "Fully Automatic Intrinsic Respiratory and Cardiac Gating of Cone-Beam CT Scans of the Thorax Region". In: *The Fifth International Conference on Image Formation in X-Ray Computed Tomography, Proceedings*.

Hahn, A., M. Knaup, and M. Kachelrieß (Nov. 2018). "A Robust Fully Automatic Method for Intrinsic Respiratory and Cardiac Gating for Cone-Beam CT Scans of the Thorax Region". In: *104th Scientific Assembly and Annual Meeting of the Radiological Society of North America (RSNA), Proceedings*.

Hahn, A., S. Sauppe, and M. Kachelrieß (2016). "Automatic Intrinsic Cardiac and Respiratory Gating from Cone-Beam CT Scans of the Thorax Region". In: *Proceedings 2016 SPIE Medical Imaging Conference*.

Hahn, A., S. Sauppe, M. Knaup, and M. Kachelrieß (Feb. 2018a). "Moving Metal Artifact Reduction for Cone-Beam CT (CBCT) Scans of the Thorax Region". In: *Insights into Imaging, ECR Book of Abstracts*.

Hahn, A., M. Knaup, M. Brehm, S. Sauppe, and M. Kachelrieß (2018b). "Two Methods for Reducing Moving Metal Artifacts in Cone-Beam CT". In: *Med. Phys.* 45.8, pp. 3671–3680.

Hahn, A., M. Knaup, C. Bert, and M. Kachelrieß (2019). "Fully Automatic Intrinsic Respiratory and Cardiac Gating for Cone-Beam CT Scans of the Thorax Region". Manuscript submitted for publication.

Hertz, H. (1887). "Ueber einen Einfluss des ultravioletten Lichtes auf die electrische Entladung". In: *Annalen der Physik* 267.8, pp. 983–1000.

Hewitt, E. and R. E. Hewitt (1979). "The Gibbs-Wilbraham Phenomenon: An Episode in Fourier Analysis". In: *Archive for history of Exact Sciences* 21.2, pp. 129–160.

Hoisak, J. D., K. E. Sixel, R. Tirona, P. C. Cheung, and J.-P. Pignol (2004). "Correlation of lung tumor motion with external surrogate indicators of respiration". In: *International Journal of Radiation Oncology* Biology* Physics* 60.4, pp. 1298–1306.

Hu, J., S. T. Haworth, R. C. Molthen, and C. A. Dawson (2004). "Dynamic Small Animal Lung Imaging via a Postacquisition Respiratory Gating Technique using Micro-Cone Beam Computed Tomography". In: *Academic Radiology* 11.9, pp. 961–970.

Ionascu, D., S. B. Jiang, S. Nishioka, H. Shirato, and R. I. Berbeco (2007). "Internal-External Correlation Investigations of Respiratory Induced Motion of Lung Tumors". In: *Med. Phys.* 34.10, pp. 3893–3903.

Isola, A., A. Ziegler, T Koehler, W. Niessen, and M. Grass (2008). "Motion-Compensated Iterative Cone-Beam CT Image Reconstruction with Adapted Blobs as Basis Functions". In: *Physics in Medicine & Biology* 53.23, p. 6777.

Jeong, K. Y. and J. B. Ra (2009). "Reduction of Artifacts due to Multiple Metallic Objects in Computed Tomography". In: *Medical Imaging 2009: Physics of Medical Imaging*. Vol. 7258. International Society for Optics and Photonics, 72583E.

Jia, X., Z. Tian, Y. Lou, J.-J. Sonke, and S. B. Jiang (2012). "Four-Dimensional Cone Beam CT Reconstruction and Enhancement Using a Temporal Nonlocal Means Method". In: *Med. Phys.* 39.9, pp. 5592–5602.

Jiang, S. B. (2006). "Technical Aspects of Image-Guided Respiration-Gated Radiation Therapy". In: *Medical Dosimetry* 31.2, pp. 141–151.

Kachelrieß, M. and W. A. Kalender (1998). "Electrocardiogram–Correlated Image Reconstruction from Subsecond Spiral Computed Tomography Scans of the Heart". In: *Med. Phys.* 25.12, pp. 2417–2431.

Kachelrieß, M., K. Sourbelle, and W. A. Kalender (2006). "Empirical Cupping Correction: A First-Order Raw Data Precorrection for Cone-Beam Computed Tomography". In: *Med. Phys.* 33.5, pp. 1269–1274.

Kachelrieß, M., D.-A. Sennst, W. Maxlmoser, and W. A. Kalender (July 2002). "Kymogram Detection and Kymogram–Correlated Image Reconstruction from Subsecond Spiral Computed Tomography Scans of the Heart". In: *Med. Phys.* 29.7, pp. 1489–1503.

Kalender, W. A., R. Hebel, and J. Ebersberger (Aug. 1987). "Reduction of CT Artifacts Caused by Metallic Implants". In: *Radiology* 164.2, pp. 576–577.

Kavanagh, A., P. M. Evans, V. N. Hansen, and S. Webb (2009). "Obtaining Breathing Patterns from any Sequential Thoracic X-Ray Image Set". In: *Physics in Medicine & Biology* 54.16, p. 4879.

Keall, P. J., G. S. Mageras, J. M. Balter, R. S. Emery, K. M. Forster, S. B. Jiang, J. M. Kapatoes, D. A. Low, M. J. Murphy, B. R. Murray, et al. (2006). "The management of Respiratory Motion in Radiation Oncology Report of AAPM Task Group 76 a". In: *Med. Phys.* 33.10, pp. 3874–3900.

Kijewski, P. and B. .Bjarngard (1978). "Empirical Cupping Correction for CT Scanners with Primary Modulation (ECCP)". In: *Med. Phys.* 5.3, pp. 209–214.

Kini, V. R., S. S. Vedam, P. J. Keall, S. Patil, C. Chen, and R. Mohan (2003). "Patient Training in Respiratory-Gated Radiotherapy". In: *Medical Dosimetry* 28.1, pp. 7–11.

Kleshneva, T, J Muzik, and M Alber (2006). "An Algorithm for Automatic Determination of the Respiratory Phases in Four-Dimensional Computed Tomography". In: *Physics in Medicine & Biology* 51.16, N269.

Kory, R. C. (1957). "Routine Measurement of Respiratory Rate: An Expensive Tribute to Tradition". In: *Journal of the American Medical Association* 165.5, pp. 448–450.

Kratz, B., S. Ens, J. Müller, and T. M. Buzug (2011). "Reference-Free Ground Truth Metric for Metal Artifact Evaluation in CT Images". In: *Med. Phys.* 38.7, pp. 4321–4328.

Kriminski, S., M. Mitschke, S. Sorensen, N. M. Wink, P. E. Chow, S. Tenn, and T. D. Solberg (2005). "Respiratory Correlated Cone-Beam Computed Tomography on an Isocentric C-Arm". In: *Physics in Medicine & Biology* 50.22, p. 5263.

Kuntz, J, J Dinkel, S Zwick, T Bäuerle, M Grasruck, F Kiessling, R Gupta, W Semmler, and S. Bartling (2010). "Fully Automated Intrinsic Respiratory and Cardiac Gating for Small Animal CT". In: *Physics in Medicine & Biology* 55.7, p. 2069.

Lambert, J. H. (1760). *Photometria Sive de Mensura et Gradibus Luminis, Colorum et Umbrae*. Klett.

Lemmens, C., D. Faul, and J. Nuyts (2008). "Suppression of Metal Artifacts in CT using a Reconstruction Procedure that Combines MAP and Projection Completion". In: *IEEE transactions on medical imaging* 28.2, pp. 250–260.

Leng, S., J. Tang, J. Zambelli, B. Nett, R. Tolakanahalli, and G.-H. Chen (2008a). "High Temporal Resolution and Streak-Free Four-Dimensional Cone-Beam Computed Tomography". In: *Physics in medicine & biology* 53.20, p. 5653.

Leng, S., J. Zambelli, R. Tolakanahalli, B. Nett, P. Munro, J. Star-Lack, B. Paliwal, and G.-H. Chen (2008b). "Streaking artifacts reduction in four-dimensional cone-beam computed tomography". In: *Med. Phys.* 35.10, pp. 4649–4659.

Lentner, C. (1990). *Geigy Scientific Tables. Vol. 5: Heart and Circulation*. Ciba-Geigy.

Lewis, J. H., R. Li, X. Jia, W. T. Watkins, Y. Lou, W. Y. Song, and S. B. Jiang (2011). "Mitigation of Motion Artifacts in CBCT of Lung Tumors Based on Tracked Tumor Motion during CBCT Acquisition". In: *Physics in Medicine & Biology* 56.17, p. 5485.

Li, H., R. Mohan, and X. R. Zhu (2008). "Scatter Kernel Estimation with an Edge-Spread Function Method for Cone-Beam Computed Tomography Imaging". In: *Physics in Medicine & Biology* 53.23, p. 6729.

Li, T, E. Schreibmann, Y Yang, and L Xing (2005). "Motion Correction for Improved Target Localization with On-Board Cone-Beam Computed Tomography". In: *Physics in Medicine & Biology* 51.2, p. 253.

Li, T., L. Xing, P. Munro, C. McGuinness, M. Chao, Y. Yang, B. Loo, and A. Koong (2006). "Four-Dimensional Cone-Beam Computed Tomography using an On-Board Imager". In: *Med. Phys.* 33.10, pp. 3825–3833.

Lo, J. Y., C. E. Floyd, J. A. Baker, and C. E. Ravin (1993). "An Artificial Neural Network for Estimating Scatter Exposures in Portable Chest Radiography". In: *Med. Phys.* 20.4, pp. 965–973.

Love, L. A. and R. A. Kruger (1987). "Scatter Estimation for a Digital Radiographic System using Convolution Filtering". In: *Med. Phys.* 14.2, pp. 178–185.

Low, D. A., M. Nystrom, E. Kalinin, P. Parikh, J. F. Dempsey, J. D. Bradley, S. Mutic, S. H. Wahab, T. Islam, G. Christensen, et al. (2003). "A Method for the Reconstruction of Four-Dimensional Synchronized CT Scans Acquired During Free Bsreathing". In: *Med. Phys.* 30.6, pp. 1254–1263.

Lu, J., T. M. Guerrero, P. Munro, A. Jeung, P.-C. M. Chi, P. Balter, X. R. Zhu, R. Mohan, and T. Pan (2007). "Four-Dimensional Cone Beam CT with Adaptive Gantry Rotation and Adaptive Data Sampling". In: *Medical physics* 34.9, pp. 3520–3529.

Mahnken, A. H., R. Raupach, J. E. Wildberger, B. Jung, N. Heussen, T. G. Flohr, R. W. Günther, and S. Schaller (2003). "A new Algorithm for Metal Artifact Reduction in Computed Tomography: in Vitro and in Vivo Evaluation after Total Hip Replacement". In: *Investigative radiology* 38.12, pp. 769–775.

Maier, J., S. Sawall, M. Knaup, and M. Kachelrieß (2018). "Deep Scatter Estimation (dse): Accurate Real-Time Scatter Estimation for X-Ray CT using a Deep Convolutional Neural Network". In: *Journal of Nondestructive Evaluation* 37.3, p. 57.

McDavid, W. D., R. G. Waggener, W. H. Payne, and M. J. Dennis (1977). "Correction for Spectral Artifacts in Cross-Sectional Reconstruction from X Rays". In: *Med. Phys.* 4.1, pp. 54–57.

Meyer, E., R. Raupach, M. Lell, B. Schmidt, and M. Kachelrieß (Oct. 2010). "Normalized Metal Artifact Reduction (NMAR) in Computed Tomography". In: *Med. Phys.* 37.10, pp. 5482–5493.

Meyer, E., R. Raupach, M. Lell, B. Schmidt, and M. Kachelrieß (Apr. 2012). "Frequency Split Metal Artifact Reduction (FSMAR) in Computed Tomography". In: *Med. Phys.* 39.4, pp. 1904–1916.

Meyer, M., W. A. Kalender, and Y. Kyriakou (2009). "A fast and Pragmatic Approach for Scatter Correction in Flat-Detector CT using Elliptic Modeling and Iterative Optimization". In: *Physics in Medicine & Biology* 55.1, p. 99.

Moser, T, J Biederer, S Nill, G Remmert, and R Bendl (2008). "Detection of Respiratory Motion in Fluoroscopic Images for Adaptive Radiotherapy". In: *Physics in Medicine & Biology* 53.12, p. 3129.

O'Brien, F. W. (1928). "Elevation of the diaphragm". In: *Radiology* 10.3, pp. 226–233.

Oehler, M. and T. M. Buzug (2006). "Modified MLEM Algorithm for Artifact Suppression in CT". In: *2006 IEEE Nuclear Science Symposium Conference Record*. Vol. 6. IEEE, pp. 3511–3518.

Orfanidis, S. J. (1995). *Introduction to Signal Processing*. Prentice-Hall, Inc., pp. 532–534.

Palta, J. R., C. Liu, and J. G. Li (2008). "Quality assurance of intensity-modulated radiation therapys". In: *International Journal of Radiation Oncology* Biology* Physics* 71.1, S108–S112.

Pan, T., T.-Y. Lee, E. Rietzel, and G. T. Chen (2004). "4D-CT Imaging of a Volume Influenced by Respiratory Motion on Multi-Slice CT". In: *Med. Phys.* 31.2, pp. 333–340.

Pengpan, T, W Qiu, N. Smith, and M Soleimani (2012). "Cone Beam CT Using Motion-Compensated Algebraic Reconstruction Methods with Limited Data". In: *Computer methods and programs in biomedicine* 105.3, pp. 246–256.

Prell, D., Y. Kyriakou, M. Beister, and W. A. Kalender (2009). "A novel Forward Projection-Based Metal Artifact Reduction Method for Flat-Detector Computed Tomography". In: *Physics in Medicine & Biology* 54.21, p. 6575.

Purdie, T. G., D. J. Moseley, J.-P. Bissonnette, M. B. Sharpe, K. Franks, A. Bezjak, and D. A. Jaffray (2006). "Respiration Correlated Cone-Beam Computed Tomography and 4DCT for Evaluating Target Motion in Stereotactic Lung Radiation Therapy". In: *Acta Oncologica* 45.7, pp. 915–922.

Quirk, S., N. Becker, and W. Smith (2013). "External Respiratory Motion Analysis and Statistics for Patients and Volunteers". In: *Journal of applied clinical medical physics* 14.2, pp. 90–101.

Rührnschopf, E.-P. and K. Klingenbeck (2011). "A General Framework and Review of Scatter Correction Methods in X-Ray Cone-Beam Computerized Tomography. Part 1: Scatter Compensation Approaches". In: *Med. Phys.* 38.7, pp. 4296–4311.

Rinkel, J, L Gerfault, F Esteve, and J. Dinten (2007). "A new Method for X-Ray Scatter Correction: First Assessment on a Cone-Beam CT Experimental Setup". In: *Physics in Medicine & Biology* 52.15, p. 4633.

Rit, S., J. W. Wolthaus, M. van Herk, and J.-J. Sonke (2009). "On-the-Fly Motion-Compensated Cone-Beam CT Using an a Priori Model of the Respiratory Motion". In: *Med. Phys.* 36.6Part1, pp. 2283–2296.

Ritschl, L., F. Bergner, C. Fleischmann, and M. Kachelrieß (2010). "Water Calibration for CT Scanners with Tube Voltage Modulation". In: *Phys. Med. Biol.* 55.14, p. 4107.

Ritschl, L., F. Bergner, C. Fleischmann, and M. Kachelrieß (2011). "Improved Total Variation-Based CT Image Reconstruction Applied to Clinical Data". In: *Physics in Medicine & Biology* 56.6, p. 1545.

Ritschl, L., S. Sawall, M. Knaup, A. Hess, and M. Kachelrieß (2012). "Iterative 4D Cardiac Micro-CT Image Reconstruction Using an Adaptive Spatio-Temporal Sparsity Prior". In: *Physics in Medicine & Biology* 57.6, p. 1517.

Rührnschopf, E.-P. and K. Klingenbeck (2011). "A General Framework and Review of Scatter Correction Methods in Cone Beam CT. Part 2: Scatter Estimation Approaches". In: *Med. Phys.* 38.9, pp. 5186–5199.

Ruth, C. and P. M. Joseph (1995). "A Comparison of Beam-Hardening Artifacts in X-Ray Computerized Tomography with Gadolinium and Iodine Contrast Agents". In: *Med. Phys.* 22.12, pp. 1977–1982.

Sauppe Sebastian Rank, C. M., A. Hahn, M. Brehm, P. Paysan, D. Seghers, and M. Kachelrieß (May 2016a). "Cardio-Respiratory Motion Compensation for 5D Thoracic CBCT in IGRT". In: *Proceedings ESTRO 35*.

Sauppe, S., A. Hahn, M. Brehm, P. Paysan, and M. Kachelrieß (2016b). "Five-Dimensional Motion Compensation for Respiratory and Cardiac Motion with Cone-Beam CT of the Thorax Region". In: *Proceedings 2016 SPIE Medical Imaging Conference*.

Sauppe, S., J. Kuhm, M. Brehm, P. Paysan, D. Seghers, and M. Kachelrieß (2018). "Motion Vector Field Phase-to-Amplitude Resampling for 4D Motion-Compensated Cone-Beam CT". In: *Physics in Medicine & Biology* 63.3, p. 035032.

Sawall, S., F. Bergner, R. Lapp, M. Mronz, M. Karolczak, A. Hess, and M. Kachelrieß (2011). "Low-Dose Cardio-Respiratory Phase-Correlated Cone-Beam Micro-CT of Small Animals". In: *Med. Phys.* 38.3, pp. 1416–1424.

Schäfer, D., M. Bertram, N. Conrads, J. Wiegert, G. Rose, and V. Rasche (2004). "Motion Compensation for Cone-Beam CT Based on 4D Motion Field of Sinogram Tracked Markers". In: *International Congress Series*. Vol. 1268. Elsevier, pp. 189–194.

Sidky, E. Y. and X. Pan (2008). "Image Reconstruction in Circular Cone-Beam Computed Tomography by Constrained, Total-Variation Minimization". In: *Physics in Medicine & Biology* 53.17, p. 4777.

Sonke, J.-J., L. Zijp, P. Remeijer, and M. van Herk (2005). "Respiratory Correlated Cone Beam CT". In: *Med. Phys.* 32.4, pp. 1176–1186.

Sonke, J.-J., M. Rossi, J. Wolthaus, M. van Herk, E. Damen, and J. Belderbos (2009). "Frameless Stereotactic Body Radiotherapy for Lung Cancer using Four-Dimensional Cone Beam CT Guidance". In: *International Journal of Radiation Oncology* Biology* Physics* 74.2, pp. 567–574.

Spies, L, M Ebert, B. Groh, B. Hesse, and T Bortfeld (2001). "Correction of Scatter in Megavoltage Cone-Beam CT". In: *Physics in Medicine & Biology* 46.3, p. 821.

Star-Lack, J., M. Sun, A. Kaestner, R. Hassanein, G. Virshup, T. Berkus, and M. Oelhafen (2009). "Efficient Scatter Correction using Asymmetric Kernels". In: *Medical Imaging 2009: Physics of Medical Imaging*. Vol. 7258. International Society for Optics and Photonics, 72581Z.

Sterzing, F., J. Kalz, G. Sroka-Perez, K. Schubert, M. Bischof, F. Röder, J. Debus, and K. Herfarth (2009). "Megavoltage CT in Helical Tomotherapy—Clinical Advantages and Limitations of Special Physical Characteristics". In: *Technology in cancer research & treatment* 8.5, pp. 343–352.

Sterzing, F., R. Engenhart-Cabillic, M. Flentje, and J. Debus (2011). "Image-Guided Radiotherapy: A New Dimension in Radiation Oncology". In: *Deutsches Aerzteblatt International* 108.16, p. 274.

Stonestrom, J. P., R. E. Alvarez, and A. Macovski (1981). "A Framework for Spectral Artifact Corrections in X-ray CT". In: *IEEE Transactions on Biomedical Engineering* 2, pp. 128–141.

Sun, M and J. Star-Lack (2010). "Improved Scatter Correction using Adaptive Scatter Kernel Superposition". In: *Physics in Medicine & Biology* 55.22, p. 6695.

Swindell, W. and P. M. Evans (1996). "Scattered Radiation in Portal Images: a Monte Carlo Simulation and a Simple Physical Model". In: *Med. Phys.* 23.1, pp. 63–73.

Tacke, M. B., S. Nill, A. Krauss, and U. Oelfke (2010). "Real-Time Tumor Tracking: Automatic Compensation of Target Motion using the Siemens 160 MLC". In: *Med. Phys.* 37.2, pp. 753–761.

Tan, W., L. Xu, X. Wang, D. Qiu, G. Han, and D. Hu (2013). "Estimation of the Displacement of Cardiac Substructures and the Motion of the Coronary Arteries using Electrocardiographic Gating". In: *OncoTargets and therapy* 6, p. 1325.

Thirion, J.-P. (1998). "Image Matching as a Diffusion Process: an Analogy with Maxwell's Demons". In: *Medical image analysis* 2.3, pp. 243–260.

Toftegaard, J., W. Fledelius, D. Seghers, M. Huber, M. Brehm, E. S. Worm, U. V. Elstrøm, and P. R. Poulsen (2014). "Moving Metal Artifact Reduction in Cone-Beam CT Scans with Implanted Cylindrical Gold Markers". In: *Med. Phys.* 41.12.

Tsunashima, Y., T. Sakae, Y. Shioyama, K. Kagei, T. Terunuma, A. Nohtomi, and Y. Akine (2004). "Correlation Between the Respiratory Waveform Measured using a Respiratory Sensor and 3D Tumor Motion in Gated Radiotherapy". In: *International Journal of Radiation Oncology* Biology* Physics* 60.3, pp. 951–958.

Tucker, D. M., G. T. Barnes, and D. P. Chakraborty (1991). "Semiempirical model for generating tungsten target x-ray spectra". In: *Med. Phys.* 18.2, pp. 211–218.

Van Herk, M, L Zijp, P Remeijer, J Wolthaus, and J. Sonke (2007). "On-Line 4D Cone Beam CT for Daily Correction of Lung Tumour Position during Hypofractionated Radiotherapy". In: *ICCR, Toronto, Canada*.

Vedam, S., P. Keall, V. Kini, H Mostafavi, H. Shukla, and R Mohan (2002). "Acquiring a Four-Dimensional Computed Tomography Dataset Using an External Respiratory Signal". In: *Physics in Medicine & Biology* 48.1, p. 45.

Veldkamp, W. J., R. M. Joemai, A. J. van der Molen, and J. Geleijns (2010). "Development and Validation of Segmentation and Interpolation Techniques in Sinograms for Metal Artifact Suppression in CT". In: *Med. Phys.* 37.2, pp. 620–628.

Verellen, D., M. De Ridder, and G. Storme (2008). "A (short) History of Image-Guided Radiotherapy". In: *Radiotherapy and Oncology* 86.1, pp. 4–13.

Vergalasova, I., J. Cai, and F.-F. Yin (2012). "A Novel Technique for Markerless, Self-Sorted 4D-CBCT: Feasibility Study". In: *Med. Phys.* 39.3, pp. 1442–1451.

Wang, G., D. L. Snyder, J. A. O'Sullivan, and M. W. Vannier (1996). "Iterative Deblurring for CT Metal Artifact Reduction". In: *IEEE transactions on medical imaging* 15.5, pp. 657–664.

Wang, J. and X. Gu (2013). "Simultaneous Motion Estimation and Image Reconstruction (SMEIR) for 4D Cone-Beam CT". In: *Med. Phys.* 40.10.

Wei, J., L. Chen, G. A. Sandison, Y. Liang, and L. X. Xu (2004). "X-ray CT High-Density Artefact Suppression in the Presence of Bones". In: *Physics in Medicine & Biology* 49.24, p. 5407.

Yan, H., X. Zhen, M. Folkerts, Y. Li, T. Pan, L. Cervino, S. B. Jiang, and X. Jia (2014). "A Hybrid Reconstruction Algorithm for Fast and Accurate 4D Cone-Beam CT Imaging". In: *Med. Phys.* 41.7.

Yan, H., F.-F. Yin, G.-P. Zhu, M. Ajlouni, and J. H. Kim (2006). "The Correlation Evaluation of a Tumor Tracking System using Multiple External Markers". In: *Med. Phys.* 33.11, pp. 4073–4084.

Yu, L., H. Li, J. Mueller, J. M. Kofler, X. Liu, A. N. Primak, J. G. Fletcher, L. S. Guimaraes, T. Macedo, and C. H. McCollough (2009). "Metal Artifact Reduction from Reformatted Projections for Hip Prostheses in Multislice Helical Computed Tomography: Techniques and Initial Clinical Results". In: *Investigative radiology* 44.11, p. 691.

Zeidan, O. A., K. M. Langen, S. L. Meeks, R. R. Manon, T. H. Wagner, T. R. Willoughby, D. W. Jenkins, and P. A. Kupelian (2007). "Evaluation of image-guidance protocols in the treatment of head and neck cancers". In: *International Journal of Radiation Oncology* Biology* Physics* 67.3, pp. 670–677.

Zhang, H., J. Ma, Z. Bian, D. Zeng, Q. Feng, and W. Chen (2017). "High Quality 4D Cone-Beam CT Reconstruction using Motion-Compensated Total Variation Regularization". In: *Physics in Medicine & Biology* 62.8, p. 3313.

Zhang, Q., Y.-C. Hu, F. Liu, K. Goodman, K. E. Rosenzweig, and G. S. Mageras (2010). "Correction of Motion Artifacts in Cone-Beam CT using a Patient-Specific Respiratory Motion Model". In: *Med. Phys.* 37.6Part1, pp. 2901–2909.

Zhang, T., H. Keller, M. J. O'Brien, T. R. Mackie, and B. Paliwal (2003). "Application of the spirometer in respiratory gated radiotherapy". In: *Med. Phys.* 30.12, pp. 3165–3171.

Zijp, L., J.-J. Sonke, and M. van Herk (2004). "Extraction of the Respiratory Signal from Sequential Thorax Cone–Beam X–Ray Images". In: *Proc. of the 14th ICCR, Seoul, Korea*, pp. 507–509.

List of Figures

List of Tables

Publications

Parts of this thesis have been published in the following journal articles and conference contributions:

Journal Articles (Peer Reviewed)

Hahn, **A.**, M. Knaup, M. Brehm, S. Sauppe, and M. Kachelrieß (2018b). "Two Methods for Reducing Moving Metal Artifacts in Cone-Beam CT". In: *Med. Phys.* 45.8, pp. 3671–3680.

Conference Proceedings

Hahn, **A.** and M. Kachelrieß (May 2018). "Fully Automatic Intrinsic Respiratory and Cardiac Gating of Cone-Beam CT Scans of the Thorax Region". In: *The Fifth International Conference on Image Formation in X-Ray Computed Tomography, Proceedings*.

Hahn, **A.**, M. Knaup, and M. Kachelrieß (Nov. 2018). "A Robust Fully Automatic Method for Intrinsic Respiratory and Cardiac Gating for Cone-Beam CT Scans of the Thorax Region". In: *104th Scientific Assembly and Annual Meeting of the Radiological Society of North America (RSNA), Proceedings*.

Hahn, **A.**, S. Sauppe, M. Knaup, and M. Kachelrieß (Feb. 2018a). "Moving Metal Artifact Reduction for Cone-Beam CT (CBCT) Scans of the Thorax Region". In: *Insights into Imaging, ECR Book of Abstracts*.

Sauppe Sebastian Rank, C. M., **A. Hahn**, M. Brehm, P. Paysan, D. Seghers, and M. Kachelrieß (May 2016a). "Cardio-Respiratory Motion Compensation for 5D Thoracic CBCT in IGRT". In: *Proceedings ESTRO 35*.

Sauppe, S., **A. Hahn**, M. Brehm, P. Paysan, and M. Kachelrieß (2016b). "Five-Dimensional Motion Compensation for Respiratory and Cardiac Motion with Cone-Beam CT of the Thorax Region". In: *Proceedings 2016 SPIE Medical Imaging Conference*.

Acknowledgments

First of all, I want to thank Prof. Dr. Marc Kachelrießfor giving me the opportunity to join his group 'X-Ray Imaging and CT' at the German Cancer Research Center (DKFZ) in Heidelberg. His advice and continuous support made this thesis possible. I also want to thank the other members of my thesis advisory committee, Prof. Dr. Peter Bachert and Prof. Dr. Christoph Bert, for the very interesting and fruitful discussions.

Thanks also go to my colleague Sebastian for the close cooperation and interesting exchange of ideas and Nadine, Sabrina, Stefan and the rest of group E025 for always being helpful and providing useful advice when needed.

Special thanks go to my friends Lena, Rabi, Sebastian, Jutta, Christopher, Mimi and Marieke, for always showing interest to my work and their continuous encouragement and motivation.

Finally, I want to thank my sisters Juliane and Ines as well as my parents Angelika and Wolfgang for their support, interest and being an important part in this journey.